


专业技术职务申报简表（理工类-2016 版）

所在单位： 生物与医学工程学院

填表时间：2016 年 5 月 15 日

姓 名	乔惠婷	性别	女	出生年月	1980.12	
最后学历	博士	学位	博士	拟申请专业技术职务	副教授	
现任专业技术职务	讲师	现任专业技术职务批准时间		2008.12		
申报学科（一级/二级学科名称）	生物医学工程			研究方向	生物医学信息与仪器	
申报类别	<input checked="" type="checkbox"/> 教师 <input type="checkbox"/> 科学研究 <input type="checkbox"/> 工程 <input type="checkbox"/> 实验 <input type="checkbox"/> 其他					

主要学习工作经历及海外经历（从高中起，应连续）

起止年月		学习与工作单位	学历、学位、专业、职务
起	止		
1995.9	1998.7	哈尔滨第三中学	高中，学生
1998.9	2003.7	天津大学 精密仪器与光电子工程学院	本科，学士，生物医学工程，学生
2003.9	2008.7	清华大学 医学院	研究生，博士，生物医学工程，学生
2008.9	今	北航 生物与医学工程学院	生物医学工程，讲师
2014.7	2015.7	美国德雷赛尔大学	访问学者，生物医学工程系（375 天）

研究水平和特点概述（限填 200 字）

开展了代谢模型构建、血管形态描述、肿瘤识别的算法研究和呼吸力学研究，发现了肿瘤与正常组织代谢的动态差异，提出了短时动态 PET 检测肿瘤的创新性方法，搭建了肺通气研究平台，应用于医疗器械研发，申请 5 项专利，已有 2 项授权。主持国家及省部级 9 项课题的支持，近五年经费 144.6 万，发表论文 20 篇，其中以第一或通讯作者发表 11 篇，6 篇 SCI，5 篇 EI，一篇文章被知名医学网站 MDLinx 评为 featured article。由于个人努力及所取得的成绩，入选北京市“青年英才”计划，被评为北航“蓝天新星”。

请填写任现职以来取得的代表性学术成果情况（限填 5 项，其中论文不少于 3 篇，奖励、专著或教材等各不多于 1 项）

学术论文题目	发表刊物或会议	发表（出版）时间	收录、他引情况	影响因子	期刊分区及排名/总数	作者排名
The three-dimensional shape analysis of the M1 segment of the middle cerebral artery using MRA at 3T	NEURORADIOLOGY	2014	SCI/0	2.485	Q2 41/125	通讯作者
A study of the metabolism of transplanted tumor in the lung by micro PET/CT in mice.	Medical Engineering & Physics	2014	SCI/0	1.825	Q2 35/76	第 1 作者
The Transport and deposition of Nanoparticles in respiratory system by inhalation	Journal of Nanomaterials	2015	SCI/1	1.644	Q2 122/260	第 1 作者
The effect of tumor size on the imaging diagnosis: A study based on simulation	Bio-medical materials and engineering	2014	SCI/0	1.091	Q3 57/76	第 1 作者
Modeling the excretion of FDG in human kidneys using dynamic PET	Computers in Biology and Medicine	2008	SCI/1	1.24	Q3 52/76	第 1 作者

任现职以来发表论文及收录情况：收录类别、作者贡献（第一、通讯等）仅计算 1 次；论文收录以图书馆检索证明为准，未检索到的来源刊论文仅计算 1 篇

类别	合计	SCI	SSCI	CSSCI	EI	ISTP	中文核心期刊	其他
一、符合职称申报条件论文	11	6			5			
其中：1.第一作者	8	5			3			
2.学生第一本人第二作者								
3.通讯作者	3	1			2			

二、其他	9	5		1	2	1
------	---	---	--	---	---	---

任现职以来获得国家级教学/科研成果奖_____项；省部级教学/科研成果一等奖前五名、二等奖前三名或三等奖第一名1项。请填写任现职以来获得教学、科研、管理奖励情况（限填3项，代表作成果除外）

获奖项目	奖励名称	颁奖部门	奖励级别	获奖时间	人数	排名
北京市支持中央高校项目	青年英才计划	北京市	省部级	2013	1	1
校蓝天新星项目（教学型）	“蓝天新星”称号	北航	校级	2011	1	1
以交叉创新为导向的研究生多元化学术活动模式及其实践	优秀教学成果二等奖	北航	校级	2013	5	3

任现职以来共获得排名第一（含学生第一本人第二）授权专利2项，其中发明专利2项，实用新型_____项，外观设计_____项。请填写任现职以来共获得已授权专利情况（限填3项）

专利名称	专利类型	授权日期	批准机构	专利号	权利单位	人数	排名
一种无创通气接口检测系统	发明专利	2016-01-06	国家知识产权局	ZL 2012 1 0438841.1	北航	5	1
一种基于压力波形估算容量控制通气漏气量的方法	发明专利	2016-04-27	国家知识产权局	ZL 2014 1 0232734.2	北航	5	1

任现职以来共主持纵向项目9项（不含参与，以任务书为准）：其中国家级1项，经费到款23万；省部级8项，经费到款67.5万；千万元以上_____项，经费到款_____万；请填写任现职以来主持的纵向项目（限填5项）

项目名称	项目来源	起止时间	到款/经费总额
基于 micro PET/CT 对肺部肿瘤与炎症葡萄糖代谢动态特征的研究	国家自然科学基金	2012.1-2014.12	23/23 万
青年英才计划	北京市支持中央高校项目	2013.1-2015.12	15/15 万
基于医学影像的脑血管构型及疾病防护	中央高校基本科研业务费专项	2015.1-2015.12	12/12 万
航空复杂环境下心血管-呼吸系统响应与防护研究	中央高校基本科研业务费专项	2014.1-2014.12	15/15 万
利用聚类分析从 PET/CT 短时动态成像中识别肿瘤组织的方法研究	中央高校基本科研业务费专项	2010.1-2010.12	5/5 万

任现职以来其他项目情况（限填3项）

项目名称	项目来源	起止时间	负责人	承担份额/总额	主持/参与
强机动目标追踪控制算法与软件开发	上海航天控制技术研究所	2015.12-2016.6	乔惠婷	19.1/19.1	主持
基于流体伺服作动式外骨骼机器人的运动及生物力学模型研究	哈尔滨工程大学	2016.5-2017.12	乔惠婷	50/50 万	主持

任现职以来的教育教学情况：主讲课程共计641学时；指导本科生毕设8人次；指导硕士研究生6人次；指导博士研究生_____人次。请填写任现职以来主讲的3门课程

课程名称	起止时间	课程学时	本人授课学时	授课次数	授课对象	课程性质
生物医学信号处理	2008.9-至今	48	25	6	本科生	必修课
生理系统建模与仿真	2009.9-2014.6	32	11	6	本科生	必修课
生理信号检测与处理实验	2013.3-2014.7	18	14	2	研究生	学位课

主要学术兼职（限填3项）

学术兼职名称	受聘日期	颁授机构
中国生物医学工程学会教育及科普工作委员会委员	2013.12	中国生物医学工程学会

任现职以来其他业绩成果（限100字）

获青年教师教学基本功比赛一等奖，指导硕士获北航工程硕士实习实践优秀成果奖、国家奖学金。2008-2009 兼任学生工作负责人，2008 年-2014 年兼任学院党务秘书，被评为优秀党务工作者，60 周年校庆积极奉献奖，年度考核多次被评为优秀。

本人确认表内所填内容属实，如与事实不符，本人愿承担一切责任。 本人签字：_____ 日期：2016.5.30

申请人所填内容真实性核实无误。

单位审核人签字：_____ 日期：_____ 单位负责人签字：_____（加盖单位公章） 日期：_____

The three-dimensional shape analysis of the M1 segment of the middle cerebral artery using MRA at 3T

Jintao Han · Huiting Qiao · Xuan Li · Xiaogang Li ·
Qingyuan He · Yu Wang · Ziman Cheng

Received: 24 March 2014 / Accepted: 22 July 2014 / Published online: 15 August 2014
© Springer-Verlag Berlin Heidelberg 2014

Abstract

Introduction The M1 segment of the middle cerebral artery (MCA) is of great importance to neurosurgery and interventional radiology. The purpose of this study was to describe the M1 segment in three dimensions based on shape projection using magnetic resonance angiography (MRA).

Methods A three-view method was established and used in the retrospective analysis of 717 M1 segments derived from 3D-TOF MRA images. In this method, the M1 segment was first projected on three orthogonal planes (axial, coronal, and sagittal plane); the courses of the projected vessels were classified as line-shape, C-shape, or S-shape on each orthogonal plane; and then the actual parameters, including internal diameter and so on, were measured on the projected images. The shape classifications and the measured parameters were efficient methods of describing the M1 segment. Twelve geometric models of the vessels were reconstructed and were compared with those from an actual validation method.

Results The 3D shape of the M1 segment in the 3D orthogonal views was not uniform. Only 17.3 % M1 segments were straight, 43.5 % followed plane curves, and nearly 40 % were

tortuous in 3D space. The probability distributions of shape classifications changed with age. The proportion of the tortuous vessels increased with age. We also showed that the three-view method is effective with a volume relative error of less than 13 %.

Conclusion The three-view method is convenient for describing the 3D morphology, including the shape information, of the M1 segment. It is a potential method for planning and predicting risk in neurosurgery/neurointervention.

Keywords The M1 segment of the middle cerebral artery · Magnetic resonance angiography · Shape classification · Three-view/orthogonal views · Geometric model

Introduction

The M1 segment of the middle cerebral artery (MCA) plays an important role in cerebral blood supply. It commonly suffers from pathological conditions such as stroke, and nearly one quarter of intracranial atherosclerosis cases are found at the M1 segment [1, 2]. Because the M1 segment is of great importance to neurosurgery and interventional radiology [3–5] and information about its shape is also important for the assessment of the success of endovascular therapy in stroke patients, this study focused on the shape analysis of the M1 segment of the MCA.

The M1 segment is the first segment of the MCA and courses posterior and parallel to the sphenoid bone [6]. Numerous anterolateral, central, lateral, and lenticulostriate arteries, irrigating basal ganglia and insula, are fed by the M1 segment [7]. The surgical anatomy of the M1 segment of the MCA has been studied by Rhoton, Yasargil [8], Lasjaunias [9], and others [6, 10]. The morphology of the M1 segment is usually described with anatomical terminology. In neuroradiology, the M1 segment is defined as the proximal segment of

J. Han · X. Li
Department of Interventional Radiology and Vascular Surgery,
Peking University Third Hospital, Beijing, China

H. Qiao (✉) · Y. Wang · Z. Cheng
School of Biological Science and Medical Engineering, Beihang
University, 100191 Beijing, China
e-mail: qht@buaa.edu.cn

X. Li
Department of Neurology, Peking University Third Hospital,
Beijing, China

Q. He
Department of Radiology, Peking University Third Hospital, Beijing,
China

the middle cerebral artery arising from the internal carotid artery to the first main division of the MCA [11], which follows a nearly parallel course [12]. With the development of medical imaging, vascular morphology could be studied in detail in a large number of cases [13, 14]. Recently, individual differences in the M1 segment's morphology have been a target for investigation. The division patterns and early cortical branches have been studied, and the main anatomical features have been reported [15]. However, these anatomical descriptions of the vessel are not enough for the planning and the prediction of risk in neurosurgery; quantitative analysis in three dimensions is preferred.

Some mathematical descriptions have been incorporated in the morphometry of vessels [16–19]; length, internal diameter, direction cosines, deviation index (DI), and tortuous index (TI) [20] have been used for the description of cerebral vessels. Though DI and TI can objectively describe the sinuosity and tortuosity of vessels, the shape information has thus far been neglected. There is well-documented evidence that the morphology of blood vessels, especially the shape, has a major impact on hemodynamics and consequently in the development of vascular diseases [21, 22]. For example, vascular plaques often arise in regions with low and oscillatory shear forces [23]. The course of the M1 segment does not always follow a straight line, as it may also take an undulating C- or S-shaped route [24]. Numerical simulations of blood flow have revealed that the camber of a C-shape will affect the flow patterns and wall shear stress (WSS) and that the S-shape will create swirling flow to eliminate low WSS zones [25]. Perhaps, the shape of the M1 segment has some relationship to blood vessel pathology. The 3D shape of the M1 segment is also an important factor that may affect endovascular procedures and may have direct relevance in selecting a suitable treatment strategy [26]. It has been reported that the shape of some cerebral vessels may change with age [27].

The purpose of this study is to provide a new method to describe the shape of the MCA M1 segment qualitatively and quantitatively in three dimensions, which may assist in diagnosis and risk prediction.

Materials and methods

Subjects

We retrospectively analyzed the clinical and imaging data of 419 subjects, 254 males, and 165 females aged 8 to 93 years old (mean 59.5 years old), whose basal cranial arteries were examined by magnetic resonance angiography (MRA) in Peking University Third Hospital between January 2012 and December 2012. No participants in this study had a reported history of cerebrovascular disease or clearly vascular pathology such as aneurysms or hemorrhage. All data were collected

from the patient records and critically reviewed. Rare anatomical variants as duplicate origin [34], fenestrations [35], and early bifurcation [36] of the M1 segment were not included in this study. The study was approved by the Medical Ethics Committee of Peking University Third Hospital. Excluding clearly visible vascular pathologies and anatomical variations, 717 M1 segments were used for the retrospective analysis.

MRA technique

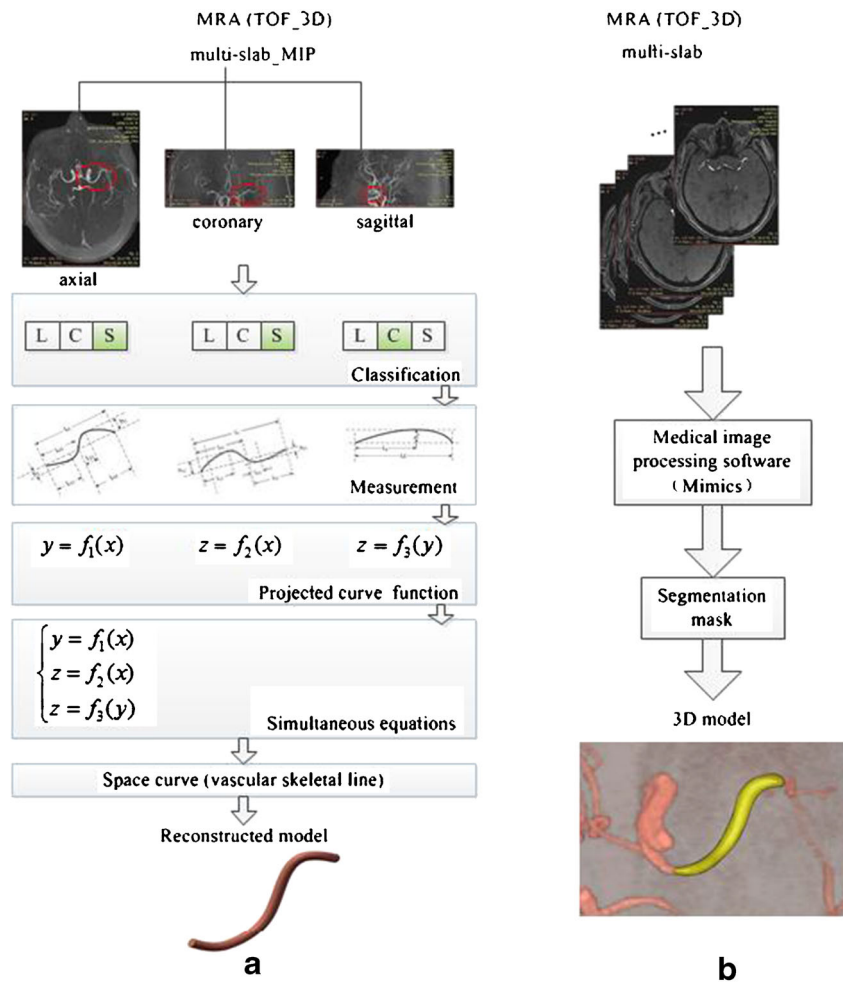
MRA was performed using a 3.0-T clinical MR system (MAGNETOM TRIO TIM; Siemens, Erlangen, Germany). The standard 3D-TOF MRA protocol was used with maximum intensity projection (MIP) reconstruction. A HD eight-channel high-resolution array coil was used. Parameters for the imaging sequence were as follows: TR=22 ms, TE=3.9 ms, flip angle $\alpha=15^\circ$, effective section thickness of 1.2 mm, and field of view of 220×165 mm. All MRA images obtained were imported into a PACS system (GE).

The three-view method

All 3D spatial structures can be described by projections onto three orthogonal views, and their spatial structure can also be reconstructed by orthogonal projection-views [31]. The three-view method was established based on the above principle. The M1 segment was described by shape classifications and measured parameters in three orthogonal views: axial, coronary, and sagittal planes.

There are four steps to describe a M1 segment by the three-view method (Fig. 1a). First, a coordinate system was defined in 3D space with the *x*-axis pointing to the participant's left side, the *y*-axis pointing towards the abdomen, and the *z*-axis pointing towards the feet. The origin of the coordinate system was assigned as the origin of the M1 segment connecting with the anterior cerebral artery. For some cases without an anterior cerebral artery, the origin of the coordinate system was mirrored from the contralateral vessel origin of the M1 segment. Second, the MIP images of the M1 segment were placed according to the defined 3D coordinate system. The MIP images required the head to be positioned on top in the coronary view and the abdomen on top in the axial view. Third, with the vessel projections on the MIP images, the curve shapes of the M1 segment on the three orthogonal views were described as three shape types: the line-, C-, and S-shapes. Last, some parameters were measured on each MIP image according to the shape type of the vessel projection, and then the quantitative function of the vessel projection could be determined (introduced in the following section in detail). To describe the shape of the M1 segment in 3D space, the shape-type descriptions from the three views must be combined. The shape types of each view were permuted through the axial, coronary, and sagittal views in turn, and thus, 27 shape

Fig. 1 The schemes of the three-view method and its validation. **a** The scheme of the description and reconstruction of the M1 segment. **b** The scheme shows how the 3D model was obtained, which was used to validate the reconstruction from the three-view method



classifications were formed. For example, the shape classification LSC means the shape type of the vessel in the axial view is the line-shape type, with the S-shape type in the coronary view and the C-shape type in the sagittal view. In this three-view method, the M1 segment was described by its shape classifications and quantitative projection functions. If we only consider the shape combinations of the M1 segment and neglect the permuting order of each projection view, the morphology of the M1 segment could be divided into ten spatial shape groups. This means that the LLC morphology (that is, L in the axial view, L in the coronary view, and C in the sagittal view) is similar to the LCL morphology (that is, L in the axial view, C in the coronary view, and L in the sagittal view), as the vessel looks like a line in two orthogonal views and a C-curve in the last orthogonal view for these two shape classifications. Some shape classifications with similar morphology were combined into one group, forming ten groups in total.

The quantitative description of the M1 segment was based on standard curve functions and the measurement of the feature points on the vessel projections. The functions for

the projected vessel varied according to the projection plane and the shape classifications. For instance, the “line-shape” vessel projection in the axial plane could be represented by a line equation, as $y = \tan \gamma \cdot x$. The “C-shape” vessel projection and the “S-shape” vessel projection were represented by cubic curves and quartic curves, respectively. Generally speaking, a cubic interpolation and modified cubic interpolation could describe most C-shape-projected vessels effectively. For some S-shape projected vessels, Runge’s phenomenon of polynomial interpolation was obvious. The problem could be solved using spline interpolation instead of polynomial interpolation. More characteristic points, for example, the midpoint of the arch, could be used as additional feature points to improve the quality of interpolation. Detailed function descriptions can be found in the “Appendix.”

The quantitative description of vessel projection

The parameters in the projection functions were determined by the measurements of the feature points in the projection plane. The parameters to be measured vary according to the

shape type (Fig. 2). For line-shape vessel projections, the length L and the rotation angle γ must be measured. For C-shape vessel projections, the length L_C , h_1 , L_1 , and the rotation angle γ must be measured. The maximum distance between the skeletal line of the projected vessel and the baseline was defined as h_1 . The point marking this maximum distance is a feature point. The projected distance of this point from the origin on the baseline was defined as L_1 . An S-shape vessel projection can be regarded as the combination of two C-shape parts, so two lengths, two projected distances, two heights, and the rotation angle γ must be measured. The rotation angle is the angle from the horizontal axis to the baseline that connects the origin and terminal of the projected M1 segment. The rotation angles from each view were used to describe the directions on the projection plane and do not affect the shape classification. Moreover, the internal diameter was measured at the proximal, middle, and distal parts of the M1 segment separately in the axial and coronary planes. All the MIP images were analyzed by two clinicians of interventional radiology and vascular surgery to confirm their shapes and characteristic parameters.

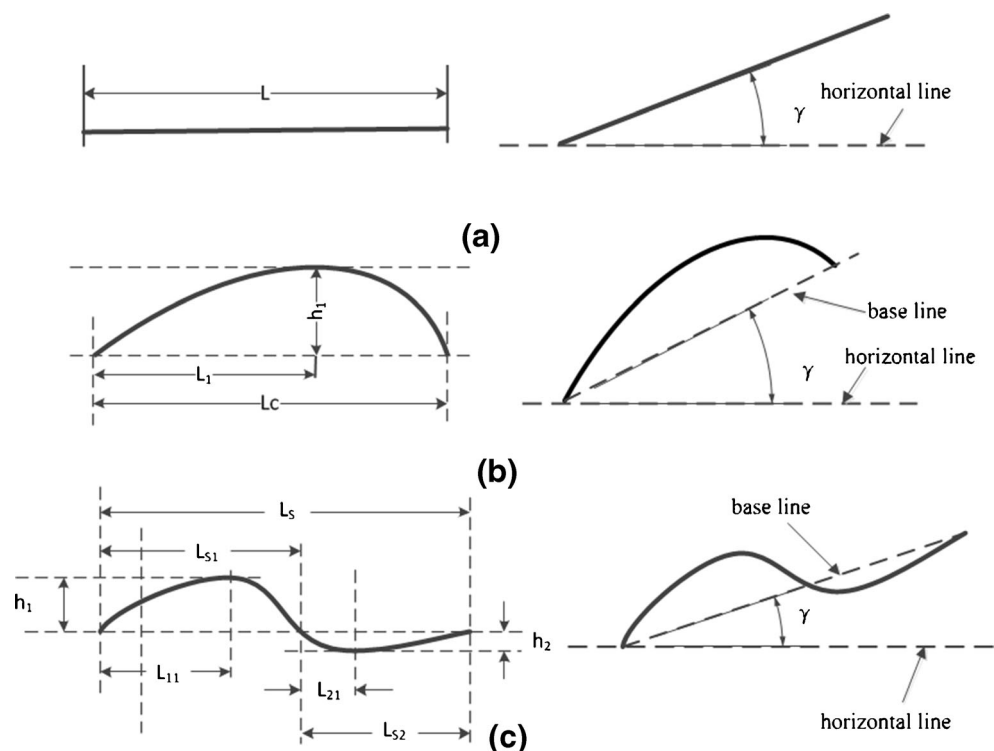
Model reconstruction and validation

The three-view method could be used to reconstruct the geometric 3D model of the vessel. The spatial skeletal line of the M1 segment could be reconstructed by solving the simultaneous equations of all the quantitative projection functions

(Fig. 1a). For example, the projection function on the axial plane is $y=f_1(x)$; the projection function on the coronary plane is $z=f_2(x)$; and the projection function on the sagittal plane is $z=f_3(y)$. The 3D skeletal line of M1 could be described as a spatial function $f_{3D}(x,y,z)=0$, which could be determined by solving the simultaneous equations $y=f_1(x)$, $z=f_2(x)$ and $z=f_3(y)$. In most cases, the function of the 3D skeletal line could be determined only with the simultaneous equations $y=f_1(x)$ and $z=f_2(x)$ because some spatial structures, which do not overlap on the projection view, can be represented and reconstructed by two orthogonal views [31]. With the 3D skeletal line and the information about the internal diameter, the 3D solid geometric model of the M1 segment could be obtained by solid-lofting reconstruction on any solid model platform.

To validate the quantitative shape description of the three-view method, 12 M1 segment vessels were sampled from the typical shape classifications at random and were used to reconstruct the 3D geometric model. The 3D models reconstructed using the three-view method were compared with the 3D model from Mimics (Materialise, Belgium), which is the software that is used to segment 3D medical images and to produce highly accurate 3D models of the patient's anatomy (Fig. 1b). The agreement of 3D models was first assessed by two clinicians and then using Solidworks software (Dassault Systemes, France). The 3D models produced by the different methods were overlapped in 3D space, and the volume difference was calculated. The agreement was then quantified by relative volume error.

Fig. 2 Schematic diagram of how M1 segment vessel parameters were measured. **a** The characteristic parameters of a “line-shape” vessel projection. **b** The characteristic parameters of a “C-shape” vessel projection. **c** The characteristic parameters of an “S-shape” vessel projection



Results

The MRA image data of 419 participants, totaling 838 M1 segments, were retrospectively reviewed. Excluding early bifurcation (26 cases), duplicate origin (5 cases), occlusion (13 cases), and stenosis (77 cases), 717 M1 segments were used in this study. In 2,151 MIP images of 717 M1 segments, the vessel projection of M1 segments could all be described as three shape types: line-shape, C-shape, and S-shape (Fig. 3). No M1 segment was found with an acute angle, such as a “V-shape,” with extreme tortuosity, or in other complex shapes, such as an “M-shape.” Moreover, the percentages of each shape type were not uniform. In all M1 segment projections from the 2,151 MIP images, there were 821 projections that could be described as a line-shape type, 928 projections as a C-shape type, and 402 projections as an S-shape type. The rates of the three shape types and the individual probabilities for each shape in the three orthogonal views are indicated in Table 1. The most probable shape of the M1 segment’s projection was the C-shape, which had a slightly higher proportion than that of the line-shape. The S-shape appeared less than the C-shape and the line-shape (Table 1). There were no significant differences in the probability of appearing on each

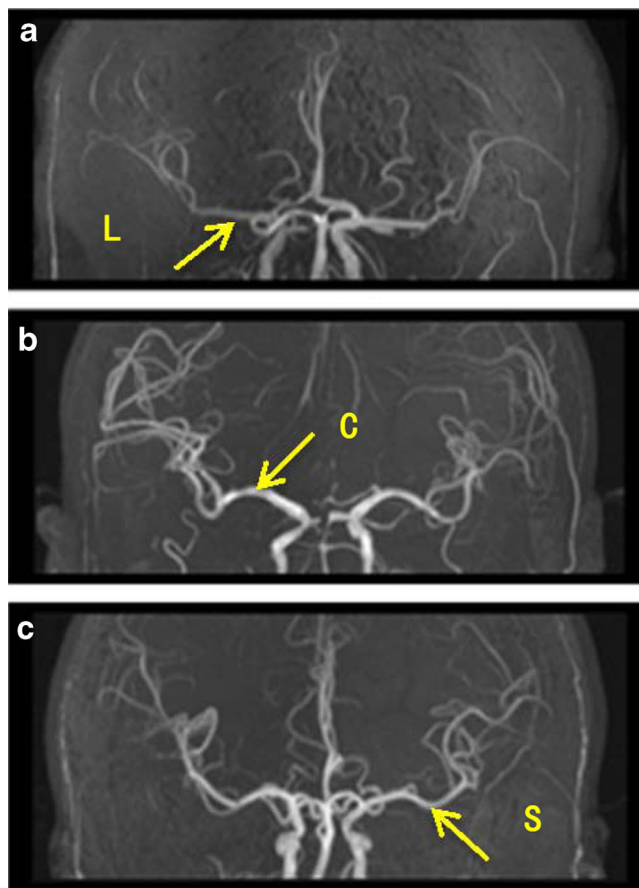


Fig. 3 MIP images of MRA coronary slabs with M1 segment in (a) line-shape, (b) C-shape, and (c) S-shape

Table 1 The statistics of the shape type of the M1 segment in each projection view

Shape types	Count (all)	Rate (%)	Probability on each projection view		
			Axial	Coronary	Sagittal
Line-shape	821	38.17	0.4351	0.3347	0.3752
C-shape	928	43.14	0.4561	0.3919	0.4463
S-shape	402	18.69	0.1088	0.2734	0.1785

projection view for the line-shape type or the C-shape type, but for the S-shape type, the probability of appearing on the coronary plane was relatively higher than on the other two projection planes.

The shapes of the vessel projection on the three views were not independent. The shape classifications (the permutation of shape type in the axial, coronary, and sagittal views) of the 717 M1 segments are listed in Table 2. There were 27 different shape classifications in the 3D orthogonal description of the M1 segment, but only 25 of these were found in the 717 cases because there was no case for some shape classifications. Some morphology had a very low probability of arising, for example, $P[\text{axial}=S, \text{coronary}=S, \text{sagittal}=L] < 0.003$, while some morphology had a very high probability of being detected (such as “CCC” and “LLL” permutations, whose appearance probabilities were over 0.15).

The proportion of the different spatial shape groups of the M1 segment is illustrated in Fig. 4. The LLL pattern on the top of the legend is for when the vessel looks like a straight line, an occurrence that had a proportion of 17 %. Other shapes are not straight in space but are curved from some viewpoints. Sometimes, M1 segments lay on a certain plane, and sometimes, they were tortuous in space. If a vessel looks like a line from only one or two orthogonal views, such as CLL and LCC, the vessel is in a curved pattern, and it is a plane curve, which lies in a single plane. Otherwise, if a vessel does not look like a line from any view, such as CCC, the vessel may be a spatial curve. It was found that about 60.8 % of M1 segment vessels were plane curves (including curves and straight lines) and that nearly 40 % of M1 segment vessels were tortuous in space, i.e., they were spatial curves with a greater tortuosity than plane curves. For vessels tortuous in space, S-tortuosity appeared more frequently.

The proportions of each spatial shape group in all age groups were compared. It was found that the degree of tortuosity changed with age. Five major spatial groups were selected from the ten groups, whose proportions in all subjects were larger than 10 %. The changes of the proportion for these five shape groups are shown in a stacked area chart (Fig. 5). These five major shape groups covered over 70 % of the samples in every age group. The top spatial shape group (including SCS, SSC, and CSS), which is shown by the light

Table 2 The rate of the shape classifications of the M1 segments in the three-view method

Shape classifications ^a	Count	Rate (%)	Shape classification	Count	Rate (%)
LLL	124	17.29	CCS	11	1.53
LLC	16	2.23	CSL	4	0.56
LLS	3	0.42	CSC	31	4.32
LCL	33	4.60	CSS	61	8.51
LCC	61	8.51	SLL	10	1.39
LCS	9	1.26	SLC	2	0.28
LSL	14	1.95	SLS	0	0.00
LSC	34	4.74	SCL	4	0.56
LSS	18	2.51	SCC	20	2.79
CLL	61	8.51	SCS	8	1.12
CLC	24	3.35	SSL	2	0.28
CLS	0	0.00	SSC	14	1.95
CCL	17	2.37	SSS	18	2.51
CCC	118	16.46			

^a The permutation of shape type on axial, coronary and sagittal planes, where L stands for line shape, C for C shape, and S for S shape

blue bar, was the group with the greatest tortuosity in these five groups. The bottom spatial shape group (LLL), which is shown by the deep blue bar, was the group with the least tortuosity. It can be seen that the proportion of the spatial shape group, LLL, decreased with age, while the proportion of the greatest tortuous shape group (SCS, SSC, and CSS) increased with age. Additionally, the proportion of the shape group CCC increased with age and then decreased slightly. No obvious trend was seen in other shape groups.

Besides the qualitative shape analysis, the feature parameters of the projected vessels were measured on axial and coronary MIP images, including the internal diameter of the M1 segment (Table 3). With measured feature parameters, the projection functions were used to fit the projected skeletal line of the M1 segment and to reconstruct the geometric 3D model.

In validation, 12 M1 segments were reconstructed by the three-view method and compared with the standard models derived from Mimics. Though the rough surface of the vessel

was neglected, the reconstructed 3D geometric models were consistent with the models from Mimics. The relative error of this method was 10.81 ± 2.78 %. The measurements and the reconstructions of two typical cases are shown in Figs. 6 and 7, including the description of the C-shape type, the line-shape type, and S-shape type.

Discussion

The M1 segment is of great clinical importance, and there is a variety of literature reporting its features [15, 17]. Zurada et al. [17] analyzed the 3D morphology of the M1 segment using angiographic computed tomography. They measured and calculated the internal diameter, length, volume, tortuosity index (TI), and deviation index (DI) of the M1 segment using the vascular skeleton processed by a 3D volume-rendering algorithm. Although TI and DI are very useful in describing the tortuosity of the vessel, the information about the vascular shape is also important for clinics, especially during neurointerventional procedures. Thus, this study focused on the shape information of the M1 segment. The MIP images from the clinic were used in the three-view method, so it is convenient for clinicians to describe the shape of the M1 segment quantitatively.

In our study, M1 segment images were taken using 3D-TOF MRA from over 400 participants. Except for visible vascular pathology and variations, which were not considered in our study, 717 M1 segments (including left M1 and right M1 segments) were described by the three-view method. Though there are noticeable differences between individuals, all M1 segments could be described as line-, S- or C-shapes from orthogonal views. Abnormal shape patterns had been

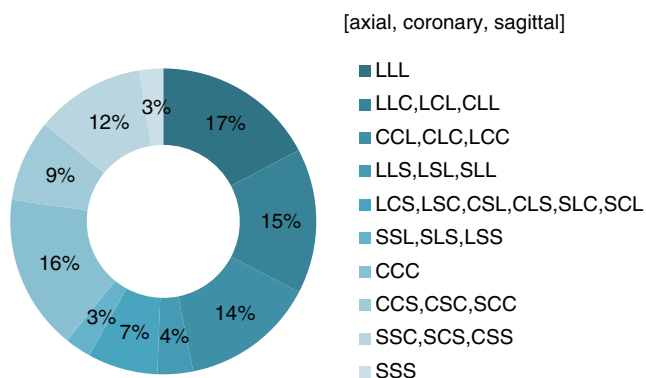
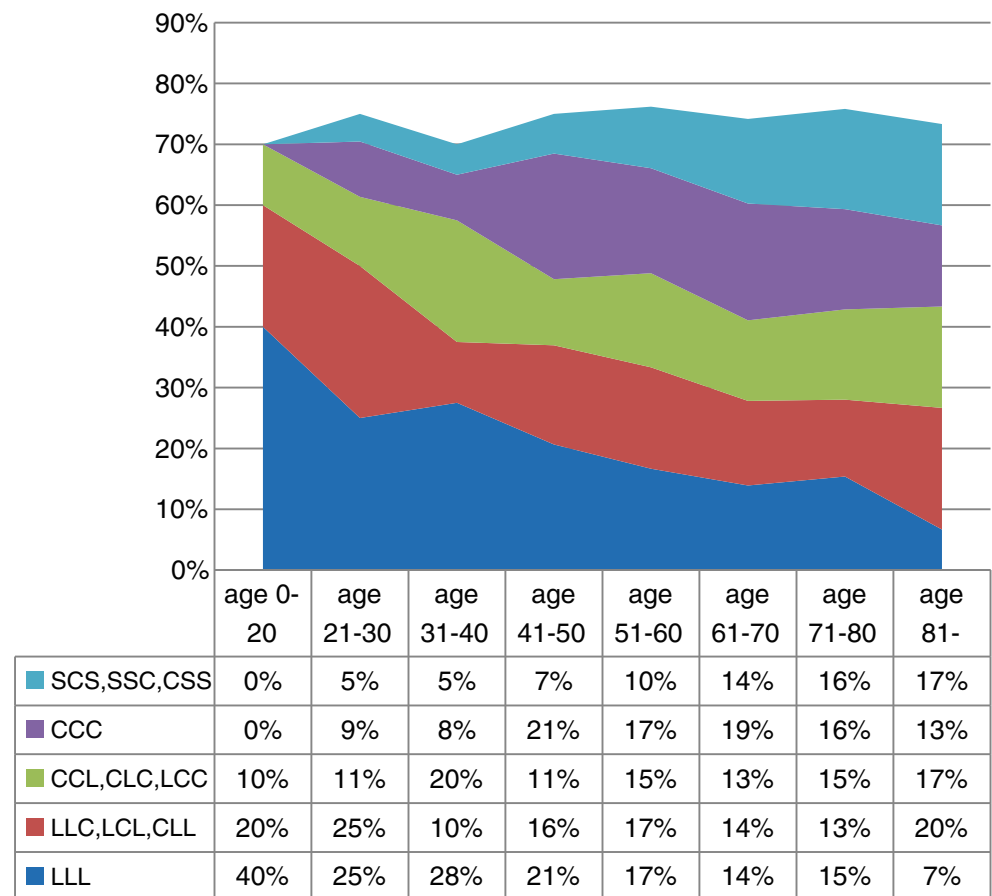


Fig. 4 The proportion of the spatial shape groups classified from shape classifications for their similar morphology. The spatial shape groups are listed according to the degree of tortuosity in space

Fig. 5 Changes in proportion for the five major spatial shape groups across different age groups. The area of each colored bar displays the trend of the proportion of these five shape groups over the age groups. The shape groups are listed according to the degree of tortuosity



considered such as V-shape and M-shape, which would be difficult to describe by a line-, C-, or S-shape type; fortunately, no M1 segment was found with such abnormal shapes. This study focused on the trunk shape description of the M1 segment, including the changes in caliber. Though the branches are also parts of the shape description, endovascular procedures are rarely performed in the branches, so only the trunk shape of the M1 segment was considered.

The M1 segment often appears to be straight and is called the horizontal segment of the vessel, but the linear pattern is not present in all cases. The vascular morphology varies. From the data we observed, only 17.29 % of the M1 segments were straight. Many M1 segments were noticeably bent in 3D space, though some of them may look like a line from one viewpoint. The course patterns of M1 segments may also

appear with C-shape or S-shape patterns. The three-view method may help us to classify them accordingly.

In this study, the changes in proportion for each shape group were found. The proportion of the spatial shape group LLL was higher in younger participants than that in elderly participants, while the proportion of the more tortuous spatial shape group was higher in elderly participants than that in younger participants. We suppose that the degree of tortuosity of the M1 segment increases with age because the proportion of straight vessels decreases with age and the proportion of the most tortuous vessels increases with age. The spatial shape group CCC has medium tortuosity. The results that the proportion of shape group CCC decreased slightly after 70, could be explained by an increase in more tortuous vessels such as SCS shape classification which enhanced with age. As for

Table 3 The measurement of the internal diameter at the proximal, middle, and distal parts of the M1 segment (mean±SD)

(mm)	Left		Right	
	From transection plane	From coronal plane	From transection plane	From coronal plane
Proximal part	2.89±0.26	2.97±0.24	2.90±0.22	2.94±0.24
Middle part	2.85±0.26	2.94±0.23	2.86±0.23	2.91±0.23
Distal part	2.82±0.24	2.93±0.27	2.85±0.23	2.91±0.24

Fig. 6 The validation of the three-view method for one case. **a** Measurement on axial MIP image. **b** Measurement on coronary MIP images. **c** The axial view of the geometric model from Mimics. **d** The coronary view of the geometric model from Mimics. **e** The axial view of the reconstructed model from the three-view method. **f** The coronary view of the reconstructed model from the three-view method

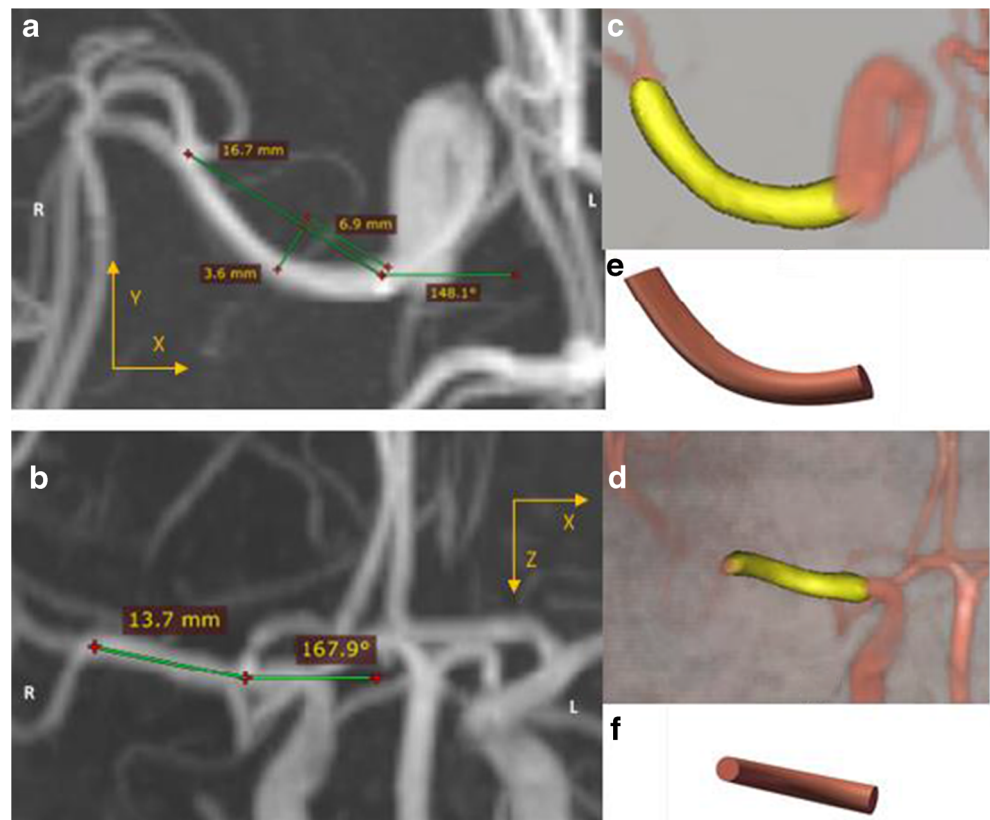
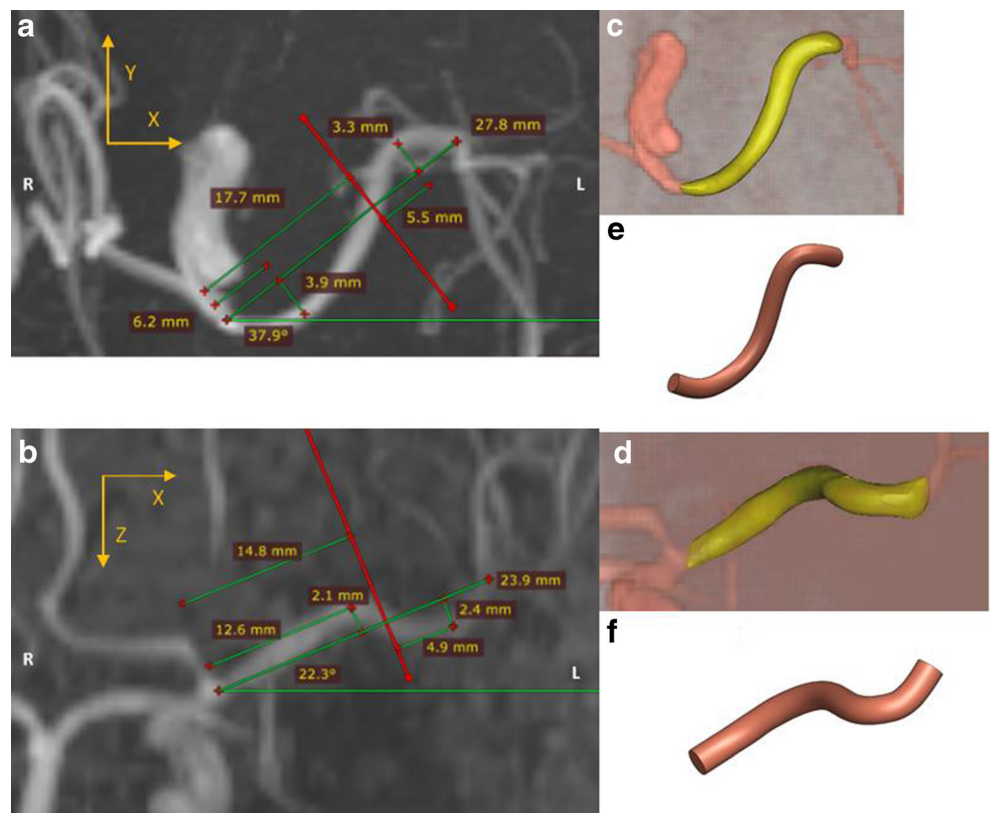


Fig. 7 The validation of the three-view method for another case. **a** Measurement on axial MIP image. **b** Measurement on coronary MIP images. **c** The axial view of the geometric model from Mimics. **d** The coronary view of the geometric model from Mimics. **e** The axial view of the reconstructed model from the three-view method. **f** The coronary view of the reconstructed model from the three-view method



other shape groups, they are also in the middle tortuosity level. The increased number of participants was similar to the decreased number in these groups with age. Thus, no obvious changes were found in these groups.

The tortuosity of the vessel is important for endovascular procedures. Mori et al. [32] has used the length, the angulated lesions, and other characteristics to describe the intracranial artery stenosis. The clinical success rate and the cumulative risks have relationships with the morphology of the vessel, especially tortuosity. For Mori's type A group, with short and nonangulated lesions, the clinical success rate was 92 %, and the cumulative risk was 8 %. For the type C group, with long and extremely angulated ($>90^\circ$) lesions with excessive tortuosity of the proximal segment, the clinical success rate was 33 %, and the cumulative risk was 87 %. Quantitative shape analysis could depict the tortuosity of the vessel in detail, so the shape analysis is significant for successful endovascular recanalization procedures. Thus, in this paper, we studied a method for the shape analysis, which could quantitatively describe the spatial shape of the vessel.

Compared with existing methods that also describe vascular morphology [17, 33, 15], the three-view method focused on the shape analysis of the M1 segment, could produce the quantitative 3D description of the M1 segment, and could be used to reconstruct the 3D model. Therefore, this method may establish a bridge between anatomic shape analysis and computational fluid analysis. The geometric vessel model, which is the basis of analyzing flow patterns and wall shear stress distribution, could be easily modified by adjusting the parameters derived from the three-view method. Thus, the three-view method can provide an approach to study the relationship between morphology and blood flow characteristics and can be used to assist in diagnosis and risk prediction. Although different degrees of tortuosity have been detected in this study, whether the tortuosity of the M1 segment has a relationship with cerebrovascular diseases is not clear. Further research will address the shape classification of M1 segments in pathological change, and computational fluid analysis will be performed to compare vessels of different degrees of tortuosity.

Conclusion

A detailed knowledge of 3D quantitative descriptions of the M1 segment is important when planning neurosurgical procedures and predicting risk. A three-view method, concerning shape information, was established to describe the M1 segment of the middle cerebral artery. The spatial shape of the M1 segment could be qualitatively described by shape classifications on three orthogonal planes. With the measurements of feature point and standard functions, the M1 segment can be quantitatively described and reconstructed. The probability distribution for the shape of the M1 segment was reported.

Acknowledgments This work was supported by National Nature Science Foundation of China (Grant No.81101123, No. 61108084, No. 61201313, No. 61190125), National Key Technology R&D Program (Grant No.2012BAI14B04) and the Fundamental Research Funds for the Central Universities of China.

Conflict of interest We declare we have no conflict of interest.

Ethical standards and patient consent We declare that all human studies have been approved by Medical Ethics Committee of Peking University Third Hospital and have therefore been performed in accordance with the ethical standards laid down in the 1964 Declaration of Helsinki and its later amendments. We declare that all patients gave informed consent prior to inclusion in this study.

Appendix

It is clear that the projection functions can be discussed in normal form by spinning the coordinate axis with a rotation angle γ and the final function $y=f(x)$ can be obtained by rotation transform, as shown in Eq. (1).

$$\begin{bmatrix} x \\ y \end{bmatrix} = \begin{bmatrix} \cos\gamma & \sin\gamma \\ -\sin\gamma & \cos\gamma \end{bmatrix} \begin{bmatrix} \hat{x} \\ \hat{y} \end{bmatrix} \quad (1)$$

The functions for C-shape vessel projections

The C-shape vessel projection was represented by cubic curves. For the C-shape, the parameter α was the quotient of L_1 and L_C , which was used to describe the relative deviation of the arch peak. The parameter β was the quotient of h_1 and L_C , which described the deviation on the project image. When α was less than $2/3$ but greater than $1/3$, the skeletal line of the vascular projection could be interpolated by a cubic curve as shown in Eq. (4), where x is the distance along the baseline from the origin.

$$\alpha = L_1/L_C \quad (2)$$

$$\beta = h_1/L_C \quad (3)$$

$$g_C(\hat{x}) = a\hat{x}^3 + b\hat{x}^2 + c\hat{x} + d \quad \frac{1}{3} < \alpha < \frac{2}{3} \quad (4)$$

$$\begin{cases} a = \frac{(1-2\alpha)\beta}{L_C^2\alpha^2(-1+\alpha)^2} \\ b = \frac{(-1+3\alpha^2)\beta}{L_C(-1+\alpha)^2\alpha^2} \\ c = \frac{(2-3\alpha)\beta}{(-1+\alpha)^2\alpha} \\ d = 0 \end{cases} \quad (5)$$

If α is greater than $2/3$ or less than $1/3$, the skeletal line should be described using a piecewise cubic curve. Fitting a single cubic polynomial to the irregular vessel was sometimes likely to yield unsatisfactory oscillating

behavior in the interpolation, so piecewise polynomial interpolation was used to solve this problem. The position of the unsatisfactory zero-crossing was termed L^* .

$$\text{if } \alpha < \frac{1}{3} \quad \begin{cases} g_C(\widehat{x}) = a\widehat{x}^3 + b\widehat{x}^2 + c\widehat{x} + d & 0 < \widehat{x} < L_1 \\ g_C(\widehat{x}) = a\left(\frac{(\widehat{x}-L_1)L^*}{L_C-L_1}\right)^3 + b\left(\frac{(\widehat{x}-L_1)L^*}{L_C-L_1}\right)^2 + c\frac{(\widehat{x}-L_1)L^*}{L_C-L_1} + d & L_1 < \widehat{x} < L_C \end{cases} \quad (6)$$

$$\text{if } \alpha > \frac{2}{3} \quad \begin{cases} g_C(\widehat{x}) = a\left(\frac{(\widehat{x}-L_1)L^*}{L_C-L_1}\right)^3 + b\left(\frac{(\widehat{x}-L_1)L^*}{L_C-L_1}\right)^2 + c\frac{(\widehat{x}-L_1)L^*}{L_C-L_1} + d & 0 < \widehat{x} < L_1 \\ g_C(\widehat{x}) = a\widehat{x}^3 + b\widehat{x}^2 + c\widehat{x} + d & L_1 < \widehat{x} < L_C \end{cases} \quad (7)$$

The functions for S-shape vessel projections

The S-shape vascular projection could be divided into two parts where the curve crosses the baseline, leaving two C-shaped curves. The function of the skeletal line in an S-shaped projection is a piecewise function g_S . The first part of the skeletal line could be treated as a C-shaped curve.

$$\alpha_1 = L_{11}/L_{S1} \quad (8)$$

$$\beta_1 = h_{11}/L_{S1} \quad (9)$$

$$g_S = \begin{cases} g_{S-1} & 0 < \widehat{x} < L_{S1} \\ g_{S-2} & L_{S1} \leq \widehat{x} < L_S \end{cases} \quad (10)$$

With α_1 , β_1 , and the function g_{S-1} forming the first part of an S-shaped skeletal line, the first derivative of the S-midpoint could be calculated. Then, the second part could be fitted by a quartic curve:

$$\alpha_2 = \frac{L_{21}}{L_S - L_{S1}} = \frac{L_{21}}{L_{S2}} \quad (11)$$

$$\beta_2 = \frac{h_{21}}{L_S - L_{S1}} = \frac{h_{21}}{L_{S2}} \quad (12)$$

$$\tau_{\text{mid-s}} = \frac{(-1 + 3\alpha_1)\beta_1}{(-1 + \alpha_1)\alpha_1^2} \quad (13)$$

$$g_{S-2}(x) = a_2\left(\frac{\widehat{x} - L_{S1}}{L_S - L_{S1}}\right)^4 + b_2\left(\frac{\widehat{x} - L_{S1}}{L_S - L_{S1}}\right)^3 + c_2\left(\frac{\widehat{x} - L_{S1}}{L_S - L_{S1}}\right)^2 + d_2\left(\frac{\widehat{x} - L_{S1}}{L_S - L_{S1}}\right) + e_2 \quad (14)$$

$$\begin{cases} a_2 = \frac{\beta_2^3(-2\tau_{\text{mid-s}}\alpha_2^2 + \tau_{\text{mid-s}}\alpha_2^3 + \alpha_2(\tau_{\text{mid-s}} - 3\beta_2) + 2\beta_2)}{h_{21}^3(-1 + \alpha_2)^2\alpha_2^3} \\ b_2 = -\frac{\beta_2^2(\tau_{\text{mid-s}}\alpha_2 - 3\tau_{\text{mid-s}}\alpha_2^3 + 2\tau_{\text{mid-s}}\alpha_2^4 + 2\beta_2 - 4\alpha_2^2\beta_2)}{h_{21}^2(-1 + \alpha_2)^2\alpha_2^3} \\ c_2 = \frac{(3\tau_{\text{mid-s}}\alpha_2^2 - \tau_{\text{mid-s}}\alpha_2^4 - 2\alpha_2(\tau_{\text{mid-s}} - 2\beta_2) - 3\beta_2)\beta_2}{h_{21}(\alpha_2 - 1)^2\alpha_2^2} \\ d_2 = \tau_{\text{mid-s}} \\ e_2 = 0 \end{cases} \quad (15)$$

References

- Mazighi M, Tanasescu R, Ducrocq X, Vicaut E, Bracard S, Houdart E, Woimant F (2006) Prospective study of symptomatic atherothrombotic intracranial stenoses—The GESICA Study. *Neurology* 66(8):1187–1191. doi:10.1212/01.wnl.0000208404.94585.b2

2. Sanchez-Sanchez C, Egido JA, Gonzalez-Gutierrez JL, Mera-Campillo J, Carneado-Ruiz J, Diaz-Otero F (2004) Stroke and intracranial stenosis: clinical profile in a series of 134 patients in Spain. *Rev Neurol* 39(4):305–311
3. Jiang W-J, Wang Y-J, Du B, Wang S-X, Wang G-H, Jin M, Dai J-P (2004) Stenting of symptomatic M1 stenosis of middle cerebral artery: an initial experience of 40 patients. *Stroke* 35(6):1375–1380
4. Vergouwen MI, Silver FL, Mandell DM, Mikulis DJ, Swartz RH (2011) Eccentric narrowing and enhancement of symptomatic middle cerebral artery stenoses in patients with recent ischemic stroke. *Arch Neurol* 68(3):338–342. doi:10.1001/archneurol.2011.20
5. Iwama T, Yoshimura S, Kaku Y, Sakai N (2004) Considerations in the surgical treatment of superior-wall type aneurysm at the proximal (M1) segment of the middle cerebral artery. *Acta Neurochir* 146(9):967–972. doi:10.1007/s00701-004-0325-1
6. Gibo H, Carver CC, Rhoton AL, Lenkey C, Mitchell RJ (1981) Microsurgical anatomy of the middle cerebral artery. *J Neurosurg* 54(2):151–169. doi:10.3171/jns.1981.54.2.0151
7. Türe U, Yasargil MG, Al-Mefty O, Yasargil DCH (2000) Arteries of the insula. *J Neurosurg* 92(4):676–687. doi:10.3171/jns.2000.92.4.0676
8. Yasargil MG (2011) Microsurgery: applied to neurosurgery. Thieme
9. Lasjaunias P, Berenstein A, Brugge K (2001) Clinical Vascular Anatomy and Variations: 1 Clinical Vascular Anatomy and Variations. Springer
10. Ulm AJ, Fautheree GL, Tanriover N, Russo A, Albanese E, Rhoton AL, Mericle RA, Lewis SB (2008) Microsurgical and angiographic anatomy of middle cerebral artery aneurysms: prevalence and significance of early branch aneurysms. *Neurosurgery* 62(5):344–352. doi:10.1227/01.neu.0000310700.14628.ae
11. Morris P (2007) Practical neuroangiography. 2nd edn. Lippincott Williams & Wilkins, Philadelphia
12. Osborn AG (1999) Diagnostic cerebral angiography. 2nd edn. Lippincott Williams & Wilkins, Philadelphia
13. Xu WH (2011) Plaque distribution of stenotic middle cerebral artery and its clinical relevance. *Stroke* 42(10):2957
14. Kiresi D, Gumus S, Cengiz SL, Cicekcibasi A (2009) The morphometric analysis of the V2 and V3 segments of the vertebral artery: normal values on MDCT. *Comput Med Imaging Graph* 33(5):399–407
15. Vuillier F, Medeiros E, Moulin T, Cattin F, Bonneville J-F, Tatu L (2008) Main anatomical features of the M1 segment of the middle cerebral artery: a 3D time-of-flight magnetic resonance angiography at 3 T study. *Surg Radiol Anat* 30(6):509–514
16. Zurada A, Gielecki J, Tubbs RS, Loukas M, Maksymowicz W, Chlebiej M, Cohen-Gadol AA, Zawilinski J, Nowak D, Michalak M (2011) Detailed 3D-morphometry of the anterior communicating artery: potential clinical and neurosurgical implications. *Surg Radiol Anat* 33(6):531–538
17. Zurada A, Gielecki J, Tubbs RS, Loukas M, Maksymowicz W, Cohen-Gadol AA, Michalak M, Chlebiej M, Zurada-Zielinska A (2011) Three-dimensional morphometrical analysis of the M1 segment of the middle cerebral artery: potential clinical and neurosurgical implications. *Clin Anat* 24(1):34–46
18. Zurada A, St Gielecki J, Tubbs RS, Loukas M, Zurada-Zielinska A, Maksymowicz W, Nowak D, Cohen-Gadol AA (2010) Three-dimensional morphometry of the A1 segment of the anterior cerebral artery with neurosurgical relevance. *Neurosurgery* 67(6):1768–1782
19. Zurada A, Gielecki J, Tubbs RS, Loukas M, Cohen-Gadol AA, Chlebiej M, Maksymowicz W, Nowak D, Zawilinski J, Michalak M (2010) Three-dimensional morphometry of the A2 segment of the anterior cerebral artery with neurosurgical relevance. *Clin Anat* 23(7):759–769
20. Gielecki JS, Zurada A, Gajda G, Nowak D, Sienkiewicz-Zawilinska J (2008) The description of vascular variations in three-dimensional space: a novel method of spatial cerebral arteries evaluation. *Med Sci Monit* 14(9):MT36–MT41
21. Zhang C, Xie S, Li S, Pu F, Deng X, Fan Y, Li D (2012) Flow patterns and wall shear stress distribution in human internal carotid arteries: the geometric effect on the risk for stenoses. *J Biomech* 45(1):83–89. doi:10.1016/j.jbiomech.2011.10.001
22. Datir P, Lee AY, Lamm SD, Han H-C (2011) Effects of geometric variations on the buckling of arteries. *Int J Appl Mech* 3(2):385–406. doi:10.1142/s1758825111001044
23. Fuster V, Badimon JJ, Chesebro JH (1998) Atherothrombosis: mechanisms and clinical therapeutic approaches. *Vasc Med* (London, England) 3(3):231–239. doi:10.1177/1358836x9800300310
24. Yasargil GM, Krisht AF, Türe U, Al-Mefty O, Yasargil DCH (2002) Microsurgery of insular gliomas: part I surgical anatomy of the sylvian cistern. *Contemp Neurosurg* 24(11):1–8
25. Fan Y, Xu Z, Jiang W, Deng X, Wang K, Sun A (2008) An S-type bypass can improve the hemodynamics in the bypassed arteries and suppress intimal hyperplasia along the host artery floor. *J Biomech* 41(11):2498–2505. doi:10.1016/j.jbiomech.2008.05.008
26. Bogunovic H, Maria Pozo J, Cardenes R, Cruz Villa-Urriol M, Blanc R, Piotin M, Frangi AF (2012) Automated landmarking and geometric characterization of the carotid siphon. *Med Image Anal* 16(4):889–903
27. Bouissou H, Emery MC, Sorbara R (1975) Age related changes of the middle cerebral artery and a comparison with the radial and coronary artery. *Angiology* 26(3):257–268. doi:10.1177/00031977502600303
28. Uchino A, Saito N, Okada Y, Nakajima R (2012) Duplicate origin and fenestration of the middle cerebral artery on MR angiography. *Surgical and Radiologic Anatomy* 34 (5):401–404
29. Uchino A, Takase Y, Nomiya K, Egashira R, Kudo S (2006) Fenestration of the middle cerebral artery detected by MR angiography. *Magnetic Resonance in Medical Sciences* 5 (1):51–55
30. Teal JS, Rumbaugh CL, Bergeron RT, Segall HD (1973) Anomalies of the middle cerebral artery: accessory artery, duplication, and early bifurcation. *The American journal of roentgenology, radium therapy, and nuclear medicine* 118 (3):567–575
31. Newman WM, Sproull RF (1979) Principles of interactive computer graphics. McGraw-Hill computer science series. McGraw-Hill
32. Mori T, Fukuoka M, Kazita K, Mori K (1998) Follow-up study after intracranial percutaneous transluminal cerebral balloon angioplasty. *AJNR Am J Neuroradiol* 19(8):1525–1533
33. Liu Q, Lu JP, Wang F, Wang L, Jin AG, Wang J, Tian JM (2009) Detection of anomalous splenic artery aneurysms with three-dimensional contrast-enhanced MR angiography. *Abdom Imaging* 34(6):772–776



A study of the metabolism of transplanted tumor in the lung by micro PET/CT in mice

Huiting Qiao^a, Jun Li^b, Yingmao Chen^c, Daifa Wang^a, Jintao Han^d, Mengqi Mei^a,
Deyu Li^{a,*}

^a Key Laboratory for Biomechanics and Mechanobiology of Ministry of Education, School of Biological Science and Medical Engineering, Beihang University, Beijing 100191, China

^b Peking University Laboratory Animal Centre, Peking University, Beijing 100871, China

^c Department of Nuclear Medicine, General Hospital of PLA, Beijing 100853, China

^d Department of Interventional Radiology and Vascular Surgery, Peking University Third Hospital, Beijing 100191, China

ARTICLE INFO

Article history:

Received 5 January 2013

Received in revised form 12 August 2013

Accepted 12 November 2013

Keywords:

Micro PET/CT

Metabolic model

Tumor

Dynamic scan

ABSTRACT

The difference of tumor metabolism from that of normal tissue is an important factor for diagnosis through functional imaging such as positron emission tomography (PET). A quantitative description of the metabolic process will help to improve the diagnosis methods. In this study, the metabolism of tumor in lung was quantitatively described in mice. The melanoma was transplanted into the lung of mice, and the metabolism of the transplanted tumor was detected by micro PET/CT with [¹⁸F]fluoro-2-deoxy-D-glucose (FDG). Nine mice were transplanted with B16 melanoma cells through their tail vein. Lung tumor was detected by pathological method. The lesions smaller than 1 mm could hardly be directly detected directly by micro PET/CT, while the tumor with a 1–4 mm diameter could be detected by micro PET/CT. A metabolic model with three compartments was separately established for lung tumors and normal lung tissues. In this model, the lung cancer had a significantly higher metabolic rate constant as compared to that of the normal lung tissue ($p=0.01$). The outputs of the model fit well with the original curve from the dynamic images. It is also found that difference of tissue activity between tumors and normal lung tissues varied along scan time. Through this comparison, it was suggested that the difference in metabolism between the lung tissue and the tumor might contribute to the tumor diagnosis.

© 2013 IPPEM. Published by Elsevier Ltd. All rights reserved.

1. Introduction

Malignant tumor is one of the great threats to human health. Early detection and early treatment is the key to reduce the mortality from malignant tumors. The distinction between cancer and normal tissue is the base of an early detection. For example, the difference of glucose metabolism between the cancer and normal tissue is the basic principle of cancer detection by Positron emission tomography (PET) with [¹⁸F]fluoro-2-deoxy-D-glucose (FDG) [1,2]. To develop a technique for tumor detection, it is important to understand the metabolic character of different tissues and cancers. Therefore quantitative metabolic models have been established for and cancer [3] as well as normal tissue [4,5].

In the process for the development of methods and techniques for tumor detection and therapy, small animals, such as mice, have been widely used [6,7]. These animals could also be used to assess

the treatment effects through imaging and semi-quantitative analysis [8,9]. Although many tumor models have been used in small animals for biomedical research and PET imaging [10,11], a quantitative metabolic study is lacking for small animal. In this study, we quantitatively investigated the tumor metabolism in mice. Unlike the existing kinetic analysis for subcutaneous tumors [12], we studied a transplanted tumor in lung by micro PET/CT imaging in mice.

The study of tumor metabolism in mice could be of great importance in order to develop tumor PET detection. There are two ways to increase the sensitivity and specificity of the PET detection, including: finding specific tracer [13], and proposing optimized scan scheme according to the metabolic distinction of focus [14]. Some previous studies have already shown the potential usefulness of dynamic PET in detection [15], due to an increased metabolic distinction that can be achieved in dynamic imaging as compared to the static imaging [16]. To optimize the scanning scheme of the dynamic imaging, the development of a metabolic model in small animals is necessary. In this effort, quantitative metabolic models were separately established for lung tumors as well as normal lung tissues, and their distinction was further discussed.

* Corresponding author. Tel.: +86 10 82339490.

E-mail address: deyuli@buaa.edu.cn (D. Li).

2. Materials and methods

2.1. Experimental model

All procedures were reviewed and approved by Peking University's Animal Care and Use Committee. Nine 6–8-week-age c57 mice were obtained from the Peking University Laboratory Animal Centre. They were housed in conventional cages, and were given free access to food and water. Of those, 9 mice (4 males and 5 females) were injected through their tail veins with 0.2 ml of cultured B16 melanoma cells at the concentration of 5×10^6 cell/ml. These nine mice were divided into two groups, including: group A with three mice (1 male and 2 females), and group B with six mice (3 males and 3 females). The three mice of group A were scanned by micro PET/CT and were then sacrificed in 21 days after the injection in order to confirm the tumor in lung. The six mice in the group B were scanned by micro PET/CT in 28 days after the injection in order to establish a metabolic model. Upon sacrifice, the lungs were collected for pathologic evaluation to confirm the existence and the approximate position of the tumor. Tumors were detected in the lung of all these nine animals specifically in the liver for one case.

2.2. In vivo scanning

All the animals had a 10 h fasting before scanning. For in vivo scanning, mice were anesthetized with 1% isoflurane inhalation [17]. Each mouse was fixed on the scan bed in the prone position with all legs fully extended. The dynamic FDG-PET scans were performed on each mouse for one hour with Micro PET/CT (Explore Vista Micro PET/CT, GE healthcare, US), on a 6.8 cm field of view. Micro PET has a 1.2 mm spatial resolution, while Micro CT's spatial resolution is 100 μ m. For this study, the scan was performed in a single bed covering the chest. The FDG tracer (0.2–0.4 mCi) was then quickly injected quickly from the tail vein, followed by an immediate start of the PET scan [18]. In the sampling protocol, the dynamic imaging sequences consisted of six 10-s frames, six 20-s frames, eight 30-s frames, eight 60-s frames, seven 300-s frames, and one 600-s frames, totaling to 36 frames for a total scan time of 60 min.

2.3. Data acquirement

Micro PET/CT merges the functional image of PET and the anatomic of CT, which has made it possible to find the relative position of the region of interest (ROI). Normal lung tissue, lung tumor, myocardium and left ventricular tissue could be differentially detected with the dynamic micro PET/CT images. The ROI of these tissues was manually drawn on 3-D images. The time-activity curve was picked up from the ROI in each frame [19]. The radioactivity was calculated by averaging the entire voxel's values within the ROI. The blood time-activity curve (BTAC) was derived from the ROI in left ventricular tissue, and was modified based on the model of myocardium [20,21]. The normal lung tissue time-activity curve (TTAC) was derived from the ROI of the normal lung region, which was not closed to myocardium. The lung tumor tissue time-activity curve (TTAC) was derived from the ROI of the highlight region, which was determined to be the lung tumor and was pathological confirmed.

2.4. Model description

The compartment model (Fig. 1) was used to describe the tumor metabolism in mice, which has been successfully used to describe the metabolism of human myocardium, skeletal muscle, brain and different tumors [22–24]. In this model, the left compartment represented the vascular space for FDG, the center compartment

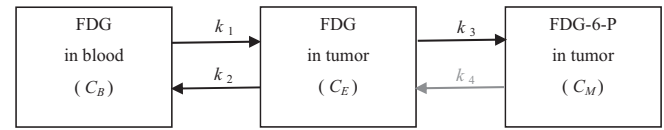


Fig. 1. The three-compartment model for FDG metabolism.

represented the lung tumor tissue space for free FDG and the right compartment represented the lung tumor tissue space for FDG-6-phosphate (FDG-6-P) [25]. The concentrations of FDG or FDG-6-P in the three compartments were C_B , C_E , and C_M respectively. The model parameters k_1 – k_4 were the rate constants of the mass exchange between compartments. For the lung tissue, the dephosphorylation was ignored, so the k_4 rate constant was assumed to be zero [3,26].

Since the radioactivity of ^{18}F was easy to detect and be converted to FDG concentration, the time activity curve (TAC) was used to express the FDG concentration. For example, the blood time activity curve (BTAC) was used as the input of the model as $C_B(t)$, which was the FDG blood concentration. In this compartment model, $C_T(t)$, the observed total tissue time activity curve (TTAC) in PET image can be described as following equations:

$$C_T(t) = C_E(t) + C_M(t) + f \cdot C_B(t) \quad (1)$$

$$C_T(t) = \frac{k_1 k_2}{k_2 + k_3} e^{-(k_2 + k_3)t} \otimes C_B(t) + \left(\frac{k_1 k_3}{k_2 + k_3} + f \right) \cdot C_B(t) \quad (2)$$

where \otimes denoted the operation of convolution, and f demonstrated the spillover fraction from blood to the lung.

In general, this compartment model for FDG-PET required the measurements of both BTAC and TTAC, which were input and output functions of the model. The parameters k_1 – k_3 with spillover fraction (f), were estimated by fitting the output function of the model.

This three compartment model was also used to describe the normal lung tissue metabolism.

2.5. Parameter estimation

The three compartment model was also used to fit the clinical data. With the measurements of $C_B(t)$ and $C_T(t)$ based on the dynamic micro PET/CT images, the weighted nonlinear least-squares algorithm was applied [27]. The model parameters were estimated by minimizing the weighted residual sum of squares (WRSS), where w_k was the weight (the inverses of the measurement error) [23], y was the output of the model using vector p parameters, and C_T from the dynamic data.

$$\text{WRSS}(p) = \sum_{k=1}^{36} w_k [y(t_k, p) - C_T(t_k)]^2 \quad (3)$$

To validate the fitting, the WRSS, R -square and parameter standard deviation were computed.

3. Results

Nine mice were scanned by micro PET/CT. In group A, the three mice were scanned 21 days after the injection of the B16 melanoma cells. No obvious abnormal tissues were detected in the micro PET/CT images as shown in Fig. 2. However, small tumors could be pathologically detected as shown in Fig. 3. In group B, six mice were scanned 28 days after injection of the B16 melanoma cells, where (one mouse died during the scan). Some highlighted regions were detected in combined micro PET/CT images as shown in Fig. 4. After

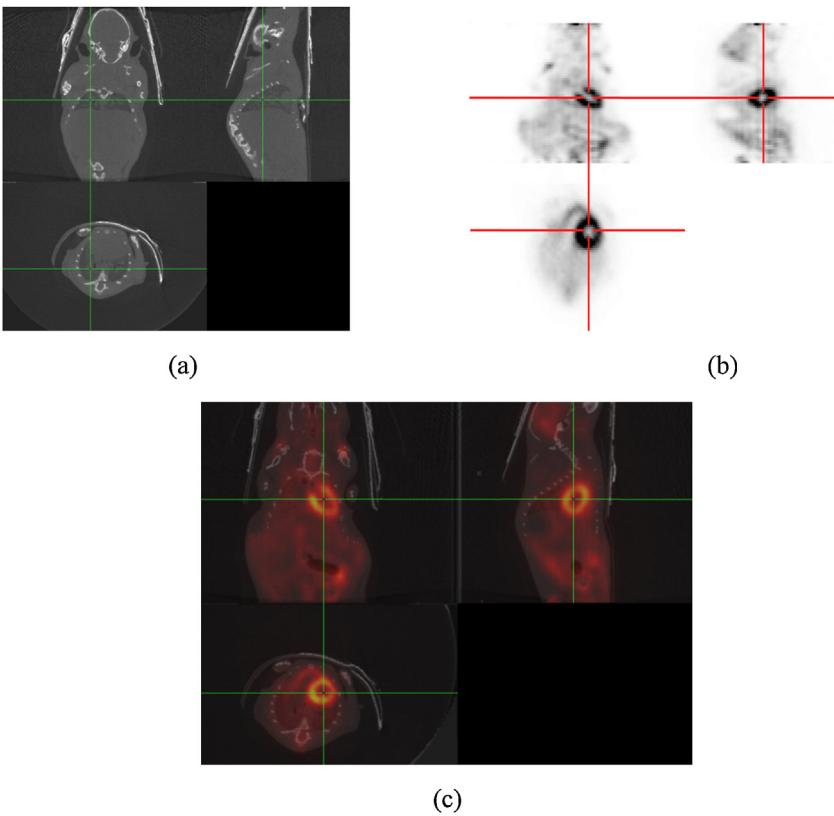


Fig. 2. The images of group A, where the left ventricular could be found. (a) CT image, (b) PET image and (c) fusion image.

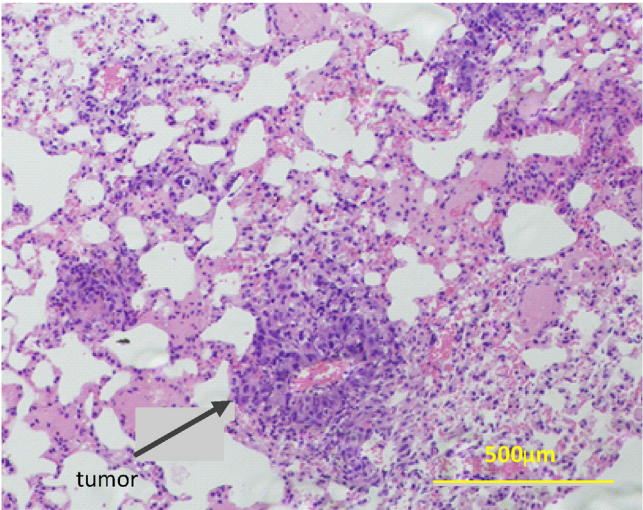


Fig. 3. The pathological slice of lung tissue from one mouse in group A.

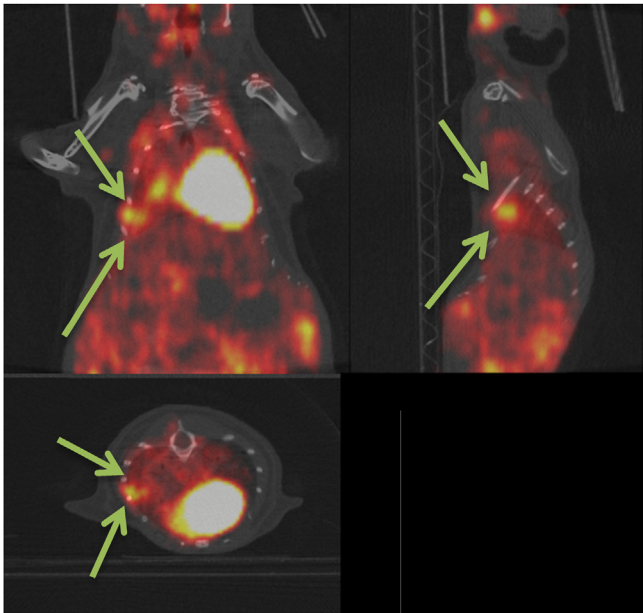


Fig. 4. The orthographic views of PET/CT image of a mouse with lung tumor.

the scan, all the mice were sacrificed in order to confirm the existence of the tumor. The tumor of 1–4 mm diameter was detected by microscope. One pathological slice is shown in Fig. 5.

For group B, the metabolic models were separately established for the tumor and normal lung tissues. All the time tissue activity curves of ROI were picked up from the combined micro PET/CT images. For each subject, the time activity curves of the normal lung tissue and lung tumor were picked up and were used to estimate the parameters of the metabolic model. The parameters for the lung tumor model were estimated by a nonlinear curve fitting method. The average and standard deviation (SD) for k_1 , k_2 , k_3 , and the net FDG phosphorylation rate (K) are presented in Table 1. The

Table 1
Estimated parameters of the tumor model.

	k_1	k_2	k_3	K
Subject 1	0.5303	0.0029	0.0231	0.47115
Subject 2	0.3478	0.0097	0.0218	0.2407
Subject 3	0.361	0.0055	0.0462	0.3226
Subject 4	0.4581	0.0054	0.029	0.3864
Subject 5	0.3976	0.0067	0.028	0.3208
Mean	0.4190	0.0060	0.0296	0.3483
SD	0.0746	0.0024	0.0097	0.0845

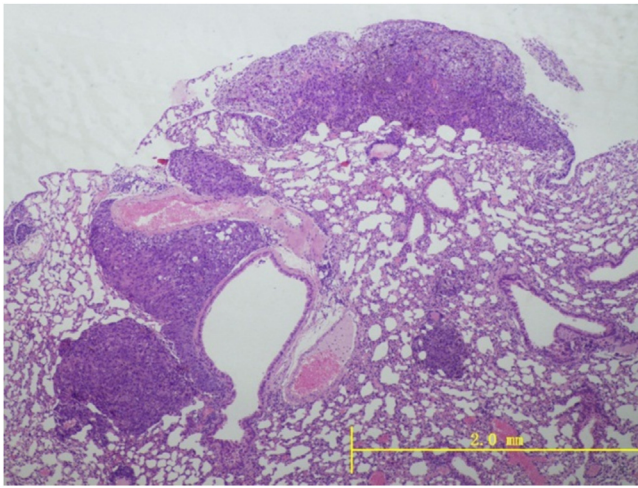


Fig. 5. The pathological slice of lung tissue from one mouse in group B.

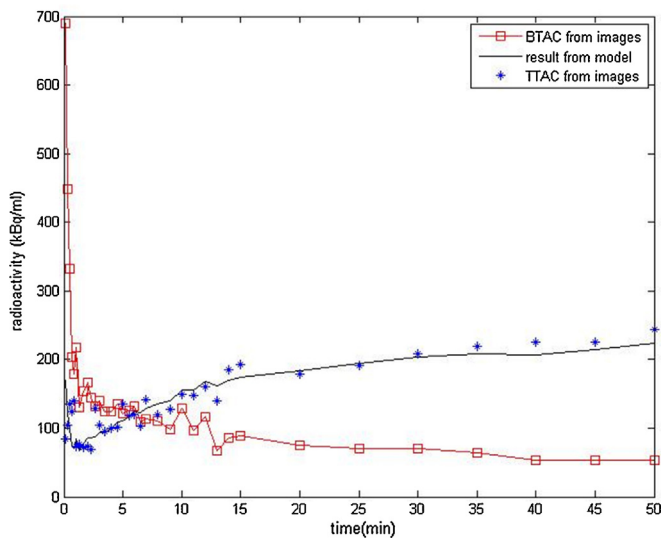


Fig. 6. The curve fitting results for tumor in lung.

R -square of 0.85 ± 0.10 demonstrated that the results of the model were consistent with the actual tissue time activity curves, since a value closer to 1 was supposed to indicate a better fit. The output of this model fit well with the original curve from the dynamic images, as shown in Fig. 6.

The parameters for the normal lung tissue model were estimated and compared with that of the tumor tissue, as shown in Table 2. To compare the difference between the tumor and normal tissues, the local pulmonary metabolic rate-constant of FDG (K) was calculated, which presented the net FDG phosphorylation rate.

$$K = \frac{k_1 k_3}{k_2 + k_3} \quad (4)$$

Table 2

The comparison of the kinetic parameters between tumor and the normal lung tissue.

	Tumor	Lung	P -value
k_1	0.4190 ± 0.0746	0.2491 ± 0.0586	0.005
k_2	0.0060 ± 0.0024	0.0263 ± 0.01498	0.03
k_3	0.0296 ± 0.0097	0.0760 ± 0.0095	<0.005
K	0.3483 ± 0.0845	0.1756 ± 0.0695	0.01

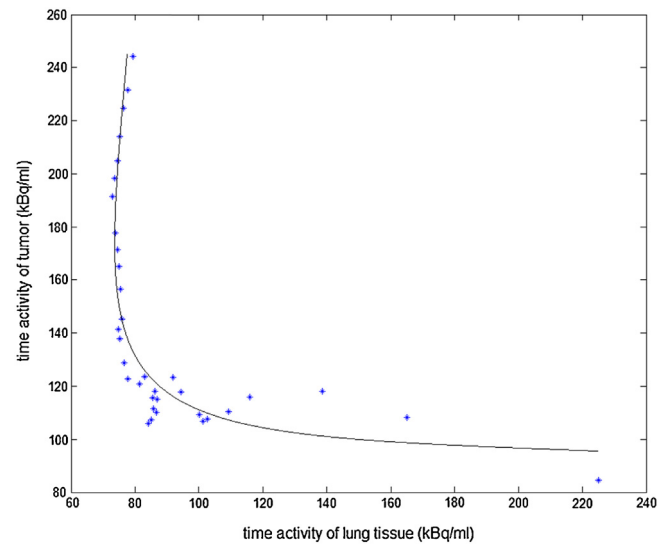


Fig. 7. The correlation between activity in lung and that in tumor.

Although the metabolic rate-constant of FDG varied for each subject in group B, the mean metabolic rate-constant of FDG for tumor was 0.3483 ± 0.0845 , which was larger than of the normal lung tissue (0.1756 ± 0.0695 , $p = 0.01$).

For each subject, there were different activity curve trends, besides the difference of the local pulmonary metabolic rate-constant of FDG. The correlation between the activity in normal lung v.s. that of tumor is shown in Fig. 7. Considering the dynamic metabolic process, the relationship among the activity in lung, activity in tumor and the scan time are shown in Fig. 8. According to the time course, the lung and tumor tissue activities and the difference between them varied. Therefore, the dynamic difference could also serve as a criterion for tumor diagnosis.

4. Discussion

Since the metabolism difference between the tumor and normal tissue was an efficient detection principle, the study of metabolism of tumor was necessary. To gather the metabolic data from the small animal, Micro PET/CT was used. The dynamic metabolic process was observed by PET, while CT had a higher resolution. Micro PET/CT combined the functional and anatomic images, which provided a convenient way to define ROI. The normal lung region was

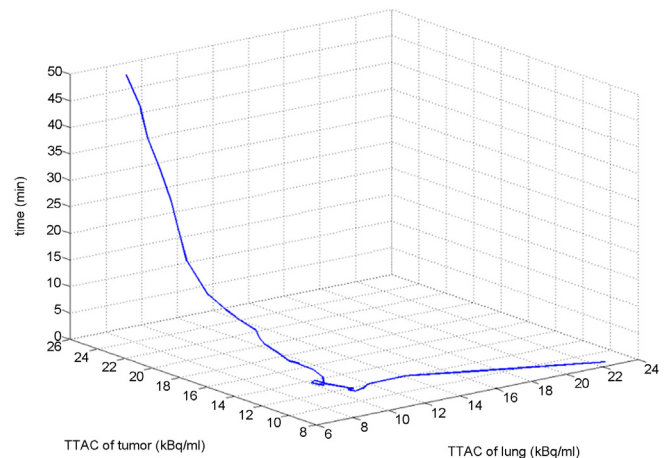


Fig. 8. The relationship among the activity in lung, activity in tumor and the scan time.

defined on the basis of the CT images. On the other hand, micro PET improved the imaging quality, which was correlated with the anatomic imaging obtained by CT scanning. Therefore, combined micro PET/CT was used instead of micro PET alone.

In this study, mice with transplantation tumors were chosen instead of mice with subcutaneous tumors in order to study the metabolism of lung tumor. Although the size and the metabolism of tumor varied for each subject, it was found that the breeding time after tumor cells injection was an important factor for micro PET/CT diagnosis. The main reason was the tumor size, such that it was hard to find the tumor by partial volume effect, when the tumor was too small. Therefore the early diagnosis of small tumor will still be a problem to solve even with the use of micro PET/CT.

The analysis performed on mice time activity curve showed that most curves became stable at about 15 min. The model parameters were also estimated with the data in 20 min. The same conclusion was reached showing that the tumor had a higher metabolic rate-constant of FDG as compared to that of the normal lung tissue. But the tumor metabolic rate-constant of FDG in the short scan schedule is a little lower than that of the long scan schedule, which is in line with the report of Torizuka [3]. Since the mice heart rate was about 5 times higher than that of human, it was supposed that mice should have a higher metabolic rate, based on which the dynamic imaging could be potentially shortened.

The different radioactivity relative to the surrounding tissues was the main criterion for PET/CT detection. In group A, the tumors were hard to detect in all the subjects, while the very small tumors were pathologically detected after animals were sacrificed. In group B, some high-lighted regions were found in the micro PET/CT images, which could be the potential focus of the tumor. Although the weighted nonlinear least-squares algorithm was validated [28], there was still some limitations of the quantitative model, such as the model simplification and ROI selection. The overlap between the tissues also impacted the accuracy of the quantitative model, based on which all the ROIs were chosen very cautiously. The overlap volume, such as the edge of the tumor, was not included in the ROI. Therefore, the impacts of overlap on parameter estimation were reduced.

In experiments with mice, the myocardial high metabolism [29] affected the lung tumor detection. Unlike human, the mice have a very high glucose metabolism in myocardium, so the myocardium presented as a high-light region in the micro PET/CT images. For some small tumors, the abnormal metabolism was less obvious, due to the high light of myocardium metabolism. Therefore, some tumors in the vicinity of the myocardium were covered.

Although it could be sometimes difficult to detect small tumors by micro PET/CT images due to their size and the myocardium effect, some other methods could be applied to process micro PET/CT images [16]. According to the variations in different tissue time activity curves, clustering and dynamic image segmentation might reveal the small tumors to some extents. The quantitative model could be used to simulate the dynamic imaging and to provide the theoretical support for diagnosis method development. Therefore, this quantitative metabolic model could be important for the further research in PET and PET/CT tumor detection area.

5. Conclusion

In summary, the transplanted tumor model could be estimated by tail vein injection in mice. The metabolic process of transplanted tumor could be detected by micro PET/CT with FDG. A mathematic model was established to quantitatively describe the tumor metabolism. The results were consistent with the tumor time activity curves from the micro PET/CT images. We concluded that the

quantitative model and dynamic metabolic character might be useful to improve early diagnose techniques.

Funding

This work was supported by National Nature Science Foundation of China (Grant Nos. 81101123, 61108084, 61227902), 111 project and the Fundamental Research Funds for the Central Universities of China.

Ethical approval

Not required.

Conflict of interest statement

None declared.

References

- [1] Rohren EM, Turkington TG, Coleman RE. Clinical applications of PET in oncology. *Radiology* 2004;231:305–32.
- [2] Higashi K, Matsunari I, Ueda Y, Ikeda R, Guo J, Oguchi M, et al. Value of whole-body FDG PET in management of lung cancer. *Annals of Nuclear Medicine* 2003;17(Febuary):1–14.
- [3] Torizuka T, Nobezawa S, Momiki S, Kasamatsu N, Kanno T, Yoshikawa E, et al. Short dynamic FDG-PET imaging protocol for patients with lung cancer. *European Journal of Nuclear Medicine* 2000;27(October):1538–42.
- [4] Cui Y, Bai J, Chen Y, Tian J. Parameter estimation for whole-body kinetic model of FDG metabolism. *Progress in Natural Science* 2006;16(November):1164–70.
- [5] Hays MT, Segall GM. A mathematical model for the distribution of fluorodeoxyglucose in humans. *Journal of Nuclear Medicine* 1999;40:1358–66.
- [6] Chow PL, Stout DB, Komisopoulou E, Chatzioannou AF. A method of image registration for small animal, multi-modality imaging. *Physics in Medicine and Biology* 2006;51(January):379–90.
- [7] de Kemp RA, Epstein FH, Catana C, Tsui BMW, Ritman EL. Small-animal molecular imaging methods. *Journal of Nuclear Medicine* 2010;51(May):185–32S.
- [8] Bretsch M, Cheng C, Witt H, Dimitrakopoulou-Strauss A, Strauss LG, Semmler W, et al. Cilengitide affects tumor compartment, vascularization and microenvironment in experimental bone metastases as shown by longitudinal F-18-FDG PET and gene expression analysis. *Journal of Cancer Research and Clinical Oncology* 2013;139(April):573–83.
- [9] Dunnwald LK, Doot RK, Specht JM, Gralow JR, Ellis GK, Livingston RB, et al. PET tumor metabolism in locally advanced breast cancer patients undergoing neoadjuvant chemotherapy: value of static versus kinetic measures of fluorodeoxyglucose uptake. *Clinical Cancer Research* 2011;17(April):2400–9.
- [10] Woo S-K, Kim KM, Lee TS, Jung JH, Kim JG, Kim JS, et al. Registration method for the detection of tumors in lung and liver using multimodal small animal imaging. *IEEE Transactions on Nuclear Science* 2009;56:1454–8.
- [11] Zhang T, Zhou N-K, Zhang J-m, Liang C-Y, Liu X, Tian X-D. Comparison of the biodistribution and PET imaging with (11)C-PDT and (18)F-FDG in the mouse model of lung adenocarcinoma. *Zhonghua zhong liu za zhi[nl]Chinese Journal of Oncology* 2010;32(Febuary):103–6.
- [12] Kim SJ, Lee JS, Im KC, Kim S-Y, Park S-A, Lee SJ, et al. Kinetic modeling of 3'-deoxy-3'-(18)F-fluorothymidine for quantitative cell proliferation imaging in subcutaneous tumor models in mice. *Journal of Nuclear Medicine* 2008;49(December):2057–66.
- [13] Rowe CC, Ackerman U, Browne W, Mulligan R, Pike KL, O'Keefe G, et al. Imaging of amyloid β in Alzheimer's disease with 18F-BAY94-9172, a novel PET tracer: proof of mechanism. *The Lancet Neurology* 2008;7:129–35.
- [14] Karakatsani NA, Lodge MA, Zhou Y, Mhlanga J, Chaudhry MA, Tahari AK, et al. Dynamic multi-bed FDG PET imaging: feasibility and optimization. In: *IEEE Nuclear Science Symposium and Medical Imaging Conference*. 2011. p. 3863–70.
- [15] Busk M, Munk OL, Jakobsen S, Wang T, Skals M, Steiniche T, et al. Assessing hypoxia in animal tumor models based on pharmacokinetic analysis of dynamic FAZA PET. *Acta Oncologica* 2010;49(October):922–33.
- [16] Qiao HT, Bai J, Chen YM, Tian JH. Method for tumor recognition with short dynamic PET images: theory and simulation study. *Progress in Natural Science* 2009;19:73–7.
- [17] Luu YK, Lublinsky S, Ozcivici E, Capilla E, Pessin JE, Rubin CT, et al. In vivo quantification of subcutaneous and visceral adiposity by micro-computed tomography in a small animal model. *Medical Engineering & Physics* 2009;31(January):34–41.
- [18] Woo S-K, Kim K, Lee T, Kim J, Jung J, Woo K, et al. Experimental condition and registration method for the tumor detection of lung metastasis small animal PET and CT whole body images. In: *Nuclear Science Symposium Conference Record. NSS'07. IEEE*. 2007. p. 3372–5.
- [19] Mabrouk R, Dubeau F, Bentourkia M, Bentabet L. Extraction of time activity curves from gated FDG-PET images for small animals' heart studies.

- Computerized Medical Imaging and Graphics: The Official Journal of the Computerized Medical Imaging Society 2012;36(September):484–91.
- [20] Li X, Feng D, Lin KP, Huang SC. Estimation of myocardial glucose utilisation with PET using the left ventricular time-activity curve as a non-invasive input function. *Medical & Biological Engineering & Computing* 1998;36(January):112–7.
 - [21] Kim J, Herrero P, Sharp T, Laforest R, Rowland DJ, Tai YC, et al. Minimally invasive method of determining blood input function from PET images in rodents. *Journal of Nuclear Medicine* 2006;47(February):330–6.
 - [22] Huang SC, Phelps ME, Hoffman EJ, Sideris K, Selin CJ, Kuhl DE. Noninvasive determination of local cerebral metabolic rate of glucose in man. *American Journal of Physiology – Endocrinology and Metabolism* 1980;238:E69–82.
 - [23] Bertoldo A, Vicini P, Sambucetti G, Lammertsma AA, Parodi O, Cobelli C. Evaluation of compartmental and spectral analysis models of [¹⁸F]FDG kinetics for heart and brain studies with PET. *IEEE Transaction on Biomedical Engineering* 1998;45(December):1429–48.
 - [24] Dimitrakopoulou-Strauss A, Hohenberger P, Pan L, Kasper B, Roumia S, Strauss LG. Dynamic PET With FDG in patients with unresectable aggressive fibromatosis: regression-based parametric images and correlation to the FDG kinetics based on a 2-tissue compartment model. *Clinical Nuclear Medicine* 2012;37:943–8.
 - [25] Epelbaum R, Frenkel A, Haddad R, Sikorski N, Strauss LG, Israel O, et al. Tumor aggressiveness and patient outcome in cancer of the pancreas assessed by dynamic F-18-FDG PET/CT. *Journal of Nuclear Medicine* 2013;54(January):12–8.
 - [26] Torizuka T, Zasadny KR, Recker B, Wahl RL. Untreated primary lung and breast cancers: correlation between F-18 FDG kinetic rate constants and findings of in vitro studies. *Radiology* 1998;207(June):767–74.
 - [27] Chen S, Feng D. Noninvasive quantification of the differential portal and arterial contribution to the liver blood supply from PET measurements using the 11C-Acetate kinetic model. *IEEE Transaction on Biomedical Engineering* 2004;51:1579–85.
 - [28] Cui YF, Bai J, Chen Y, Tian J. Kinetic model parameter estimates of liver FDG metabolism. *Qinghua Daxue Xuebao/Journal of Tsinghua University* 2007;47:420–3.
 - [29] Gallagher BM, Ansari A, Atkins H, Casella V, Christman DR, Fowler JS, et al. Radiopharmaceuticals XXVII. 18F-Labeled 2-deoxy-2-fluoro-D-glucose as a radiopharmaceutical for measuring regional myocardial glucose metabolism in vivo: tissue distribution and imaging studies in animals. *Journal of Nuclear Medicine* 1977;18(October):990–6.

The effect of tumor size on the imaging diagnosis: A study based on simulation

Huiting Qiao, Libin Wang, Deyu Li, Daifa Wang and Yu Wang*

School of Biological Science and Medical Engineering, Beihang University, Beijing 100191, China

Abstract. Positron emission tomography (PET) has been widely used in early diagnosis of tumors. Though standardized uptake value (SUV) is a common diagnosis index for PET, it will be affected by the size of the tumor. To explore how the tumor size affects imaging diagnosis index, dynamic PET images were simulated to study the relationship between tumor size and the imaging diagnosis index. It was found that the SUV of the region of the tumor varied with scan time, and the SUV was always lower than the true value of tumor. Even more deviations were found in SUV with a reduced tumor size. The diagnosis index SUV_{max} was more reliable than SUV, for it declined only when the volume of tumor was less than 3 mm^3 . Therefore, the effect of tumor size on the SUV and SUV_{max} that are used as diagnosis indices in the early diagnosis of tumors should not be neglected.

Keywords: Standardized uptake value, maximum standardized uptake value, positron emission tomography, tumor size, diagnosis

1. Introduction

As one of the most serious threats to life health, cancer is the second leading cause of death in developing countries. The number of people who are diagnosed with cancer and the mortality rates of people diagnosed with malignant tumor are still increasing in recent years [1,2]. It was reported that lung cancer was the leading cause of death in all the common cancer registries [3,4], and its mortality rate increased substantially in the past three years. Although there are some methods of oncologic treatment on clinical therapies, such as radiation, chemotherapy and surgery, it is still hard to improve the survival rate of lung cancer because of late diagnosis [5,6]. Therefore, early diagnosis is important to improve treatment and the survival rate of patients with lung cancer [7,8]. Imaging diagnosis [9] as well as identification of molecular biomarkers [10–12] have been used as two main methods in the studies of early diagnosis for lung cancer.

In terms of imaging diagnosis, positron emission tomography (PET) is the function imaging technology that can provide metabolism information of tissues by using a radioactive tracer [13]. Moreover, it is an important tool for staging, prognosis, evaluation of treatment, and, especially, for early diagnosis [14,15]. A tumor usually has a higher metabolic rate, so it can be recognized easily by using PET. Besides the visual cancer imaging, PET can also provide some detection indices for diagnosis,

*Corresponding author: Yu Wang, School of Biological Science and Medical Engineering, Beihang University, Beijing, China. Tel.: 82338755; Fax: 82315554; E-mail: wangyu@buaa.edu.cn.

treatment, such as total lesion glycolysis (TLG), standardized uptake value (SUV), and maximum standardized uptake value (SUV_{max}) [16].

SUV, which is widely used in the study of cancer, is a semi-quantitative measurement of radioactivity concentration [17]. SUV describes the ratio between the radioactive substances uptake of the lesion and the average uptake of the whole body [18]. SUV and SUV_{max} are different expressions of SUV. SUV refers to the mean SUV of the region of interest (ROI), while SUV_{max} is the maximal SUV in the ROI. SUV and SUV_{max} are often used as detection indices for early diagnosis of lung cancer. In order to study the different lung tumors and different study demands, researchers often choose different SUV value. Juhász et al. evaluated metabolic ratio and tracer transport of non-small cell lung cancers by using SUV [19]. Koh et al. studied the relationship between SUV and disease-free survival (DFS) and the relationship between SUV and overall survival (OS). DFS and OS are both evaluation indicators of the prognostic impact of the lung tumor patients receiving chemotherapy after surgery [20]. In Alessandro's study of solitary pulmonary nodule tumor, SUV_{max} was used to find significant difference or correlation [21]. Mehta also used SUV_{max} to study the research about the patients with non-small-cell lung cancer [16]. In MI B's research [22], $SUV=2.5$ is used as a threshold value to differentiate benign and malignant lesions. In addition, SUV_{max} of normal lung ranges from 1.0 to 1.5, which can be used as the threshold value to differentiate the normal lung tumor from lung tissue [23]. Thus, SUV and SUV_{max} were both studied in this paper as detection indices for early diagnosis of lung cancer.

The SUV is impacted by many factors, such as blood glucose, partial volume effect, body situation, time after injection, and tumor sizes [24].

Although the size of tumor is also an important aspect for SUV calculation and may even cause false negative results, the relationship between the tumor size and the SUV is difficult to study in clinics. Therefore, a mathematical model and simulated PET images were used to study their relationship. The study may be helpful to the imaging diagnosis of lung cancer, and even to that of small size tumors.

2. Methods

In order to study the relationship between tumor size and SUV, simulated PET images based on the model were used. First, the chest model with different sizes of tumor was established based on visible human project (VHP) data. Then the dynamic metabolic information was simulated with the metabolic model of tissues, including tumor. And then the dynamic PET images were simulated by mapping techniques. Finally, the SUV and SUV_{max} were calculated within the region of interest (ROI) from simulated images. The SUV values from different chest models were compared in term of the sizes of tumor.

2.1. Chest model

The chest model was established based on the VHP datasets. VHP provides detailed anatomical information of the human body and it has been widely used in medical imaging segmentation, reconstruction and 3D visualization [25]. The chest model showed in Figure 1 simplifies the chest of the human body through treating some tissues as air, such as fat and the bone of the chest. Lung tumors with eight different sizes were placed in one side of the lung. Each size was tested individually. The chest models using different sizes of tumor are the foundation of the following study.

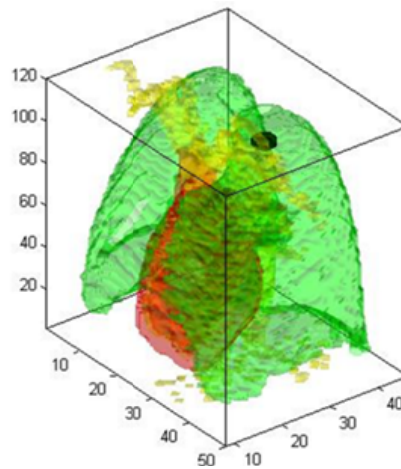


Fig. 1. Schematic diagram of the three-dimensional model.

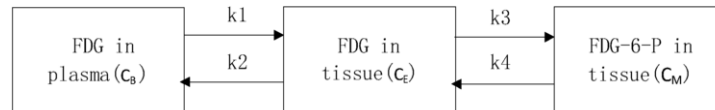


Fig. 2. Three-compartment model.

2.2. Dynamic metabolic information

The simulation of the dynamic metabolic information was based on the existed three-compartment model with a 288.566 MBq injected dose every kilogram. The three-compartment model, used in Hang's study of measuring the metabolism ratio of glucose in local brain tissues in 1980 [26], is the most commonly used in the study of FDG-PET ($[^{18}\text{F}]$ 2-fluoro-2-deoxy-D-glucose, FDG) [27]. Figure 2 shows the structure of the three-compartment model with four parameters.

In the model, three compartments with different concentrations simplify the metabolism system of the human body. C_B is the concentration of FDG in blood. C_E is the concentration of FDG in tissues. C_M is the concentration of the phosphorylated FDG-6-P when it came into the cells. The kinetic parameters of the model, k_1 - k_4 , express the rate coefficient of the substance exchange in different compartments. The curve, which represents the metabolism of blood changing over time, is called the blood time activity curve (BTAC). As BTAC is the input of this model, it is also called an input curve. The BTAC used in this study is the standard input curve from Feng's article [28]. According to the requirement of the experiment, the sampling protocol is set up as follows: 1 min *8, 5 min *9. The time points are 1min, 2min, 10min, 20min, 30min, 40min, 50min. Table 1 shows the kinetic parameters of different normal tissues (myocardium, lung) which are quoted from Cui's articles [29]. Those of skeletal muscle are quoted from Reinhardt's article [30]. The parameters of the simulated lung tumor are quoted from Torizuka's article on lung tumors [31]. In Table 1, f represents the impact coefficient of surrounding tissues that are affected by the radioactive specific activity of blood [32]. C_T is defined to represent the output curve, which is also called the tissue time activity curve.

Table 1
Metabolic model parameters of different organs

tissue name	Model parameters of three-compartment model				
	K1 (ml/min/ml)	K2 (min-1)	K3 (min-1)	K4 (min-1)	f
myocardium	0.196	1.022	0.149	0.010	0.545
lung	0.014	0.291	0.006	0.	0.151
lung tumor	0.231	1.149	0.259	0	0
Skeletal muscle	0.047	0.325	0.084	0	0.019

2.3. Simulated PET images

TTACs of tissues contain function information of tissues metabolism. VHP provides the detailed anatomical information of the human body. The simulation of PET images combines function information with the anatomical information of the human body. Therefore, the PET images were simulated by using TTACs and VHP.

The method that combines TTACs and VHP data sets is the mapping technique proposed by Cui [33]. Firstly, radioactivity values of tissues at specific time points were extracted by sampling the simulated TTACs. Secondly, these radioactivity values were assigned to the corresponding tissues of the VHP datasets at every time point.

The different sizes of the lung tumors in the simulation are set to 0.5 mm³, 1 mm³, 2 mm³, 3 mm³, 5 mm³, 1 cm³, 2 cm³, and 3 cm³. The resolution of VHP datasets is 0.33 mm*0.33 mm*1 mm. According to the resolution, the number of lung tumor pixels was calculated. Clinical PET images are commonly datasets with 128*128 pixels in every cross section. However, every layer of VHP datasets has 1760*1024 pixels. In order to keep the proportion of tissues and simulate the partial volume effect, the sample of simulated datasets was dropped by using an average. After dropping the sample of datasets, the final number of pixels in every cross section is 220*128. Then the chest models with tumor and dynamic metabolic information were obtained.

2.4. Calculation of SUV

SUV (Eq. (1)) represents the ratio of FDG concentration in tissue activity to the injected dose in every kilogram body weight. The SUV is calculated as:

$$SUV = \frac{\text{tissue activity (KBq/ml)}}{\text{injected dose (MBq)/bodyweight (kg)}} \quad (1)$$

SUV_{max} is calculated by using the maximum value of tissue activity instead of the average value of tissue activity. The denominator of the Eq. (1) was estimated as 288.566 MBq/kg, according to a report of Stefani et al. [19]. Tissue activity was obtained by selecting ROI manually from the established chest model. Finally, values of SUV and SUV_{max} were calculated by these values and equation.

3. Results

3.1. Dynamic PET image simulations

The concentration of FDG in each tissue could be described by TTACs, which were simulated with three-compartment model. The simulated TTACs of myocardium, lung, lung tumor, and skeletal muscle, as well as the standard input curve, are shown in Figure 3. The TTACs show the characters of the metabolism in these four tissues. The difference in metabolism could be used as the basis for the dynamic images segmentation.

Dynamic PET images were simulated by mapping with simulated TTACs. Eight sets of dynamic images were simulated. Various tumor size (from 0.5 mm^3 to 3 cm^3) were included in these eight simulated dynamic images. The dynamic imaging sequences consisted of eight 1-min frames, and nine 5-min frames, totaling 17 frames. Some of the simulated images are shown in Figure 4.

3.2. The analysis of the simulated dynamic images

The region of interest, including tumor, were identified on the simulated dynamic images. On this basis, SUV and SUV_{\max} of the lung tumors were calculated according to Eq. (1). Figures 5 and 6 show SUV and SUV_{\max} , separately.

Both SUV and SUV_{\max} change along with the time going. In the clinical study, values at 50 min are the most common used in the diagnosis of tumor. There are differences between changes in SUV and

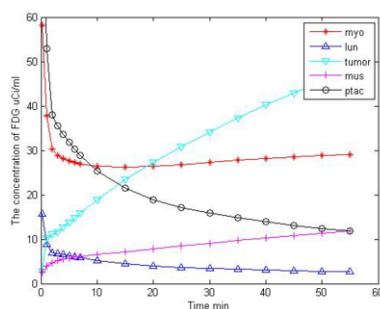


Fig. 3. Simulated TTACs.

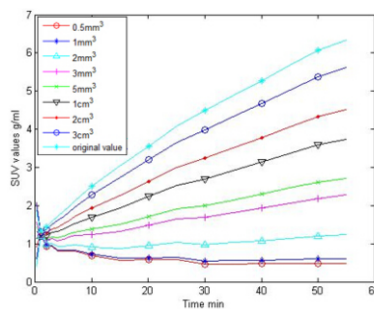


Fig. 5. Comparison between original values and SUV values.

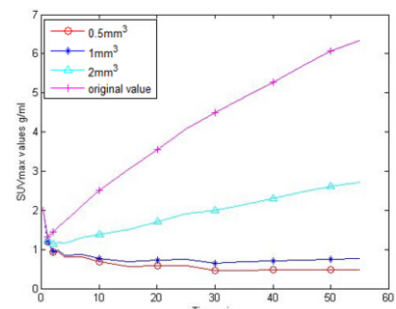


Fig. 6. Comparison of SUV_{\max} with different sizes tumors.

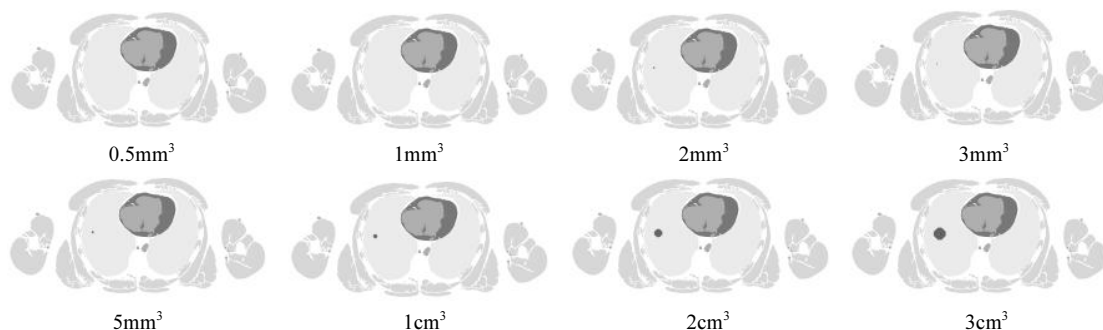


Fig. 4. Simulated PET images.

SUV_{max} . SUV values of different tumor size are less than the original values. SUV values decrease along with the decreasing tumor size. SUV_{max} of some tumor sizes are equal to the original value and some are less than the original value.

4. Discussion

SUV and SUV_{max} were studied based on simulated dynamic PET images. It has been certified that SUV_{max} is preferred to SUV in tumor diagnosis, as Alessandro et al. [21] reported. The SUV will be affected by the size of the tumor. The effect of tumor sizes was studied by simulating PET images with different sizes tumors. Results of the study show that SUV values change with ongoing monitoring time. 50 min is the common used time point in the related studies. Because the difference in the tissues is obvious, radioactive concentration of normal tissues tend to be stable at 50 min. However, FDG uptake in the tumor increased over time. SUV can reflect that distribution of the radioactive tracer. Therefore, SUV values at 50 min were selected to analyze the effect of tumor sizes quantitatively.

Compared with the existing studies, this study focused on the effect of tumor size on diagnosis by using simulated dynamic PET images. Figures 5 and 6 show the relationship between SUV, SUV_{max} and different tumor sizes, respectively. Figure 5 shows that SUV values increase as time increases. In the simulation study, the SUV values of tumor were lower than the original values for the reason of partial volume effect. SUV values reduce along with the tumor size decreased. In the reference, $SUV=2.5$ is generally used as a threshold to differentiate benign and malignant lesions. In Figure 5, tumor with sizes $< 5 \text{ mm}^3$ have SUV values less than 2.5. In other words, the tumor whose size less than 5 mm^3 cannot be diagnosed as malignant tumor. Diagnosis of tumor with sizes $< 5 \text{ mm}^3$ may cause false negative results in the identification of benign and malignant lesions and may result in an inappropriate treatment. SUV_{max} values of normal lung range from 1.0 to 1.5, which are used as a threshold to differentiate the normal lung tumor from lung tissue. As can be seen in Figure 6, SUV_{max} values of the tumor with sizes $> 2 \text{ mm}^3$ are equal to original SUV_{max} of tumor. Tumors with sizes $< 2 \text{ mm}^3$ have SUV values less than 1.5. In other words, the tumor whose sizes less than 2 mm^3 cannot be diagnosed as the tumor. Such results may cause false negative result in the diagnosis of a tumor. The thresholds of study can provide a significant reference for the clinical diagnosis and treatment.

In the clinical study, PET images are affected by noises which were not added in the simulation study. In addition, ROIs were selected manually which caused an error inevitably. These two factors affect the SUV to a certain extent. In a future study, these factors will be studied by adding in the simulated PET images.

5. Conclusion

Though SUV is the useful index for tumor diagnosis in PET imaging, it has some limitations. Through the simulation study, tumor size affects the SUV. Tumors whose size is less than 2 mm^3 have a SUV_{max} value of less than 1.5, which lead to a false negative diagnosis of tumor. Tumors, whose size is less than 5 mm^3 have a SUV value less than 2.5, which affect the grade of the tumor. Compared with SUV, SUV_{max} is better than SUV in the aspect of minimizing the partial volume effect. When tumor size is less than 2 mm^3 , the tumor cannot be diagnosed and evaluated correctly by either SUV or SUV_{max} .

Acknowledgement

This work was supported by National Nature Science Foundation of China (Grant No. 81101123, No. 61108084, No. 61201313, No. 61190125), National Key Technology R & D Program (Grant No. 2012BAI14B04) and the Fundamental Research Funds for the Central Universities of China.

References

- [1] M.P. Pavlou and E.P. Diamandis, The cancer cell secretome: A good source for discovering biomarkers, *Journal of Proteomics* **73** (2010), 1896–1906.
- [2] W. Cho, Contribution of oncoproteomics to cancer biomarker discovery, *Mol. Cancer* **6** (2007), 25–27.
- [3] W. Chen et al., An analysis of lung cancer mortality in China, 2004–2005, *Journal of Preventive Medicine* **44** (2010), 378–382.
- [4] J. She et al., Lung Cancer in China Challenges and Interventions, *Chest* **143** (2013), 1117–1126.
- [5] H.S. Sekhon et al., Advances in cytopathology for lung cancer: The impact and challenges of new technologies, *Thoracic Surgery Clinics* **23** (2013), 163–178.
- [6] A. Jemal et al., Global cancer statistics, *CA: A Cancer Journal for Clinicians* **61** (2011), 69–90.
- [7] W.C.S. Cho, Molecular diagnostics for monitoring and predicting therapeutic effect in cancer, *Expert Review of Molecular Diagnostics* **11** (2011), 9–12.
- [8] M. Hassanein et al., Advances in proteomic strategies toward the early detection of lung cancer, *Proceedings of the American Thoracic Society* **8** (2011), 183–188.
- [9] Y. Liu and M. Wang, Advances in early diagnosis of lung cancer, *Journal of Lung Cancer* **14** (2011), 429–434.
- [10] L. Cui and H. Wei, Research status and funding trends of lung cancer biomarkers, *Journal of Thoracic Disease* **5** (2013), 698–705.
- [11] Z. Altintas and I. Tothill, Biomarkers and biosensors for the early diagnosis of lung cancer, *Sensors and Actuators B-Chemical* **188** (2013), 988–998.
- [12] C.H. Oak et al., Potential molecular approaches for the early diagnosis of lung cancer (Review), *Molecular Medicine Reports* **6** (2012), 931–936.
- [13] S. Thureau et al., Interobserver Agreement of qualitative analysis and tumor delineation of f-18-fluoromisonidazole and 3'-deoxy-3'-f-18-fluorothymidine PET images in lung cancer, *Journal of Nuclear Medicine* **54** (2013), 1543–1550.
- [14] N. Avril et al., Response to therapy in breast cancer, *Journal of Nuclear Medicine* **50** (2009), 55–63.
- [15] L. Schrevels et al., The role of PET scan in diagnosis, staging, and management of non-small cell lung cancer, *Oncologist* **9** (2004), 633–643.
- [16] G. Mehta et al., Feasibility study of FDG PET/CT-derived primary tumor glycolysis as a prognostic indicator of survival in patients with non-small-cell lung cancer, *Clinical Radiology* **69** (2014), 268–274.
- [17] O. Demirkaya, Lesion segmentation in whole-body images of PET, *Nuclear Science Symposium Conference Record* **4** (2003), 2873–2876.
- [18] K.R. Zasadny and R.L. Wahl, Standardized uptake values of normal tissues at PET with 2-fluorine-18-fluoro-2-deoxy-D-glucose: Variations with body weight and a method for correction, *Radiology* **189** (1993), 847–850.
- [19] C. Juhasz et al., Quantification of tryptophan transport and metabolism in lung tumors using PET, *Journal of Nuclear Medicine* **50** (2009), 356–363.
- [20] Y. Koh et al., EGFR gene copy number gain is related to high tumor SUV and frequent relapse after adjuvant chemotherapy in resected lung adenocarcinoma, *Journal of Clinical Oncology* **41** (2011), 548–554.
- [21] A. Stefani et al., Integrated FDG-PET/CT imaging is useful in the approach to carcinoid tumors of the lung, *Journal of Cardiothoracic Surgery* **8** (2013), 1–7.
- [22] B. Mi et al., The value of extra-lung lesions on 18 F-FDG PET/CT in improving diagnosis of lung cancer, *Chinese Journal of Lung Cancer* **15** (2012), 78–83.
- [23] C.D. Ramos et al., FDG-PET standardized uptake values in normal anatomical structures using iterative reconstruction segmented attenuation correction and filtered back-projection, *Journal of Nuclear Medicine* **28** (2001), 155–164.
- [24] P. Obara and Y. Pu, Prognostic value of metabolic tumor burden in lung cancer, *Chinese Journal of Cancer Research*, **25** (2013), 615–622.
- [25] A. Pommert et al., Creating a high-resolution spatial/symbolic model of the inner organs based on the visible human, *Medical Image Analysis* **5** (2001), 221–228.

- [26] S.C. Huang et al., Noninvasive determination of local cerebral metabolic rate of glucose in man, *The American Journal of Physiology* **238** (1980), 69–82.
- [27] Y.T. Hong and T.D. Fryer, Kinetic modelling using basis functions derived from two-tissue compartmental models with a plasma input function, *Neuroimage* **51** (2010), 164–172.
- [28] D. Feng et al., A technique for extracting physiological parameters and the required input function simultaneously from PET image measurements: theory and simulation study, *IEEE Transactions on Information Technology in Biomedicine: A Publication of the IEEE Engineering in Medicine and Biology Society* **1** (1997), 243–254.
- [29] Y. Cui et al., Parameter estimation for whole-body kinetic model of FDG metabolism, *Progress in Natural Science* **16** (2006), 1164–1170.
- [30] M. Reinhardt et al., Quantification of glucose transport and phosphorylation in human skeletal muscle using FDG PET, *Journal of Nuclear Medicine* **40** (1999), 977–985.
- [31] T. Torizuka et al., Untreated primary lung and breast cancers: correlation between F-18 FDG kinetic rate constants and findings of in vitro studies, *Radiology* **207** (1998), 767–774.
- [32] X. Li et al., Estimation of myocardial glucose utilisation with PET using the left ventricular time-activity curve as a non-invasive input function, *Medical and Biological Engineering and Computing* **36** (1998), 112–117.
- [33] Y.F. Cui and J. Bai, Method of simulation and visualization of FDG metabolism based on VHP image, *Medical Imaging 2005: Visualization, Image-Guided Procedures, and Display, Pts. 1 and 2* **5744** (2005), 547–554.

Modeling the excretion of FDG in human kidneys using dynamic PET

Huiting Qiao^{a,b}, Jing Bai^{a,*}, Yingmao Chen^c, Jiahe Tian^c

^aDepartment of Biomedical Engineering, School of Medicine, Tsinghua University, Beijing, PR China

^bSchool of Biological Science and Medical Engineering, Beijing University of Aeronautics and Astronautics, Beijing, PR China

^cDepartment of Nuclear Medicine, General Hospital of PLA, Beijing, PR China

Received 29 October 2007; accepted 16 September 2008

Abstract

In order to understand the excretion function of kidneys, dynamic scan was performed using the positron emission tomography (PET), the process of FDG's (2-[¹⁸F]fluoro-2-deoxy-D-glucose) excretion was detected, and the kidney model was established. The model in this study consisted of two parts: the fore part of the model described the transportation of FDG from plasma and the accumulation of FDG in kidney, and the latter part of the model described the transportation of FDG from kidney to ureter and then to bladder. Since there was a time delay between the fore part and the later part, which occurred when FDG was filtered into urine and accumulated in pelvis temporarily, a new parameter, delay constant t_0 , was introduced in the model. Twelve healthy adult volunteers took part in the dynamic FDG-PET experiment. Ten subjects received dynamic scan on kidneys, and the data extracted from the PET scans were used for parameter estimation and model analysis. The other two subjects received dynamic scan on bladder in order to confirm the time delay constant. The output of the model fit well with the original curve, and the model built in this study could not only describe the excretion process of FDG, but also be used to quantitatively estimate urinary excretion of FDG and plasma clearance. Moreover, the model kept good accordance with physiological characteristics. © 2008 Elsevier Ltd. All rights reserved.

Keywords: Kidney; Model; FDG; PET; Dynamic scan; Excretion

1. Introduction

The use of positron emission tomography (PET) has made it possible to detect the physiological process in human bodies. The 2-[¹⁸F]fluoro-2-deoxy-d-glucose (FDG) is one of the analogues of glucose, which has been widely used in clinical PET study and diagnoses [1]. Using FDG-PET, the dynamic physiological process can be detected *in vivo*. Mathematical models of FDG have been established for brain, heart, liver and some other organs [2–5] but little work has been done for kidney modeling using FDG-PET. The main reason is that FDG cannot be reabsorbed at renal tubule, and high quantity of FDG is excreted through kidney [6]. Nevertheless, this character makes FDG adapt to detection of the excretion function of kidneys.

In some studies, the function of kidney is just described by a constant rate from plasma to urine [7]. For some tracers,

kidney can also be described by the classical three-compartment model [8]. Shreve et al. [9] have used ¹¹C-acetate as the tracer to detect kidney. In their study no urinary tracer activity appeared in the intrarenal collecting system. Unlike monoamine oxidase B and ¹¹C-acetate, FDG is a kind of tracer which cannot be reabsorbed when the initial urine passes through the renal tubule. Therefore, FDG can be detected in renal pelvis (Fig. 1) and bladder.

In previous work, we have compared the bidirectional fluxes with the unidirectional fluxes of FDG between blood and kidneys. Although bidirectional fluxes model could give a smaller weighted residual sum of squares (WRSS), the unidirectional fluxes model was more preferable according to Akaike information criteria (AIC) [10] and Schwarz criteria (SC) [11], thus the unidirectional fluxes was also used in this model. The unidirectional fluxes from kidney to metabolism and to urine have appeared in some pharmacokinetic models [12]. Compared with excretion of FDG, the quantity of FDG metabolized in kidney is very small. Thus renal metabolism of FDG was neglected in this model. Because double peaks could be obviously detected

* Corresponding author. Tel.: +86 10 62786480.

E-mail address: deabj@tsinghua.edu.cn (J. Bai).

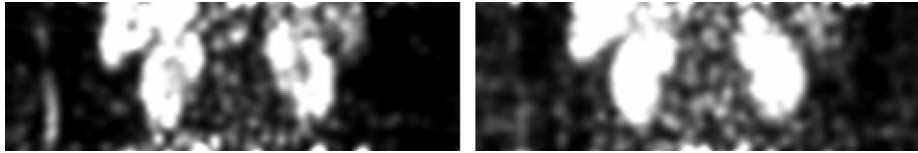


Fig. 1. The kidney images in FDG-PET. On the left is a coronal section of one subject in this study at 3 min after injection, and on the right is the same coronal section of the same subject at 10 min after injection.

in most time-activity curve (TAC) of kidneys, the time delay constant was involved in this model, which could give a good explanation to double-peak phenomenon. The model consists of two parts: the process of FDG's transport from blood and the process of FDG's excretion out of kidneys, and the time delay occurred between these two parts.

Using the model presented in this paper, the excretion process can be simulated, and the excretion of FDG and plasma clearance can be quantitatively estimated in the whole process.

2. Materials and methods

2.1. Subjects

Twelve normal volunteers participated in the study. Ten volunteers formed a group for kidney modeling study, with age between 34 and 60 years (mean \pm SD, 47 ± 9 years), height from 165 to 185 cm (171 ± 6 cm), and weight from 53 to 94 kg (74 ± 11 kg). The other two volunteers took part in the experiment to validate the time delay. None of them had a prior history of any major metabolic illnesses or renal diseases. Dynamic FDG-PET scans were performed on each subject. They were asked to fast for at least four hours, and to empty the bladder before the scanning. During the experiment, they were asked to lie down still and to keep quiet. Each volunteer was informed fully about the purposes and procedures of the study and had given written consent before the experiment was undertaken.

2.2. PET scanning protocol

All the experiments were carried out with an ECAT-EXACT HR⁺ PET scanner (CTI/Siemens, Inc., TN, USA), with a 15.5 cm field of view, 63 transaxial image planes and 4.2 mm full-width-at-half-maximum spatial resolution in the centre field of view. Each voxel was $5.15 \times 5.15 \times 2.43$ mm³. For modeling study, the experiments were performed in a single bed position covering the kidneys. The tracer dose of FDG, 2.6–5 mCi was injected intravenously into the human body, and PET scan began immediately after the injection. In the sampling protocol, the dynamic imaging sequences consisted of six 10-s frames, eight 20-s frames, six 30-s frames, five 60-s frames, four 300-s frames, and three 600-s frames, totaling 32 frames for a total scan time of 61 min and 40 s. To validate the time delay constant, the other two volunteers took a dynamic scan on bladder, with a protocol of 20×30 -s frames.

2.3. Data acquisition

Kidney and abdominal aorta could be detected from the renal dynamic PET image. The region of interest (ROI) was manually drawn on 3-D images. The TAC was picked up from ROI in each frame. The radioactivity was calculated by averaging the whole voxel's values within the ROI. The time-activity curve of blood (BTAC) was derived from the ROI in abdominal aorta [13,14], which was drawn in the frame about 10–30 s after injection. The tissue time-activity curve (TTAC) of kidney was derived from ROI of the whole kidney region. The number of voxel of the renal ROI was used to calculate the volume of the kidney.

2.4. Model description

The new kidney model consisted of two parts: one part described the transportation of FDG from blood and the other part described the excretion process of FDG out of kidney. t_0 , the timing delay constant, was the excretion time of FDG out of kidney from injection. In this model, it was assumed that concentrations of FDG were homogeneous in compartments of blood and kidney. Compared with large quantity of FDG flowing through kidneys, the metabolism of FDG in kidney was unobvious, thus it was neglected in the model. K_1 was the rate constant of FDG from blood compartment to kidney compartment, and k_2 was that from kidney to bladder. When $t < t_0$, no FDG flowed out of kidneys. FDG diffused in blood, went into the kidney from circulation system, filtrated to urine, and accumulated in renal pelvis temporarily.

$$C_2(t) = K_1 \int_0^t C_1(t) \quad t < t_0 \quad (1)$$

where $C_1(t)$ is the concentration of FDG in blood, $C_2(t)$ is the concentration of FDG in kidneys. When $t \geq t_0$, it began to excrete FDG with urine out of kidneys.

$$\frac{dC_2(t)}{dt} = K_1 C_1(t) - k_2 C_2(t) \quad t \geq t_0 \quad (2)$$

Eq. (3) was derived from Eqs. (1) and (2) by Laplace transform. \otimes denotes the operation of convolution.

$$\begin{cases} C_2(t) = K_1 \int_0^t C_1(t) & t < t_0 \\ C_2(t) = K_1 e^{-k_2(t-t_0)} \otimes C_1(t) + C_2(t_0) e^{-k_2(t-t_0)} & t \geq t_0 \end{cases} \quad (3)$$

$$C_T(t) = C_2(t) + f C_1(t) \quad (4)$$

$C_T(t)$ is the concentration of FDG in kidney, which can be detected by PET. Since kidney is an organ rich in blood, the

parameter f was used to describe the effect fraction from the blood to kidney. $C_1(t)$ and $C_T(t)$, are the input and output of the model to estimate the parameter by nonlinear curve fitting.

2.5. Urinary excretion of FDG and plasma clearance

Using the model, the urinary excretion of FDG from kidney, $X_3(t)$, can be estimated. The quantity of FDG in kidney, $X_2(t)$, can be calculated with the concentration of FDG in kidney and the estimated volume of kidney [15], as shown in Eq. (5). The FDG in urinary came totally from renal excretion, thus the urinary excretion of FDG can be described with the rate constants k_2 mentioned before as shown in Eq. (7).

$$X_2(t) = C_2(t)V_2 \quad (5)$$

$$\frac{dX_3(t)}{dt} = X_2(t) \cdot k_2 = C_2(t)V_2 \cdot k_2 \quad (6)$$

$$X_3(t) = \int_0^t \frac{dX_3(t)}{dt} dt = \int_0^t C_2(t)V_2 k_2 dt \quad (7)$$

With quantificational estimated urinary excretion of FDG, the plasma clearance, K_{CL} , can be estimated dynamically. Plasma clearance is an important parameter to characterize the capability of kidneys to clear something from plasma.

$$C_1(t) \cdot K_{CL} = \frac{dX_3(t)}{dt} \quad (8)$$

3. Results

This model was built and implemented using an IBM personal computer with Windows XP. A number of functions and tools in Matlab 6.5 software package, including nonlinear least-squares fitting (lsqnonlin) and curve fitting tool (cftool), were also applied to help implement and analyze the model.

3.1. Parameters of model fit

Ten dynamic data sets from the ten subjects were used for parameter estimation. The BTAC picked up from aorta was the input of the model, while the detected TTAC of kidney was the output of the model. The weighted nonlinear least-squares algorithm was applied to estimate all of the parameters provided that t_0 was one time point around the second peak of TTAC. The weights were the inverses of the measurement error. Parameters for the model were listed in Table 1. R -square presents the coefficient which measures how successful the fit is. A value closer to 1 indicates a better fit. Fig. 2 presented the data and its fit to the model in one of the subjects.

3.2. Confirmation of delay constant t_0

Two volunteers took dynamic scan on bladder to validate whether the delay constant t_0 is reasonable. The time delay occurred when FDG was filtered into urine and accumulated in pelvis temporarily. Thus it took at least t_0 for FDG to appear in bladder after injection. Fig. 3 showed the TTAC of one bladder.

Table 1

Estimated parameters of the kidney model and the R -square of the fitting.

	K_1 (1/min)	k_2 (1/min)	f	t_0 (min)	R -square
Subject 1	0.2915	0.3828	0.8403	4.267	0.9573
Subject 2	0.3311	0.3693	0.4276	2.633	0.9390
Subject 3	0.2799	0.2956	0.5244	3.667	0.8448
Subject 4	0.2251	0.2657	0.3495	3.75	0.8625
Subject 5	0.3712	0.2947	0.3074	3.333	0.9339
Subject 6	0.2169	0.2149	0.4564	5	0.9136
Subject 7	0.3012	0.3038	0.4333	3.333	0.9675
Subject 8	0.21208	0.34812	0.35043	3.167	0.9640
Subject 9	0.15083	0.18361	0.35499	4.5	0.9547
Subject 10	0.254	0.33445	0.33478	2.667	0.9385
Mean	0.2634	0.2993	0.4379	3.6317	0.9276
SD	0.0647	0.0643	0.1563	0.7722	0.0423

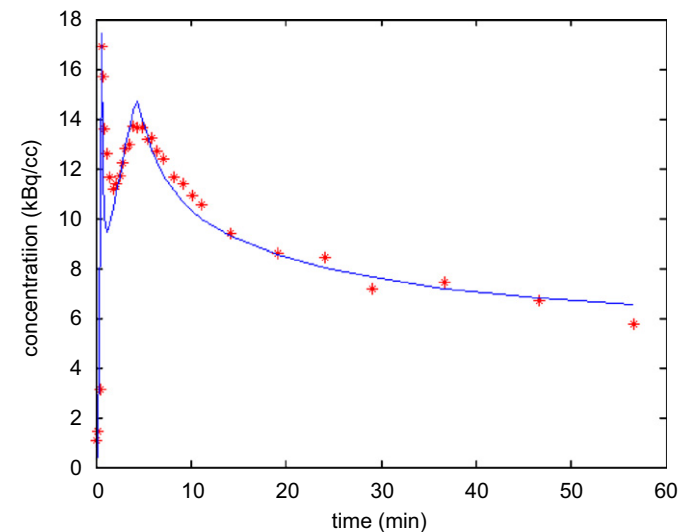


Fig. 2. Time-activity curves of kidney. The asterisks show the TTAC extracted from PET kidney scan of one subject and the normal line represents its fit curve by this model.

It was about 3 min after injection that the accumulation of FDG in bladder became visible. The obvious FDG excretion step appeared at about 3–5 min after injection in these two dynamic experiments. That was consistent with the estimation of t_0 .

3.3. Urinary excretion of FDG

The volume of kidneys was estimated by the voxel number in ROI. The estimated volume of kidney was listed in Table 2, accorded with the volume of each kidney reported by Deloar [16] and Bouchet [17]. The estimated urinary excretion of FDG in about 60 min for each subject was listed in Table 2. The urinary excretion of FDG was between 10%ID and 20%ID, with a mean of 14.29%ID, which was a little higher than the excretion of FDG in urine 8.21%ID for dehydrated patient and 6.67%ID for hydrated patient [18] and about 10%ID estimated by Hays' model [7]. The accumulation of FDG can also be

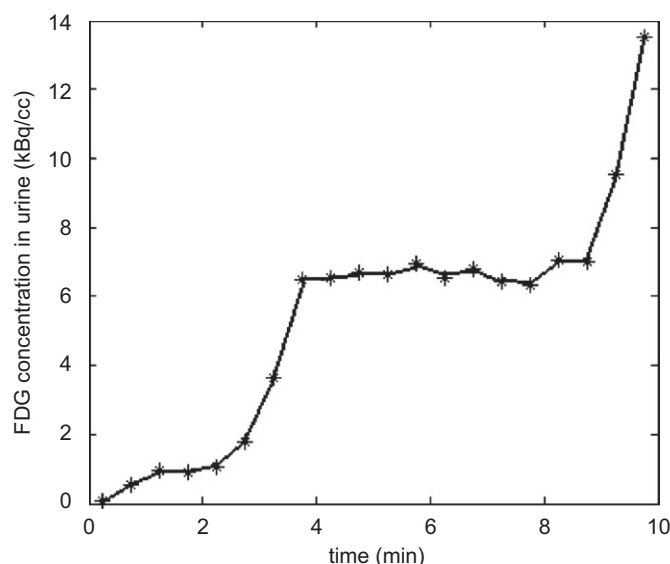


Fig. 3. Time-activity curve of urine in bladder.

Table 2

Urinary excretion (%ID) of FDG and accumulation (%ID) of FDG in kidneys (60 min after injection).

	Voxel	Volume (cm ³)	Input (mCi)	FDG in urine (%ID)	FDG in kidney (%ID)
Subject 1	4277	275.6	4	15.15	0.58
Subject 2	4506	290.4	5	13.59	0.55
Subject 3	4200	270.7	4	18.08	0.88
Subject 4	4174	269	4.2	14.62	0.73
Subject 5	3994	257.4	4	18.63	0.88
Subject 6	4161	268.2	4.2	11.39	0.70
Subject 7	4243	273.5	2.6	14.55	0.62
Subject 8	4223	272.2	4.5	15.42	0.58
Subject 9	4284	276.1	4.5	9.243	0.64
Subject 10	3794	244.5	4	12.22	0.44
Mean	4185.6	269.8		14.29	0.66

calculated for each subject, using Eq. (7). The mean value of accumulation of FDG in kidney is 0.66%ID, about an hour after injection.

3.4. Plasma clearance of FDG

The plasma clearance was estimated using Matlab cftool after the system becoming stable. In time period t_0 after injection, no FDG was excreted from kidneys, therefore the data after t_0 were used to estimate plasma clearance. The result of linear regression analysis of urine excretion rate of FDG versus plasma concentration was shown in Fig. 4. The slope of the fitting result is the plasma clearance of FDG. All the plasma clearances estimated for each subject were list in Table 3. The mean plasma clearance of FDG is 115.8 ml/min, a little lower than glomerular filtration rate, 125 ml/min.

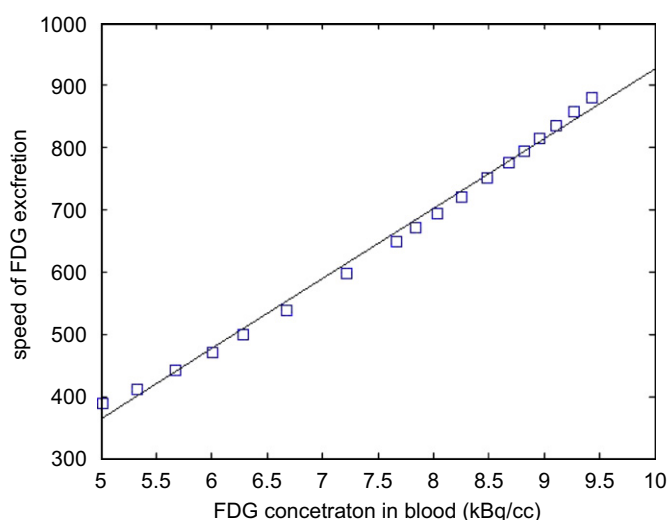


Fig. 4. Curve fitting to estimate the plasma clearance. The square is the point from experiment and model, the solid line is the fitting result.

4. Discussion

Although FDG is not a good tracer for the study of renal metabolism, it is suitable to detect excretive process in kidney. The model developed in this paper could dynamically simulate the process of FDG's excretion, and quantitatively estimate the urinary excretion and plasma clearance of FDG. For great percentage of FDG pass through kidney, the development of the model would benefit the study of FDG-PET.

In previous work, a kidney model of separated renal parenchyma had been developed [19], which was a unidirectional model. The unidirectional model was the optimal choice considering the efficiency and feasibility of the model. However, this model was not considered satisfactory, because it only described part of kidney. As a result, a more advanced model was developed in this study based on the previous work. The time delay constant t_0 was introduced in this model and successfully explained the double-peak time-activity curve. The time delay constant had two significant observations: (1) in the first t_0 after injection, no FDG appeared in urinary out of kidney, and (2) the time for FDG to pass through kidney and to excrete to bladder was approximately equal to t_0 . Thus when $0 < t < t_0$, the model only described the transportation of FDG from plasma and accumulate in kidney. In first t_0 after injection, the FDG in kidney filtered into urine, and after t_0 FDG began to leave kidney and transport into bladder by ureter. Like other kinetic parameters, t_0 is a parameter that differs from each person to another, and could evaluate renal function. Apart from the excretion of FDG, in kidney the quantity of metabolized FDG was insignificant.

Ten sets of clinical dynamic data were used to estimate the parameters. Results have shown some differences for different subject. However, the output of the model fitted with the original curve from clinical data well, which could be seen from R-square value in Table 1. The mean parameter values were calculated in ten subjects to build a typical model. The renal

Table 3
Estimation of plasma clearances.

Subject	1	2	3	4	5	6	7	8	9	10	Mean
K_{CL}	199.7	194.1	112.7	83.21	140.8	90.64	105	96.74	50.21	85.35	115.8
R -square	0.8416	0.9536	0.9944	0.9969	0.9912	0.9978	0.9934	0.986	0.9788	0.9952	

volume was calculated for each subject, and was used to estimate the quantity of FDG in urine at about 60 min. The urinary excretion of FDG estimated was a little higher than those from the literature. The urinary excretion estimated in this paper contained the urine in ureter and in bladder, while others estimated it by measuring FDG in urine voided from bladder. Therefore the result in this study was reasonable.

5. Summary and conclusion

The process of FDG excretion is detected using PET. The model for kidney was developed with mean parameter values K_1 to be $0.2634 \text{ (min}^{-1}\text{)}$, k_2 to be $0.2993 \text{ (min}^{-1}\text{)}$, blood fraction in kidney to be 0.4379, and t_0 to be 3.6317 (min). Though individual differences exist, this model could still give a good fit to dynamic data extracted from clinic experiments. Using this model, the excretive process of FDG could be simulated, and the accumulation of FDG in urine and the plasma clearance could be estimated. The estimated results did not differ significantly from the literature, and the difference could be explained reasonably.

Conflict of interest statement

There is no conflict of interest.

Acknowledgements

We would like to thank Prof. David Feng, Prof. Stefan Eberl and Dr. Lingfeng Wen of School of Information Technologies, the University of Sydney, for their helpful comments and advices. We are also grateful for people who volunteered for this study. This work was partially supported by the National Nature Science Foundation of China, the Tsinghua-Yue-Yuen Medical Science Foundation, the National Basic Research Program of China, the Special Research Fund for the Doctoral Program of Higher Education of China, and International Science Linkages established under the Australian Government's innovation statement (CH050131).

References

- [1] L. Kostakoglu, H. Agress, S.J. Goldsmith, Clinical role of FDG PET in evaluation of cancer patients, *Radiographics* 23 (2003) 315.
- [2] A. Bertoldo, P. Vicini, G. Sambuceti, et al., Evaluation of compartmental and spectral analysis models of [^{18}F]FDG kinetics for heart and brain studies with PET, *IEEE Trans. Biomed. Eng.* 45 (1998) 1429.
- [3] Y.F. Cui, J. Bai, Y.M. Chen, et al., Parameter estimation for whole-body kinetic model of FDG metabolism, *Prog. Nat. Sci.* 16 (2006) 1164.
- [4] S.C. Huang, M.E. Phelps, E.J. Hoffman, et al., Noninvasive determination of local cerebral metabolic rate of glucose in man, *Am. J. Physiol. Endocrinol. Metab.* 238 (1980) E69.
- [5] T. Torizuka, K.R. Zasadny, B. Recker, et al., Untreated primary lung and breast cancers: correlation between F-18 FDG kinetic rate constants and findings of in vitro studies, *Radiology* 207 (1998) 767.
- [6] Z. Szabo, J.S. Xia, W.B. Mathews, et al., Future direction of renal positron emission tomography, *Semin. Nucl. Med.* 36 (2006) 36.
- [7] M.T. Hays, G.M. Segall, A mathematical model for the distribution of fluorodeoxyglucose in humans, *J. Nucl. Med.* 40 (1999) 1358.
- [8] J.S. Fowler, J. Logan, G.J. Wang, et al., PET imaging of monoamine oxidase B in peripheral organs in humans, *J. Nucl. Med.* 43 (2002) 1331.
- [9] P. Shreve, P.C. Chiao, H.D. Humes, et al., Carbon-11-acetate PET imaging in renal-disease, *J. Nucl. Med.* 36 (1995) 1595.
- [10] H. Akaike, A new look at the statistical model identification, *IEEE Trans. Autom. Control* 19 (1974) 716.
- [11] G. Schwarz, Estimating the dimension of a model, *Ann. Stat.* 6 (1978) 461.
- [12] R.R. Brechner, D.Z. D'Argenio, R. Dahalan, et al., Noninvasive estimation of bound and mobile platinum compounds in the kidney using a radiopharmacokinetic model, *J. Pharm. Sci.* 75 (1986) 873.
- [13] G. Germano, B.C. Chen, S.C. Huang, et al., Use of the abdominal aorta for arterial input function determination in hepatic and renal PET studies, *J. Nucl. Med.* 33 (1992) 613.
- [14] S. Keiding, O.L. Munk, K.M. Schiött, et al., Dynamic 2- ^{18}F fluoro-2-deoxy-d-glucose positron emission tomography of liver tumours without blood sampling, *Eur. J. Nucl. Med. Mol. Imaging* 27 (2000) 407.
- [15] D.C. Maneval, D.Z.D. Argenio, W. Wolf, A kinetic model for $^{99\text{m}}\text{Tc}$ -DMSA in rat, *Eur. J. Nucl. Med.* 16 (1990) 29.
- [16] H.M. Deloar, T. Fujiwara, M. Shidahara, et al., Estimation of absorbed dose for 2- ^{18}F fluoro-2-deoxy-d-glucose using whole-body positron emission tomography and magnetic resonance imaging, *Eur. J. Nucl. Med. Mol. Imaging* 25 (1998) 565.
- [17] L.G. Bouchet, W.E. Bolch, H.P. Blanco, et al., MIRD pamphlet No. 19: absorbed fractions and radionuclide s values for six age-dependent multiregion models of the kidney, *J. Nucl. Med.* 44 (2003) 1113.
- [18] J.K. Moran, H.B. Lee, M.D. Blafox, Optimization of urinary FDG excretion during PET imaging, *J. Nucl. Med.* 40 (1999) 1352.
- [19] H. Qiao, J. Bai, Y. Chen, et al., Kidney modelling for FDG excretion with PET, *Int. J. Biomed. Imaging* (2007).

Huiting Qiao was born in China, in 1980. She received the bachelor degree in biomedical engineering from Tianjin University of China in 2003. She obtained her PhD degree in Biomedical engineering of Tsinghua University in China. Now she works in School of Biological Science and Medical Engineering in Beijing University of Aeronautics and Astronautics. Her research interests focus on modeling in biomedical engineering.

Jing Bai obtained her MS and PhD from Drexel University, Philadelphia, in 1983 and 1985. From 1985 to 1987 she was a Research Associate and Assistant Professor with the Biomedical Engineering and Science Institute of Drexel University. In 1991, and 2000 she became a Professor, and Cheung Kong Chair Professor at Biomedical Engineering Department of Tsinghua University, Beijing, China. Her research activities have included mathematical modeling and simulation of cardiovascular system, optimization of cardiac assist devices, medical ultrasound, telemedicine, home health care network and home monitoring devices, infrared imaging and molecular imaging. She has published four books and over 100 journal papers. She is a Fellow of IEEE. From 1997, she became an Associate Editor for IEEE Transactions on Information Technology in Biomedicine.

Yingmao Chen received a degree from the University of Henan, China, in 1982 and a master degree, from Zhongshan Medicine University, in 1992. Now he is an Associate Professor in the Department of Nuclear Medicine, General Hospital of PLA, in China. His research interests focus on nuclear medicine.

Jiahe Tian was graduated from Medicine University of Jilin, in China. He has been a visiting scholar in University of New South Wales, in Australia. Now he is the Professor in the Department of Nuclear Medicine, General Hospital of PLA, in China. His research interests focus on nuclear medicine.

Review Article

The Transport and Deposition of Nanoparticles in Respiratory System by Inhalation

Huiting Qiao,^{1,2} Wenyong Liu,¹ Hongyu Gu,¹ Daifa Wang,¹ and Yu Wang¹

¹Key Laboratory for Biomechanics and Mechanobiology of Ministry of Education, School of Biological Science and Medical Engineering, Beihang University, Beijing 100191, China

²School of Biomedical Engineering, Science and Health Systems, Drexel University, Philadelphia, PA 19104, USA

Correspondence should be addressed to Yu Wang; wangyu@buaa.edu.cn

Received 18 September 2014; Accepted 25 December 2014

Academic Editor: Shuming Zhang

Copyright © 2015 Huiting Qiao et al. This is an open access article distributed under the Creative Commons Attribution License, which permits unrestricted use, distribution, and reproduction in any medium, provided the original work is properly cited.

The inhaled nanoparticles have attracted more and more attention, since they are more easily to enter the deep part of respiratory system. Some nanoparticles were reported to cause pulmonary inflammation. The toxicity of nanoparticles depends not only on its chemical component but also on the quantity and position of the deposition. The deposition of nanoparticles is not uniform and is influenced by airflow transport. The high deposition mainly occurs at the carinal ridges and the inside walls around the carinal ridges. Many factors could affect the transport and deposition of nanoparticles, such as particle size, flow rate, structure of airway, pulmonary function, and age. In this review, we discussed the methods and technique involved in particle transport and deposition studies. The features of particles deposition could be observed in clinic experiments and animal experiments. The mechanism of transport could be studied by numerical simulation. Numerical model and experiment study supplement each other. Some techniques such as medical imaging may support the study of nanoparticles transport and deposition. The knowledge of particles transport and deposition may be helpful both to defend the toxicity of inhaled particles and to direct inhaled drug delivery.

1. Introduction

More and more attention has been paid to air pollution. The high concentration of fine particle matter (PM 2.5) during the 2013 severe haze of north China has caused public worries [1, 2]. The most worries are due to the adverse effect of air pollution on health [3]. It is believed that the most airborne particles were derived from fossil, biomass, and solid fuels combustion [4–6]. The traffic exhausts have been verified as the source of particle matter [7, 8]. The particles emitted by engines have a high proportion of nanoparticles, though most of them are in accumulation mode [9]. Epidemiological studies have confirmed that air pollution makes adverse health effect, especially the pollutant in nanoscale [10, 11]. Thus, nowadays most attention paid to airborne pollutants lies in nanoparticles and ultrafine particles.

Though some studies did not differentiate ultrafine particles from nanoparticles [12], the different definitions have also been reported. The particles in nanoscales (<100 nm) in

one dimension could be generally called nanoparticles, while ultrafine particles are limited to 100 nm in all dimensions [13]. For the purposes of this review, we do not differentiate nanoparticles from ultrafine particles: they are both particles in nanoscales.

People have great expectation for nanotechnology and have been trying to apply nanomaterial in many fields [14, 15]. Thus airborne nanoparticles are unavoidable. For the reason of small size, nanoparticles may enter the deep part of human respiratory system with breathing. Pulmonary inflammation has been reported after inhalation exposure to nanoparticles [16, 17], so the toxicity of nanoparticles in air should be considered [18].

Respiratory system is an important pathway for substance to enter human body besides alimentary canal. Air enters the trachea through nasal and oral cavities, passing by the tracheobronchial tree, and arrives at the alveoli, so does some airborne nanoparticles. The transport and deposition of particles have great relations with the complicated airway.

The structures of respiratory system have been described by Weibel as a bifurcating tubes' model with 23-generation bifurcations, and the airways are named as G0–G23 [19, 20]. The airways from G0 to G16 belong to conducting zone, and the airways from G17 to G23 have the function of gas exchange. The upper airway, which begins from the nose and mouth to the trachea (G0), functions not only as the passage-way but also as a filter to protect the lower airway; however some small-scale pollutants could still enter the respiratory system and may cause disease [21–23].

Although many researches have confirmed that the toxicity of airborne particles changes along with their compositions [24], the quantity of transport and the position of deposition also have great relations with the toxicity of nanoparticles. This review aims at the toxicity of nanoparticles by inhalation with great emphasis on the transport and deposition of nanoparticles in respiratory system. The research methods for toxicity of airborne nanoparticles were compared. The potential application of a medical imaging technique was also mentioned.

2. The Toxicity of Nanoparticles by Inhalation

Airborne particles especially nanoparticles have been recognized as a potential risk for health. Since airborne nanoparticles enter human body by inhalation, respiratory system has higher risk exposed to nanoparticles [25]. In the view of epidemiology, the increased morbidity and mortality may have relations with particles in air [23, 26]; for example, fine particulate pollution is confirmed to be associated with all-cause, lung cancer and cardiopulmonary mortality [27]. For their small scale, nanoparticles can enter lower airway, reach alveoli, and can even pass the alveolar epithelium to intrapleural space [28]. Pulmonary inflammation could be caused when exposed to some nanoparticles [17].

Nanoparticles harm respiratory system mainly by the injury of epithelium [29], and the most important mechanism is the oxidative stress induced by nanoparticles [30, 31]. The adverse effects happen not only in respiratory system but also in extrapulmonary organs. Once nanoparticles reach pulmonary alveoli, some of them may pass through the alveolar epithelium and capillary endothelial cell and then enter the cardiovascular system and other internal organs [32]. In the long term exposure experiment using sensitive mouse model, inhaled nickel hydroxide could increase mitochondrial DNA damage in the aorta and exacerbate the progression of atherosclerosis as well as the inflammation in lung [30]. The pathological changes in liver have also been reported when inhalation exposed to ferric oxide and zinc oxide nanoparticles [33].

The toxicity of airborne nanoparticles depends on the chemical component of the nanomaterial. To confirm the toxicity of individual nanoparticles, the effect on health of nanoparticles has been studied, respectively. Some nanoparticles may cause pulmonary inflammation, while some nanoparticles may not. A great deal of metallic oxide and hydroxide may cause pulmonary inflammation. Nanoparticles of zinc oxide [34, 35], aluminum oxide [36], copper oxide [37, 38], cobalt oxide [37], iron oxide [39], cadmium oxide [40], and

nickel hydroxide [30, 41] have been reported to induce pulmonary inflammation and adverse effects, while no significant inflammation nor adverse effects have been observed when exposed to some nanomaterials, such as carbon nanoparticles [41], graphite nano platelets [42], carbon black [42], and silica [43].

The toxicity of nanoparticles depends not only on the chemical component, but also on dose, size, and other factors [13, 17]. For the nanoparticles of the same component, size and concentration are also crucial [44–46]. More obvious infection signs have been found in animal experiment after instillation of smaller size polystyrene particles [45]. The toxicity of some nanoparticles may also depend on concentration. Inflammatory processes appeared when the exposure concentration reached 0.5 mg/m^3 for multiwall carbon nanotubes and 10 mg/m^3 for graphene [42]. Significant inflammation could be observed when titanium dioxide was inhaled in high dose, compared with no significant pulmonary inflammation when it was inhaled in low and medium dose [47].

The toxicity of particles also depends on the position where the particles arrive and deposit [48]. Respiratory system has complicated bifurcate tree-structure airways which can be divided into conduction zone and respiratory zone. In conduction airway the particle matters may stick to the mucus and be removed with the help of cilia, as well as the phagocytosis of macrophage [49]. In alveoli, the important region for gas exchange, there is only macrophage protecting the body from infection [50]. When particles accumulate in alveoli, the pulmonary inflammation will be induced [17]. Thus the understanding of how nanoparticles transport and deposit is as important as the cytotoxic study.

3. The Means to Study Transport and Deposition of Nanoparticles

As the toxicity of nanoparticles has attracted great attention, the study of nanoparticles deposition is developing step by step. Many different methods have been used in particles deposition study, as shown in Figure 1. The study of particles transport and deposition could be classified as clinical or animal experiment studies and computer simulation studies. Each kind of study method is irreplaceable. They supplement each other. At first the relations between inhaled particle pollution and health were detected by epidemiological studies. At the same time clinical or animal experiment studies were conducted to understand the particles' deposition in respiratory system. Then mathematical models, including CFD model, were established to find more details of particles' transport and deposition.

The experiment studies include in vivo experiments and in vitro experiments. The respiratory tract deposition of particles could be determined from in vivo experiments during spontaneous breathing of volunteers, patients, and experimental animals [51–53]. For the reason of ethics, there are many limitations of in vivo experiments in volunteers and patients. For volunteers and patients, the total deposition fractions were derived by comparing the difference between

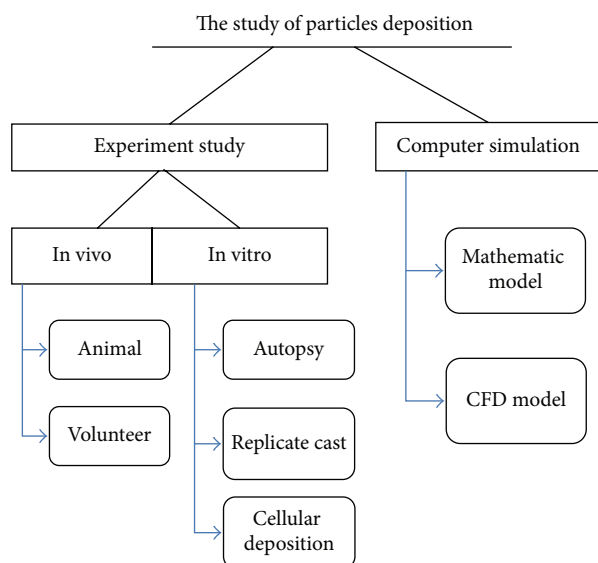


FIGURE 1: The classification of the method to study particles deposition.

inhaled and exhaled particle concentrations. In animal experiments, the accumulated particles were recovered and assessed from the excised tissue after sacrifice [54]. The lung tissue could be excised to proceed with pathological examination [55]. The response of the physiological system, such as the inflammation caused by inhaled particles [56], could be also observed during *in vivo* experiments. For patients and volunteers, induced sputum after inhalation could be obtained to analyze inflammation and immune function [52]. The *in vivo* experiment is good to observe the actual physiological response, but it is not enough to investigate the mechanism of transport, deposition, and toxicity of nanoparticles.

In the study of autopsy, the retained particles in human lung parenchyma could be examined [57], while, to understand how these particles were retained, some designed *in vitro* experiments proceeded. In the end of last century, many particle deposition experiments had been conducted with replicate human airway cast [15, 58, 59]. Gurman et al. and Cohen et al. used a replicate cast of human upper tracheobronchial tree to examine the deposition of particles [60, 61]. Some small airways were hard to build cast, so most of the casts were trimmed to airways with diameter >3 mm. In the study of Cohen et al., the replicate airway cast included 10-generation airway and retained 141 airways [58]. Most of the casts were made of silicone rubber [62] and just used to simulate the transport phenomenon of particles in tube; the deposition in cell was studied by cell exposure experiment [63]. The cell exposure experiment could be used to study the mechanism the toxicity of nanoparticles without cross-species correlation and ethical concerns, while the results of *in vitro* cell exposure experiment were different from those of *in vivo* experiment [64] because the cell culture system could not represent the multicellular organism.

To describe the transport and deposition of nanoparticles quantitatively, some mathematical models have been established based on the results of experiments [65]. Martin and

Finlay used a simple algebraic formulation to predict the total respiratory tract deposition fraction with an empirical fit to experiment data [66]. A two-compartment model has been established to describe the deposition and clearance of particles in surfactant layer of the alveolar surface and in the cell plasma of alveolar macrophages [67]. A semiempirical model has been used to study the particle deposition difference between a single breath and multiple breathing cycles [68]. This kind of mathematic model explained the result of experiment with lumped parameters, instead of providing detailed transport and deposition of local region.

It is difficult to observe and to accurately measure the local deposition of ultrafine particles in real-time experiment. Computational fluid dynamics (CFD) simulation could provide the detailed flow mechanics in airway and predict the deposition of nanoparticles [69]. In CFD studies, the structure of human airway is the basis for analyzing particle transport and deposition. The geometric model of airway was divided into tiny meshes; thus the deposition feature could be compared in very small local regions. The number of meshes and the time of simulation increase with the complexity of airway. Thus most of the CFD simulation just focused on some part of the airway. For example, Zhang and Kleinstreuer studied ultrafine particles deposition and heat transport with an oral airway model and G0–G3 airway model [70], and they studied inertial and gravitational deposition of microparticles in medium-size bronchial generations G6–G9 [71]. They also attempted to study the deposition in the entire tracheobronchial airway. Five levels of triple-bifurcation unit constituted a 16-generation model [72]. The simulation study was conducted for each triple-bifurcation unit. The respiratory zone of airway was not considered in existing CFD deposition studies because of the complexity of structure. Although the CFD technique has been utilized to study in many fields including the transport of particles in airway, the reliability of the simulation should be validated by data from experimental studies.

4. Factors Influence the Transport and Deposition of Particles in Respiratory System

The transport of particles with air flow in curved tubes of respiratory system can be described by fluid mechanics. In the study of gas-solid-two-phase flow, Stokes number is used to describe the behavior of particles in the flow, and Reynolds number is used to distinguish flow patterns. For low inspiratory flow rate, the transport of particles in airways can be described as laminar flow with secondary flow, while turbulence appears with the increase of flow rate [73]. Low Reynolds number $K-\omega$ model for turbulence can be used to study the transport and deposition of nanoparticles [74, 75]. Though the flow rate is oscillatory in spontaneous breathing, the flow fields seemed similar to those in steady state inhalation in case of the equivalent Reynolds number [76]. In most cases, the deposition fraction increases with the increase of Stokes number [77]. The deposition could also be influenced

by many factors, such as size of the particles, inhalation waveform, and also the structure of respiratory airway [12, 73, 78].

For the complicated airway structure, the deposition of particles is not uniform in the total respiratory system. Some parameters were introduced to describe the total and regional deposition. The deposition fraction (DF) is the mostly used not only for deposition in total respiratory system, but also for that in regional part, which is defined as the ratio of number of particles depositing to the number of particles entering the system. The deposition efficiency (DE) is derived as the ratio of particles depositing within a region to the particles entering that region. The deposition enhancement factor (DEF) is defined as the ratio of the number of particles depositing per unit area in local region to the average number of particles depositing per unit area in the whole bifurcation [79], which could indicate the deposition “hot spots” [12]. In the studies of Gurman et al., the replicate casts of human upper tracheobronchial model were used to examine the deposition of microparticles in 0–5 airway generations [60]. The DE of microparticles in each airway generation was different, especially between trachea and bronchi. The position-dependent deposition fraction feature also appears for nanoparticles. In the human tracheobronchial cast deposition experiments, Cohen showed the different DE of nanoparticles from airway generation 0 to generation 7 [58]. The DE in trachea (generation 0) was greater than that in main bronchi (generation 1), while the DF increased from the second generation airway to the sixth generation airway. In numerical study, the difference of deposition was also observed in great detail. The deposition fraction of different parts has been studied such as nasal cavity, nasopharynx, larynx, and trachea [80]. The deposition fraction in head airway is much higher than that in larynx and trachea. The local region with high DEF, meaning the hot spot of deposition, mainly occurs at the carinal ridges and the inside walls around the carinal ridges [12].

Size of particles plays an important role in particles transport and deposition in respiratory system. The transport of microparticles mainly depends on inertial impaction and sedimentation [71], while that of nanoparticles mostly relies on diffusion [74]. The particles in small scale are easier to enter the lung. From the analyses of particle content of autopsy lungs, it was found that the sizes of the particles and aggregates in autopsy lung were obviously smaller than the average sizes in air, which were mostly in nanoscale [25]. The places where particles deposit have great relation with particle size. For microparticles, the deposition in head airway is much greater than that in tracheobronchial and alveolar region. Only when the diameter of particle is less than 10 μm , the deposition in alveoli became obvious, and the ratio of the deposition in alveoli to that in total respiratory system increases remarkably for particles with diameter from 10 μm to 0.5 μm [81]. For nanoparticles, the total deposition and head airway deposition will increase with the decrease of nanoparticles diameter (from 100 nm to 1 nm) [82, 83]. In alveolar region and tracheobronchial region, the deposition fractions of nanoparticles increase firstly and then decrease along with the decrease of nanoparticle's diameter, while the deposition variations in these two regions are not synchronous [84].

The influence of flow rate on particles deposition has been studied by experiments and numerical simulation. In deposition experiments for microparticles and nanoparticles, it was found that the DE in high flow rate was less than that in low flow rate [58, 60]. The same results have been received from computer simulation that the flow rate may influence the deposition of particles [85]. While in some other measurement experiments, the influence of flow rate is not obvious [83], which may be because of the differences in the applied methodologies and the difference of airway model [84]. Besides the flow rate, the influence of inhale waveform has also been studied. The flow rate, cyclicity, and velocity inlet profile influence particle deposition to a certain extent [77, 78], while these influences seemed minor compared with the influence of particle size [12]. Some reports about flow influences were not coincident, which may be because of the difference of the airway models. It has been reported for microparticles, in bronchi, that the DE is greater under cyclic flow than under constant flow, but the DE in the entire tracheobronchial tree showed no observed difference under these two different means of flow [60].

The transport and deposition of nanoparticles in respiratory system also vary with age, lung function [51, 86, 87]. In volunteer respiratory tract deposition experiments, it was found that the deposition probability of nanoparticles had relations with the lung function and severity of the disease [51, 88]. In simulation study, there was a higher particle deposition rate for child than that for adults [75, 86]. The deposition variation is due to the difference of airway geometry and breath parameters. The deposition during exercise is obviously higher than that in rest, because of the different breath pattern [89]. The geometry model is also an important factor to study particles deposition. When considering the laryngeal model, the DF of microparticles in tracheobronchial airway increased, while that of nanoparticles in tracheobronchial decreased [90].

5. Other Techniques Involved in Particle Transport and Deposition Study

Some other techniques were also involved in the study of particles transport and deposition, such as medical imaging. Medical images can not only provide detailed anatomy structure of airway but also be used to observe the deposition in vivo. In some early studies, the airway casts were made from a cadaver [91]. With the development of medical imaging, the geometrical morphology of airway can be picked up from medical images. CT, MRI, and some other imaging techniques have been used in particles' transport and deposition study. Grgic et al. built a realistic extrathoracic model with simple geometric shape based on CT scan and MRI scan [92]. Then many realistic airway geometric models were constructed by CT scan and MRI scan [75, 80, 93], which make it possible to realize individual airway deposition CFD analysis. Together with the development of 3D printing technique [94], detailed individual airway solid model for in vitro experiment will be achievable.

Some molecular imaging techniques, which have been used to detect nanomedicine distribution, can also be used

in the deposition study of nanoparticles in respiratory system [95]. Fluorescent imaging has been used to detect the distribution of aerosols in each lung lobe [96]. The γ -camera has been used to scan bronchial airway after radiolabeled particles were inhaled [52]. SPECT and PET have been used to measure the deposition and postdeposition kinetics of some aerosol in the lung [97, 98]. Although the developed imaging technique such as PET can provide three-dimension kinetics of the tracers' distribution, up to now the poor spatial resolution is still the limitation to observing the transport process in detail.

Besides the knowledge on defense against the toxicity of nanoparticles, the transport and deposition of nanoparticles also have another potential application. Medicine in nanoscale could be inhaled through the tracheobronchial airways down into the alveolar region [32, 99]. The transport and deposition study of nanoparticles may also provide useful information for aerosol drug delivering system. With the assistance of medical imaging, the personalized risk assessment and individual drug delivery scheme could be achieved in future.

6. Conclusions

More and more nanoproducts appear together with the concern about the toxicity of nanoparticles by inhalation. Not only in occupational conditions but also in resident conditions, airborne nanoparticles have been detected, which bring the risk of toxicity by inhalation. Though strict exposure limits have been established to protect human body from the toxicity of airborne nanoparticles [100], knowledge on the transport and deposition of nanoparticles is also significant.

In this review, the methods for the particles deposition studies have been classified and listed. The advantages and disadvantages of each method have been mentioned. The nonuniform deposition feature of nanoparticles has been described, and the effect of factors of their transport and deposition has been discussed. The flow rate, respiratory pattern, and even individual airway structure may influence the particles deposition. The combination of medical imaging and other techniques may promote the study of the particle deposition.

Conflict of Interests

The authors declare that there is no conflict of interests regarding the publication of this paper.

Acknowledgments

This work was supported by National Nature Science Foundation of China (Grants nos. 81101123, 61108084, 61201313, 61190123, and 11272039), National Key Technology R&D Program (2012BAI14B04), Beijing Higher Education Young Elite Teacher Project, and the Fundamental Research Funds for the Central Universities of China.

References

- [1] L. T. Wang, Z. Wei, J. Yang et al., "The 2013 severe haze over southern Hebei, China: model evaluation, source apportionment, and policy implications," *Atmospheric Chemistry and Physics*, vol. 14, no. 6, pp. 3151–3173, 2014.
- [2] Y. Wang, L. Yao, L. Wang et al., "Mechanism for the formation of the January 2013 heavy haze pollution episode over central and eastern China," *Science China Earth Sciences*, vol. 57, no. 1, pp. 14–25, 2014.
- [3] Z. Cheng, J. Jiang, O. Fajardo, S. Wang, and J. Hao, "Characteristics and health impacts of particulate matter pollution in China (2001–2011)," *Atmospheric Environment*, vol. 65, pp. 186–194, 2013.
- [4] W. Li, C. Wang, H. Wang et al., "Distribution of atmospheric particulate matter (PM) in rural field, rural village and urban areas of northern China," *Environmental Pollution*, vol. 185, pp. 134–140, 2014.
- [5] Y. Sun, G. Zhuang, Y. Wang et al., "The air-borne particulate pollution in Beijing—concentration, composition, distribution and sources," *Atmospheric Environment*, vol. 38, no. 35, pp. 5991–6004, 2004.
- [6] Y. Cheng, G. Engling, K.-B. He et al., "The characteristics of Beijing aerosol during two distinct episodes: impacts of biomass burning and fireworks," *Environmental Pollution*, vol. 185, pp. 149–157, 2014.
- [7] D. B. Kittelson, W. F. Watts, and J. P. Johnson, "Nanoparticle emissions on Minnesota highways," *Atmospheric Environment*, vol. 38, no. 1, pp. 9–19, 2004.
- [8] D. B. Kittelson, W. F. Watts, and J. P. Johnson, "On-road and laboratory evaluation of combustion aerosols—part I: summary of diesel engine results," *Journal of Aerosol Science*, vol. 37, no. 8, pp. 913–930, 2006.
- [9] D. B. Kittelson, "Engines and nanoparticles: a review," *Journal of Aerosol Science*, vol. 29, no. 5–6, pp. 575–588, 1998.
- [10] D. Tang, T. Y. Li, J. C. Chow et al., "Air pollution effects on fetal and child development: a cohort comparison in China," *Environmental Pollution*, vol. 185, pp. 90–96, 2014.
- [11] G. Oberdörster, J. N. Finkelstein, C. Johnston et al., "Acute pulmonary effects of ultrafine particles in rats and mice," *Research Report*, no. 96, pp. 5–75, 2000.
- [12] Z. Zhang and C. Kleinstreuer, "Airflow structures and nanoparticle deposition in a human upper airway model," *Journal of Computational Physics*, vol. 198, no. 1, pp. 178–210, 2004.
- [13] V. Stone, H. Johnston, and M. J. D. Clift, "Air pollution, ultrafine and nanoparticle toxicology: cellular and molecular interactions," *IEEE Transactions on Nanobioscience*, vol. 6, no. 4, pp. 331–340, 2007.
- [14] Z. Abidin, M. A. Alim, R. Saidur et al., "Solar energy harvesting with the application of nanotechnology," *Renewable and Sustainable Energy Reviews*, vol. 26, pp. 837–852, 2013.
- [15] R. Lehner, X. Wang, S. Marsch, and P. Hunziker, "Intelligent nanomaterials for medicine: carrier platforms and targeting strategies in the context of clinical application," *Nanomedicine: Nanotechnology, Biology, and Medicine*, vol. 9, no. 6, pp. 742–757, 2013.
- [16] I. Gosens, J. A. Post, L. J. J. de la Fonteyne et al., "Impact of agglomeration state of nano- and submicron sized gold particles on pulmonary inflammation," *Particle and Fibre Toxicology*, vol. 7, article 37, 2010.

- [17] H. M. Braakhuis, M. V. D. Z. Park, I. Gosens, W. H. de Jong, and F. R. Cassee, "Physicochemical characteristics of nanomaterials that affect pulmonary inflammation," *Particle and Fibre Toxicology*, vol. 11, no. 1, article 18, 2014.
- [18] G. Oberdörster, E. Oberdörster, and J. Oberdörster, "Nanotoxicology: an emerging discipline evolving from studies of ultrafine particles," *Environmental Health Perspectives*, vol. 113, no. 7, pp. 823–839, 2005.
- [19] E. R. Weibel, B. Sapoval, and M. Filoche, "Design of peripheral airways for efficient gas exchange," *Respiratory Physiology & Neurobiology*, vol. 148, no. 1–2, pp. 3–21, 2005.
- [20] E. R. Weibel, *Morphometry of the Human Lung*, Springer, New York, NY, USA, 1963.
- [21] K. R. Smith, J. M. Samet, I. Romieu, and N. Bruce, "Indoor air pollution in developing countries and acute lower respiratory infections in children," *Thorax*, vol. 55, no. 6, pp. 518–532, 2000.
- [22] M. A. Reyna-Carranza, A. P. Moreno-Flores, and R. Lopez-Avitia, "Acute respiratory infections and its Spearman correlation with meteorological and air pollutants data from Mexicali, BC, Mexico," in *Proceedings of the Pan American Health Care Exchange (PAHCE '10)*, p. 17, Lima, Peru, March 2010.
- [23] M. Lippmann, K. Ito, A. Nadas, and R. T. Burnett, "Association of particulate matter components with daily mortality and morbidity in urban populations," *Research Report*, no. 95, pp. 5–82, 2000.
- [24] B. Brunekreef and S. T. Holgate, "Air pollution and health," *The Lancet*, vol. 360, no. 9341, pp. 1233–1242, 2002.
- [25] M. Brauer, C. Avila-Casado, T. I. Fortoul, S. Vedal, B. Stevens, and A. Churg, "Air pollution and retained particles in the lung," *Environmental Health Perspectives*, vol. 109, no. 10, pp. 1039–1043, 2001.
- [26] A. Ibaldo-Mulli, H. E. Wichmann, W. Kreyling, and A. Peters, "Epidemiological evidence on health effects of ultrafine particles," *Journal of Aerosol Medicine: Deposition, Clearance, and Effects in the Lung*, vol. 15, no. 2, pp. 189–201, 2002.
- [27] C. A. Pope III, R. T. Burnett, M. J. Thun et al., "Lung cancer, cardiopulmonary mortality, and long-term exposure to fine particulate air pollution," *Journal of the American Medical Association*, vol. 287, no. 9, pp. 1132–1141, 2002.
- [28] R. R. Mercer, A. F. Hubbs, J. F. Scabilloni et al., "Distribution and persistence of pleural penetrations by multi-walled carbon nanotubes," *Particle and Fibre Toxicology*, vol. 7, article 28, 2010.
- [29] N. R. Yacobi, H. C. Phuleria, L. Demaio et al., "Nanoparticle effects on rat alveolar epithelial cell monolayer barrier properties," *Toxicology in Vitro*, vol. 21, no. 8, pp. 1373–1381, 2007.
- [30] G. S. Kang, P. A. Gillespie, A. Gunnison, A. L. Moreira, K.-M. Tchou-Wong, and L.-C. Chen, "Long-term inhalation exposure to nickel nanoparticles exacerbated atherosclerosis in a susceptible mouse model," *Environmental Health Perspectives*, vol. 119, no. 2, pp. 176–181, 2011.
- [31] W. Lin, Y. Xu, C.-C. Huang et al., "Toxicity of nano- and micro-sized ZnO particles in human lung epithelial cells," *Journal of Nanoparticle Research*, vol. 11, no. 1, pp. 25–39, 2009.
- [32] S. Sultana, R. Ali, S. Talegaonkar, F. J. Ahmad, G. Mittal, and A. Bhatnagar, "In vivo lung deposition and sub-acute inhalation toxicity studies of nano-sized alendronate sodium as an antidote for inhaled toxic substances in Sprague Dawley rats," *Environmental Toxicology and Pharmacology*, vol. 36, no. 2, pp. 636–647, 2013.
- [33] L. Wang, L. Wang, W. Ding, and F. Zhang, "Acute toxicity of ferric oxide and zinc oxide nanoparticles in rats," *Journal of Nanoscience and Nanotechnology*, vol. 10, no. 12, pp. 8617–8624, 2010.
- [34] M. Ho, K.-Y. Wu, H.-M. Chein, L.-C. Chen, and T.-J. Cheng, "Pulmonary toxicity of inhaled nanoscale and fine zinc oxide particles: mass and surface area as an exposure metric," *Inhalation Toxicology*, vol. 23, no. 14, pp. 947–956, 2011.
- [35] W.-S. Cho, R. Duffin, S. E. M. Howie et al., "Progressive severe lung injury by zinc oxide nanoparticles; the role of Zn²⁺ dissolution inside lysosomes," *Particle and Fibre Toxicology*, vol. 8, article 27, 2011.
- [36] P. V. Rajsekhar, G. Selvam, A. Goparaju, P. B. Murthy, and P. N. Reddy, "Pulmonary responses of manufactured ultrafine aluminum oxide particles upon repeated exposure by inhalation in rats," *Indian Journal of Forensic Medicine and Toxicology*, vol. 7, no. 1, pp. 147–153, 2013.
- [37] W.-S. Cho, R. Duffin, F. Thielbeer et al., "Zeta potential and solubility to toxic ions as mechanisms of lung inflammation caused by metal/metal oxide nanoparticles," *Toxicological Sciences*, vol. 126, no. 2, pp. 469–477, 2012.
- [38] W.-S. Cho, R. Duffin, C. A. Poland et al., "Metal oxide nanoparticles induce unique inflammatory footprints in the lung: important implications for nanoparticle testing," *Environmental Health Perspectives*, vol. 118, no. 12, pp. 1699–1706, 2010.
- [39] A. Srinivas, P. J. Rao, G. Selvam, A. Goparaju, B. P. Murthy, and N. P. Reddy, "Oxidative stress and inflammatory responses of rat following acute inhalation exposure to iron oxide nanoparticles," *Human & Experimental Toxicology*, vol. 31, no. 11, pp. 1113–1131, 2012.
- [40] J. L. Blum, L. K. Rosenblum, G. Grunig, M. B. Beasley, J. Q. Xiong, and J. T. Zelikoff, "Short-term inhalation of cadmium oxide nanoparticles alters pulmonary dynamics associated with lung injury, inflammation, and repair in a mouse model," *Inhalation Toxicology*, vol. 26, no. 1, pp. 48–58, 2014.
- [41] G. S. Kang, P. A. Gillespie, A. Gunnison, H. Rengifo, J. Koberstein, and L.-C. Chen, "Comparative pulmonary toxicity of inhaled nickel nanoparticles; Role of deposited dose and solubility," *Inhalation Toxicology*, vol. 23, no. 2, pp. 95–103, 2011.
- [42] L. Ma-Hock, V. Strauss, S. Treumann et al., "Comparative inhalation toxicity of multi-wall carbon nanotubes, graphene, graphite nanoplatelets and low surface carbon black," *Particle and Fibre Toxicology*, vol. 10, no. 1, article 23, 2013.
- [43] C. M. Sayes, K. L. Reed, K. P. Glover et al., "Changing the dose metric for inhalation toxicity studies: short-term study in rats with engineered aerosolized amorphous silica nanoparticles," *Inhalation Toxicology*, vol. 22, no. 4, pp. 348–354, 2010.
- [44] M. Lundqvist, J. Stigler, G. Elia, I. Lynch, T. Cedervall, and K. A. Dawson, "Nanoparticle size and surface properties determine the protein corona with possible implications for biological impacts," *Proceedings of the National Academy of Sciences of the United States of America*, vol. 105, no. 38, pp. 14265–14270, 2008.
- [45] D. M. Brown, M. R. Wilson, W. MacNee, V. Stone, and K. Donaldson, "Size-dependent proinflammatory effects of ultrafine polystyrene particles: a role for surface area and oxidative stress in the enhanced activity of ultrafines," *Toxicology and Applied Pharmacology*, vol. 175, no. 3, pp. 191–199, 2001.
- [46] T. Stoeger, C. Reinhard, S. Takenaka et al., "Instillation of six different ultrafine carbon particles indicates a surface area threshold dose for acute lung inflammation in mice," *Environmental Health Perspectives*, vol. 114, no. 3, pp. 328–333, 2006.
- [47] W. McKinney, M. Jackson, T. M. Sager et al., "Pulmonary and cardiovascular responses of rats to inhalation of a commercial

- antimicrobial spray containing titanium dioxide nanoparticles,” *Inhalation Toxicology*, vol. 24, no. 7, pp. 447–457, 2012.
- [48] P. Gehr and J. Heyder, *Particle-Lung Interactions*, Taylor & Francis, London, UK, 2000.
- [49] M. Geiser, “Update on macrophage clearance of inhaled micro- and nanoparticles,” *Journal of Aerosol Medicine and Pulmonary Drug Delivery*, vol. 23, no. 4, pp. 207–217, 2010.
- [50] A. Vander, J. Sherman, and D. Luciano, *Human Physiology: The Mechanisms of Body Function*, McGraw-Hill, New York, NY, USA, 8th edition, 2001.
- [51] J. Löndahl, E. Swietlicki, J. Rissler et al., “Experimental determination of the respiratory tract deposition of diesel combustion particles in patients with chronic obstructive pulmonary disease,” *Particle and Fibre Toxicology*, vol. 9, article 30, 2012.
- [52] N. E. Alexis, J. C. Lay, K. Zeman et al., “Biological material on inhaled coarse fraction particulate matter activates airway phagocytes in vivo in healthy volunteers,” *Journal of Allergy and Clinical Immunology*, vol. 117, no. 6, pp. 1396–1403, 2006.
- [53] L. Geraets, A. G. Oomen, J. D. Schroeter, V. A. Coleman, and F. R. Cassee, “Tissue distribution of inhaled micro- and nano-sized cerium oxide particles in rats: results from a 28-day exposure study,” *Toxicological Sciences*, vol. 127, no. 2, pp. 463–473, 2012.
- [54] J. H. Vincent, A. M. Johnston, A. D. Jones, R. E. Bolton, and J. Addison, “Kinetics of deposition and clearance of inhaled mineral dusts during chronic exposure,” *British Journal of Industrial Medicine*, vol. 42, no. 10, pp. 707–715, 1985.
- [55] G. Oberdorster, J. Ferin, and B. E. Lehnert, “Correlation between particle size, in vivo particle persistence, and lung injury,” *Environmental Health Perspectives*, vol. 102, no. 5, pp. 173–179, 1994.
- [56] K. Ogino, R. Zhang, H. Takahashi et al., “Allergic airway inflammation by nasal inoculation of particulate matter (PM_{2.5}) in NC/Nga mice,” *PLoS ONE*, vol. 9, no. 3, Article ID e92710, 2014.
- [57] A. Churg and M. Brauer, “Human lung parenchyma retains PM_{2.5},” *American Journal of Respiratory and Critical Care Medicine*, vol. 155, no. 6, pp. 2109–2111, 1997.
- [58] B. S. Cohen, R. G. Sussman, and M. Lippmann, “Ultrafine particle deposition in a human tracheobronchial cast,” *Aerosol Science and Technology*, vol. 12, no. 4, pp. 1082–1091, 1990.
- [59] D. L. Swift, N. Montassier, P. K. Hopke, K. Karpen-Hayes, Y.-S. Cheng, and J. C. Strong, “Inspiratory deposition of ultrafine particles in human nasal replicate cast,” *Journal of Aerosol Science*, vol. 23, no. 1, pp. 65–72, 1992.
- [60] J. L. Gurman, M. Lippmann, and R. B. Schlesinger, “Particle deposition in replicate casts of the human upper tracheobronchial tree under constant and cyclic inspiratory flow. I. Experimental,” *Aerosol Science and Technology*, vol. 3, no. 3, pp. 245–252, 1984.
- [61] B. S. Cohen and B. Asgharian, “Deposition of ultrafine particles in the upper airways: an empirical analysis,” *Journal of Aerosol Science*, vol. 21, no. 6, pp. 789–797, 1990.
- [62] Y.-S. Cheng, Y. Zhou, and B. T. Chen, “Particle deposition in a cast of human oral airways,” *Aerosol Science and Technology*, vol. 31, no. 4, pp. 286–300, 1999.
- [63] E. Fröhlich and S. Salar-Behzadi, “Toxicological assessment of inhaled nanoparticles: role of in vivo, ex vivo, in vitro, and in Silico Studies,” *International Journal of Molecular Sciences*, vol. 15, no. 3, pp. 4795–4822, 2014.
- [64] C. M. Sayes, K. L. Reed, and D. B. Warheit, “Assessing toxicology of fine and nanoparticles: comparing in vitro measurements to in vivo pulmonary toxicity profiles,” *Toxicological Sciences*, vol. 97, no. 1, pp. 163–180, 2007.
- [65] S. S. Park and A. S. Wexler, “Particle deposition in the pulmonary region of the human lung: a semi-empirical model of single breath transport and deposition,” *Journal of Aerosol Science*, vol. 38, no. 2, pp. 228–245, 2007.
- [66] A. R. Martin and W. H. Finlay, “A general, algebraic equation for predicting total respiratory tract deposition of micrometer-sized aerosol particles in humans,” *Journal of Aerosol Science*, vol. 38, no. 2, pp. 246–253, 2007.
- [67] W. Koch and W. Stöber, “A simple pulmonary retention model accounting for dissolution and macrophage-mediated removal of deposited polydisperse particles,” *Inhalation Toxicology*, vol. 13, no. 2, pp. 129–148, 2001.
- [68] S. S. Park and A. S. Wexler, “Size-dependent deposition of particles in the human lung at steady-state breathing,” *Journal of Aerosol Science*, vol. 39, no. 3, pp. 266–276, 2008.
- [69] C. Kleinstreuer, Z. Zhang, and Z. Li, “Modeling airflow and particle transport/deposition in pulmonary airways,” *Respiratory Physiology and Neurobiology*, vol. 163, no. 1–3, pp. 128–138, 2008.
- [70] Z. Zhang and C. Kleinstreuer, “Species heat and mass transfer in a human upper airway model,” *International Journal of Heat and Mass Transfer*, vol. 46, no. 25, pp. 4755–4768, 2003.
- [71] C. Kleinstreuer, Z. Zhang, and C. S. Kim, “Combined inertial and gravitational deposition of microparticles in small model airways of a human respiratory system,” *Journal of Aerosol Science*, vol. 38, no. 10, pp. 1047–1061, 2007.
- [72] Z. Zhang, C. Kleinstreuer, and C. S. Kim, “Comparison of analytical and CFD models with regard to micron particle deposition in a human 16-generation tracheobronchial airway model,” *Journal of Aerosol Science*, vol. 40, no. 1, pp. 16–28, 2009.
- [73] C. Kleinstreuer and Z. Zhang, “Laminar-to-turbulent fluid-particle flows in a human airway model,” *International Journal of Multiphase Flow*, vol. 29, no. 2, pp. 271–289, 2003.
- [74] Z. Zhang, C. Kleinstreuer, J. F. Donohue, and C. S. Kim, “Comparison of micro- and nano-size particle depositions in a human upper airway model,” *Journal of Aerosol Science*, vol. 36, no. 2, pp. 211–233, 2005.
- [75] J. Xi, X. Si, J. W. Kim, and A. Berlinski, “Simulation of airflow and aerosol deposition in the nasal cavity of a 5-year-old child,” *Journal of Aerosol Science*, vol. 42, no. 3, pp. 156–173, 2011.
- [76] Z. Li, C. Kleinstreuer, and Z. Zhang, “Simulation of airflow fields and microparticle deposition in realistic human lung airway models. Part I: airflow patterns,” *European Journal of Mechanics, B/Fluids*, vol. 26, no. 5, pp. 632–649, 2007.
- [77] Z. Li, C. Kleinstreuer, and Z. Zhang, “Simulation of airflow fields and microparticle deposition in realistic human lung airway models. Part II: particle transport and deposition,” *European Journal of Mechanics, B/Fluids*, vol. 26, no. 5, pp. 650–668, 2007.
- [78] Z. Li, C. Kleinstreuer, and Z. Zhang, “Particle deposition in the human tracheobronchial airways due to transient inspiratory flow patterns,” *Journal of Aerosol Science*, vol. 38, no. 6, pp. 625–644, 2007.
- [79] I. Balásházy, T. Heistracher, and W. Hofmann, “Deposition enhancement factors for inhaled radon decay products in bronchial airway bifurcations,” *Journal of Aerosol Science*, vol. 28, supplement 1, pp. S597–S598, 1997.
- [80] P. Farhadi Ghalati, E. Keshavarzian, O. Abouali, A. Faramarzi, J. Tu, and A. Shakibafard, “Numerical analysis of micro- and nano-particle deposition in a realistic human upper airway,” *Computers in Biology and Medicine*, vol. 42, no. 1, pp. 39–49, 2012.

- [81] T. C. Carvalho, J. I. Peters, and R. O. Williams III, "Influence of particle size on regional lung deposition—what evidence is there?" *International Journal of Pharmaceutics*, vol. 406, no. 1-2, pp. 1–10, 2011.
- [82] P. W. Longest and L. T. Holbrook, "In silico models of aerosol delivery to the respiratory tract—development and applications," *Advanced Drug Delivery Reviews*, vol. 64, no. 4, pp. 296–311, 2012.
- [83] K.-H. Cheng, Y.-S. Cheng, H.-C. Yeh, and D. L. Swift, "An experimental method for measuring aerosol deposition efficiency in the human oral airway," *American Industrial Hygiene Association Journal*, vol. 58, no. 3, pp. 207–213, 1997.
- [84] J. Löndahl, W. Möller, J. H. Pagels, W. G. Kreyling, E. Swietlicki, and O. Schmid, "Measurement techniques for respiratory tract deposition of airborne nanoparticles: a critical review," *Journal of Aerosol Medicine and Pulmonary Drug Delivery*, vol. 27, no. 4, pp. 229–254, 2014.
- [85] W. Li, J. Q. Xiong, and B. S. Cohen, "The deposition of unattached radon progeny in a tracheobronchial cast as measured with iodine vector," *Aerosol Science and Technology*, vol. 28, no. 6, pp. 502–510, 1998.
- [86] E. Keshavarzian, P. F. Ghalati, O. Abouali, G. Ahmadi, and M. H. Bagheri, "Micro/Nano-particle deposition in the airway of a 6-year-old child from nostril to the third generation," in *Proceedings of the Asme Fluids Engineering Division Summer Meeting*, vol. 1 of *Symposia, Parts A and B*, pp. 831–837, American Society of Mechanical Engineer, Rio Grande, Puerto Rico, USA, 2012.
- [87] P. A. Jaques and C. S. Kim, "Measurement of total lung deposition of inhaled ultrafine particles in healthy men and women," *Inhalation Toxicology*, vol. 12, no. 8, pp. 715–731, 2000.
- [88] J. S. Brown, K. L. Zeman, and W. D. Bennett, "Ultrafine particle deposition and clearance in the healthy and obstructed lung," *The American Journal of Respiratory and Critical Care Medicine*, vol. 166, no. 9, pp. 1240–1247, 2002.
- [89] C. C. Daigle, D. C. Chalupa, F. R. Gibb et al., "Ultrafine particle deposition in humans during rest and exercise," *Inhalation Toxicology*, vol. 15, no. 6, pp. 539–552, 2003.
- [90] J. Xi, P. W. Longest, and T. B. Martonen, "Effects of the laryngeal jet on nano- and microparticle transport and deposition in an approximate model of the upper tracheobronchial airways," *Journal of Applied Physiology*, vol. 104, no. 6, pp. 1761–1777, 2008.
- [91] K.-H. Cheng, Y.-S. Cheng, H.-C. Yen, and D. L. Swift, "Measurements of airway dimensions and calculation of mass transfer characteristics of the human oral passage," *Journal of Biomechanical Engineering*, vol. 119, no. 4, pp. 476–482, 1997.
- [92] B. Grgic, W. H. Finlay, and A. F. Heenan, "Regional aerosol deposition and flow measurements in an idealized mouth and throat," *Journal of Aerosol Science*, vol. 35, no. 1, pp. 21–32, 2004.
- [93] J. Xi and P. W. Longest, "Transport and deposition of micro-aerosols in realistic and simplified models of the oral airway," *Annals of Biomedical Engineering*, vol. 35, no. 4, pp. 560–581, 2007.
- [94] F. Rengier, A. Mehndiratta, H. von Tengg-Kobligk et al., "3D printing based on imaging data: review of medical applications," *International Journal of Computer Assisted Radiology and Surgery*, vol. 5, no. 4, pp. 335–341, 2010.
- [95] H. Chrystyn, "Methods to identify drug deposition in the lungs following inhalation," *British Journal of Clinical Pharmacology*, vol. 51, no. 4, pp. 289–299, 2001.
- [96] D. Yi, A. Price, A. Panoskaltis-Mortari, A. Naqwi, and T. S. Wiedmann, "Measurement of the distribution of aerosols among mouse lobes by fluorescent imaging," *Analytical Biochemistry*, vol. 403, no. 1-2, pp. 88–93, 2010.
- [97] S. Eberl, H.-K. Chan, and E. Daviskas, "SPECT imaging for radioaerosol deposition and clearance studies," *Journal of Aerosol Medicine: Deposition, Clearance, and Effects in the Lung*, vol. 19, no. 1, pp. 8–20, 2006.
- [98] M. S. Berridge, Z. Lee, and D. L. Heald, "Pulmonary distribution and kinetics of inhaled [¹¹C]triamcinolone acetonide," *Journal of Nuclear Medicine*, vol. 41, no. 10, pp. 1603–1611, 2000.
- [99] M. M. Bailey and C. J. Berkland, "Nanoparticle formulations in pulmonary drug delivery," *Medicinal Research Reviews*, vol. 29, no. 1, pp. 196–212, 2009.
- [100] P. A. Schulte, V. Murashov, R. Zumwalde, E. D. Kuempel, and C. L. Geraci, "Occupational exposure limits for nanomaterials: state of the art," *Journal of Nanoparticle Research*, vol. 12, no. 6, pp. 1971–1987, 2010.

文献收录被引及期刊影响因子排名分区检索证明

作者姓名: 乔惠婷 (Qiao, Huiting)

经检索“网络版科学引文索引 (SCI-EXPANDED)”数据库, 该作者发表的论文 (2008 年--2016 年) 被收录 6 篇, 被引用 3 次, 其中他引 2 次, 论文收录被引及期刊影响因子排名分区等信息详见附件所列。

注明: 1) 他引定义: 文献被除作者及合作者以外的其他人的引用。

2) 所有他引只计算被 SCIE 收录的论文进行的引用。

检索结果见附件, 共 7 页。

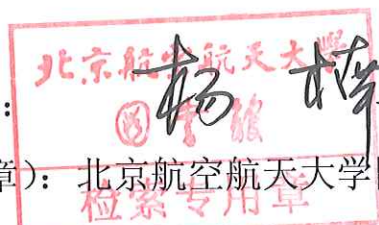
检索时间为 2016 年 5 月 24 日。

特此证明!

证明人 (签字):

证明单位 (盖章): 北京航空航天大学图书馆

二〇一六年五月二十四日



附件:

Record 1 of 6

Title: The Transport and Deposition of Nanoparticles in Respiratory System by Inhalation

一作第1

Author(s): Qiao, HT (Qiao, Huiting); Liu, WY (Liu, Wenyong); Gu, HY (Gu, Hongyu); Wang, DF (Wang, Daifa); Wang, Y (Wang, Yu)

Source: JOURNAL OF NANOMATERIALS Article Number: 394507 DOI: 10.1155/2015/394507

Published: 2015

Times Cited in Web of Science Core Collection: 1

Total Times Cited: 1

Accession Number: WOS:000355431300001

Language: English

Document Type: Review

Addresses: [Qiao, Huiting; Liu, Wenyong; Gu, Hongyu; Wang, Daifa; Wang, Yu] Beihang Univ, Sch Biol Sci & Med Engn, Key Lab Biomech & Mechanobiol, Minist Educ, Beijing 100191, Peoples R China.

[Qiao, Huiting] Drexel Univ, Sch Biomed Engn Sci & Hlth Syst, Philadelphia, PA 19104 USA.

Reprint Address: Wang, Y (reprint author), Beihang Univ, Sch Biol Sci & Med Engn, Key Lab Biomech & Mechanobiol, Minist Educ, Beijing 100191, Peoples R China.

E-mail Addresses: wangyu@buaa.edu.cn

IDS Number: CJ4CG

ISSN: 1687-4110

eISSN: 1687-4129

Source Item Page Count: 8

JOURNAL OF NANOMATERIALS



Impact Factor

1.644 1.798

2014 5 year

JCR® Category	Rank in Category	Quartile in Category
MATERIALS SCIENCE, MULTIDISCIPLINARY	122 of 260	Q2
NANOSCIENCE & NANOTECHNOLOGY	48 of 80	Q3

Data from the 2014 edition of Journal Citation Reports®

Publisher

HINDAWI PUBLISHING CORPORATION, 410 PARK AVENUE, 15TH FLOOR, #287
PMB, NEW YORK, NY 10022 USA

ISSN: 1687-4110

eISSN: 1687-4129

被引文献共计 1 篇(in SCIE), 其中他引文献 1 篇:

Record 1 of 1

Title: Role of Physicochemical Properties in Nanoparticle Toxicity

Author(s): Shin, SW (Shin, Seung Won); Song, IH (Song, In Hyun); Um, SH (Um, Soong Ho)

Source: NANOMATERIALS Volume: 5 Issue: 3 Pages: 1351-1365 DOI: 10.3390/nano5031351
Published: SEP 2015
Accession Number: WOS:000362643900014
ISSN: 2079-4991

Record 2 of 6

通讯第一

Title: The three-dimensional shape analysis of the M1 segment of the middle cerebral artery using MRA at 3T

Author(s): Han, JT (Han, Jintao); Qiao, HT (Qiao, Huiting); Li, X (Li, Xuan); Li, XG (Li, Xiaogang); He, QY (He, Qingyuan); Wang, Y (Wang, Yu); Cheng, ZM (Cheng, Ziman)

Source: NEURORADIOLOGY Volume: 56 Issue: 11 Pages: 995-1005 DOI: 10.1007/s00234-014-1414-3 Published: NOV 2014

Times Cited in Web of Science Core Collection: 0

Total Times Cited: 0

Accession Number: WOS:000344345800010

Language: English

Document Type: Article

Addresses: [Han, Jintao; Li, Xuan] Peking Univ, Hosp 3, Dept Intervent Radiol & Vasc Surg, Beijing 100871, Peoples R China.

[Qiao, Huiting; Wang, Yu; Cheng, Ziman] Beihang Univ, Sch Biol Sci & Med Engn, Beijing 100191, Peoples R China.

[Li, Xuan] Peking Univ, Hosp 3, Dept Neurol, Beijing 100871, Peoples R China.

[He, Qingyuan] Peking Univ, Hosp 3, Dept Radiol, Beijing 100871, Peoples R China.

Reprint Address: Qiao, HT (reprint author), Beihang Univ, Sch Biol Sci & Med Engn, Beijing 100191, Peoples R China.

E-mail Addresses: qht@buaa.edu.cn

IDS Number: AS5ZW

ISSN: 0028-3940

eISSN: 1432-1920

Source Item Page Count: 11

宝
中
专



Impact Factor

2.485 2.672

2014 5 year

JCR® Category	Rank in Category	Quartile in Category
CLINICAL NEUROLOGY	80 of 192	Q2
NEUROIMAGING	7 of 14	Q2
RADIOLOGY, NUCLEAR MEDICINE & MEDICAL IMAGING	41 of 125	Q2

Data from the 2014 edition of Journal Citation Reports®

Publisher
SPRINGER, 233 SPRING ST. NEW YORK, NY 10013 USA

ISSN: 0028-3940
eISSN: 1432-1920

被引文献共计 0 篇 (in SCIE), 其中他引文献 0 篇。

Record 3 of 6

一作第2

Title: A study of the metabolism of transplanted tumor in the lung by micro PET/CT in mice

Author(s): Qiao, HT (Qiao, Huiting); Li, J (Li, Jun); Chen, YM (Chen, Yingmao); Wang, DF (Wang, Daifa); Han, JT (Han, Jintao); Mei, MQ (Mei, Mengqi); Li, DY (Li, Deyu)

Source: MEDICAL ENGINEERING & PHYSICS Volume: 36 Issue: 3 Pages: 294-299 DOI: 10.1016/j.medengphy.2013.11.012 Published: MAR 2014

Times Cited in Web of Science Core Collection: 0

Total Times Cited: 0

Accession Number: WOS:000334008700003

Language: English

Document Type: Article

Addresses: [Qiao, Huiting; Wang, Daifa; Mei, Mengqi; Li, Deyu] Beihang Univ, Minist Educ, Sch Biol Sci & Med Engn, Key Lab Biomech & Mechanobiol, Beijing 100191, Peoples R China.

[Li, Jun] Peking Univ, Lab Anim Ctr, Beijing 100871, Peoples R China.

[Chen, Yingmao] Gen Hosp PLA, Dept Nucl Med, Beijing 100853, Peoples R China.

[Han, Jintao] Peking Univ, Hosp 3, Dept Intervent Radiol & Vasc Surg, Beijing 100191, Peoples R China.

Reprint Address: Li, DY (reprint author), Beihang Univ, Minist Educ, Sch Biol Sci & Med Engn, Key Lab Biomech & Mechanobiol, Beijing 100191, Peoples R China.

E-mail Addresses: deyuli@buaa.edu.cn

IDS Number: AE5DT

ISSN: 1350-4533

eISSN: 1873-4030

Source Item Page Count: 6



Impact Factor

1.825 **2.223**

2014

5 year

JCR® Category	Rank in Category	Quartile in Category
ENGINEERING, BIOMEDICAL	35 of 76	Q2

Data from the 2014 edition of Journal Citation Reports®

Publisher

ELSEVIER SCI LTD, THE BOULEVARD, LANGFORD LANE, KIDLINGTON, OXFORD
OX5 1GB, OXON, ENGLAND

ISSN: 1350-4533

eISSN: 1873-4030

被引文献共计 0 篇 (in SCIE), 其中他引文献 0 篇。

Record 4 of 6

Title: The effect of tumor size on the imaging diagnosis: A study based on simulation

一作第3

Author(s): Qiao, HT (Qiao, Huiting); Wang, LB (Wang, Libin); Li, DY (Li, Deyu); Wang, DF (Wang, Daifa); Wang, Y (Wang, Yu)

Source: BIO-MEDICAL MATERIALS AND ENGINEERING Volume: 24 Issue: 6 Pages:
3129-3136 DOI: 10.3233/BME-141135 Published: 2014

Times Cited in Web of Science Core Collection: 0

Total Times Cited: 0

Accession Number: WOS:000343005700138

Language: English

Document Type: Article

Addresses: [Qiao, Huiting; Wang, Libin; Li, Deyu; Wang, Daifa; Wang, Yu] Beihang Univ, Sch Biol Sci & Med Engn, Beijing 100191, Peoples R China.

Reprint Address: Wang, Y (reprint author), Beihang Univ, Sch Biol Sci & Med Engn, Beijing 100191, Peoples R China.

E-mail Addresses: wangyu@buaa.edu.cn

IDS Number: AQ7NW

ISSN: 0959-2989

eISSN: 1878-3619

Source Item Page Count: 8



Impact Factor
1.091 1.28
2014 5 year

JCR® Category	Rank in Category	Quartile in Category
ENGINEERING, BIOMEDICAL	57 of 76	Q3
MATERIALS SCIENCE, BIOMATERIALS	27 of 33	Q4

Data from the 2014 edition of Journal Citation Reports®

Publisher
IOS PRESS, NIEUWE HEMWEG 6B, 1013 BG AMSTERDAM, NETHERLANDS
ISSN: 0959-2989
eISSN: 1878-3619

被引文献共计 0 篇(in SCIE), 其中他引文献 0 篇。

Record 5 of 6

Title: The Mutual Beneficial Effect between Medical Imaging and Nanomedicine

Author(s): Qiao, HT (Qiao, Huiting); Wang, LB (Wang, Libin); Han, JT (Han, Jintao); Chen, YM (Chen, Yingmao); Wang, DF (Wang, Daifa); Li, DY (Li, Deyu)

Source: JOURNAL OF NANOMATERIALS Article Number: 764095 DOI: 10.1155/2013/764095

Published: 2013

Times Cited in Web of Science Core Collection: 0

Total Times Cited: 0

Accession Number: WOS:000323964200001

Language: English

Document Type: Review

Addresses: [Qiao, Huiting; Wang, Libin; Wang, Daifa; Li, Deyu] Beihang Univ, Key Lab Biomech & Mechanobiol, Minist Educ, Sch Biol Sci & Med Engn, Beijing 100191, Peoples R China.

[Han, Jintao] Peking Univ, Dept Intervent Radiol & Vasc Surg, Hosp 3, Beijing 100871, Peoples R China.

[Chen, Yingmao] Gen Hosp PLA, Dept Nucl Med, Beijing 100853, Peoples R China.

Reprint Address: Li, DY (reprint author), Beihang Univ, Key Lab Biomech & Mechanobiol, Minist Educ, Sch Biol Sci & Med Engn, Beijing 100191, Peoples R China.

E-mail Addresses: deyuli@buaa.edu.cn

IDS Number: 212ED

ISSN: 1687-4110

eISSN: 1687-4129

Source Item Page Count: 7

一作第4



Impact Factor

1.644 1.798

2014 5 year

JCR® Category	Rank in Category	Quartile in Category
MATERIALS SCIENCE, MULTIDISCIPLINARY	122 of 260	Q2
NANOSCIENCE & NANOTECHNOLOGY	48 of 80	Q3

Data from the 2014 edition of Journal Citation Reports®

Publisher
HINDAWI PUBLISHING CORPORATION, 410 PARK AVENUE, 15TH FLOOR, #287
PMB, NEW YORK, NY 10022 USA

ISSN: 1687-4110
eISSN: 1687-4129

被引文献共计 0 篇(in SCIE), 其中他引文献 0 篇。

Record 6 of 6

Title: Modeling the excretion of FDG in human kidneys using dynamic PET

一作第5

Author(s): Qiao, HT (Qiao, Huiting); Bai, J (Bai, Jing); Chen, YM (Chen, Yingmao); Tian, JH (Tian, Jiahe)

Source: COMPUTERS IN BIOLOGY AND MEDICINE Volume: 38 Issue: 11-12 Pages: 1171-1176 DOI: 10.1016/j.combiomed.2008.09.006 Published: NOV-DEC 2008

Times Cited in Web of Science Core Collection: 2

Total Times Cited: 2

Accession Number: WOS:000261868500005

Language: English

Document Type: Article

Addresses: [Qiao, Huiting; Bai, Jing] Tsinghua Univ, Sch Med, Dept Biomed Engn, Beijing 100084, Peoples R China.

[Qiao, Huiting] Beijing Univ Aeronaut & Astronaut, Sch Biol Sci & Med Engn, Beijing 100083, Peoples R China.

[Chen, Yingmao; Tian, Jiahe] Gen Hos PLA, Dept Nucl Med, Beijing, Peoples R China.

Reprint Address: Bai, J (reprint author), Tsinghua Univ, Sch Med, Dept Biomed Engn, Beijing 100084, Peoples R China.

E-mail Addresses: deabj@tsinghua.edu.cn

IDS Number: 386FU

ISSN: 0010-4825



Impact Factor

1.24 1.459

2014 5 year

JCR® Category	Rank in Category	Quartile in Category
BIOLOGY	49 of 85	Q3
COMPUTER SCIENCE, INTERDISCIPLINARY APPLICATIONS	64 of 102	Q3
ENGINEERING, BIOMEDICAL	52 of 76	Q3
MATHEMATICAL & COMPUTATIONAL BIOLOGY	36 of 57	Q3

Data from the 2014 edition of Journal Citation Reports®

Publisher

PERGAMON-ELSEVIER SCIENCE LTD, THE BOULEVARD, LANGFORD LANE,
KIDLINGTON, OXFORD OX5 1GB, ENGLAND

ISSN: 0010-4825

被引文献共计 2 篇(in SCIE), 其中他引文献 1 篇。

Record 1 of 2

Title: Evaluation of F-18-FDG Excretion Patterns in Malignant Obstructive Uropathy

Author(s): Cho, A (Cho, Arthur); Chung, YE (Chung, Yong Eun); Lee, JH (Lee, Jae-hoon); Yun, M (Yun, Mijin); Lee, JD (Lee, Jong Doo); Kang, WJ (Kang, Won Jun)

Source: CLINICAL NUCLEAR MEDICINE Volume: 38 Issue: 9 Pages: 695-702 Published: SEP 2013

Accession Number: WOS:000330356900011

PubMed ID: 23816942

ISSN: 0363-9762

eISSN: 1536-0229

Record 2 of 2

Title: The Mutual Beneficial Effect between Medical Imaging and Nanomedicine

Author(s): Qiao, HT (Qiao, Huiting); Wang, LB (Wang, Libin); Han, JT (Han, Jintao); Chen, YM (Chen, Yingmao); Wang, DF (Wang, Daifa); Li, DY (Li, Deyu)

Source: JOURNAL OF NANOMATERIALS Article Number: 764095 DOI: 10.1155/2013/764095
Published: 2013

Accession Number: WOS:000323964200001

ISSN: 1687-4110

eISSN: 1687-4129

文献收录检索证明

作者姓名: 乔惠婷 (Qiao, Huiting)

经检索“网络版工程索引 (EI Compendex)”数据库, 该作者发表的
论文 (2008 年--2016 年), 被收录 5 篇。

检索结果见附件, 共 5 页。

检索时间为 2016 年 5 月 24 日。

特此证明!

证明人 (签字):



证明单位 (盖章): 北京航空航天大学图书馆

二〇一六年五月二十四日

附件:

1. An approach for detecting cerebral artery stenosis based on MRA images

EI 通讯第1

Accession number: 20131616215299

Authors: Li, X.W. (1); Zhu, G. (1); Yang, T. (1); Xia, X.G. (1); Fan, K. (1); Zhang, Q. (1); Qiao, H.T. (1); Li, S.Y. (1); Li, D.Y. (1)

Author affiliation: (1) School of Biological Science and Medical Engineering, Beihang University, No.37, Xueyuan, Road. Haidian district, Beijing, China

Corresponding author: Qiao, H.T.(qht@buaa.edu.cn)

Source title: IFMBE Proceedings

Abbreviated source title: IFMBE Proc.

Volume: 39 IFMBE

Monograph title: World Congress on Medical Physics and Biomedical Engineering

Issue date: 2013

Publication year: 2013

Pages: 2091-2094

Language: English

ISSN: 16800737

ISBN-13: 9783642293047

Document type: Conference article (CA)

Conference name: World Congress on Medical Physics and Biomedical Engineering

Conference date: May 26, 2012 - May 31, 2012

Conference location: Beijing, China

Conference code: 96476

Publisher: Springer Verlag, Tiergartenstrasse 17, Heidelberg, D-69121, Germany

Abstract: Cerebral artery stenosis is an important cause and risk factor to ischemic cerebrovascular disease. This paper describes a simple and effective method for the detection of cerebral artery stenosis in magnetic resonance angiography (MRA). Because..of the complex structure of the brain blood vessels, the fast and accurate segmentation method is needed. Here, we used the information of the maximum intensity projection (MIP) image to get 3D vascular structure. As skeleton was one of useful measures for charactering region-based shape features, we extracted 3D-Skeleton of blood vessels by using fast marching method. Finally, the accurate crosssectional areas based on cerebrovascular skeleton were computed to determine the location and extent of vascular stenosis. The results showed that our method could effectively detect the cerebral artery stenosis. © 2013 Springer-Verlag.

Number of references: 14

Main heading: Blood vessels

Controlled terms: Angiography - Biomedical engineering - Image segmentation - Magnetic resonance - Musculoskeletal system - Physics - Three dimensional - Three dimensional computer graphics

Uncontrolled terms: 3D segmentation - Cerebral arteries - Cross sectional profiles - MR angiography - Skeletonization

Classification code: 933 Solid State Physics

Solid State Physics

- 932 High Energy Physics; Nuclear Physics; Plasma Physics

High Energy Physics; Nuclear Physics; Plasma Physics

- 931 Classical Physics; Quantum Theory; Relativity

Classical Physics; Quantum Theory; Relativity

- 902.1 Engineering Graphics

Engineering Graphics

- 746 Imaging Techniques

Imaging Techniques

- 741.1 Light/Optics

Light/Optics

- 723.5 Computer Applications

Computer Applications

- 701.2 Magnetism: Basic Concepts and Phenomena

Magnetism: Basic Concepts and Phenomena

- 461 Bioengineering and Biology

Bioengineering and Biology

DOI: 10.1007/978-3-642-29305-4_549

201318

Database: Compendex

Compilation and indexing terms, Copyright 2016 Elsevier Inc.

Data Provider: Engineering Village

2. Dynamic simulation of FDG-PET image based on VHP datasets

EI 一作第1

Accession number: 20112814129357

Authors: Qiao, Huiting (1); Bai, Jing (2)

Author affiliation: (1) School of Biological Science and Medical Engineering, Beihang University, Beijing 100191, China; (2) Department of Biomedical Engineering, School of Medicine, Tsinghua University, Beijing 100084, China

Corresponding author: Qiao, H.(qht@buaa.edu.cn)

Source title: 2011 IEEE/ICME International Conference on Complex Medical Engineering, CME 2011

Abbreviated source title: IEEE/ICME Int. Conf. Complex Med. Eng., CME

Monograph title: 2011 IEEE/ICME International Conference on Complex Medical Engineering, CME 2011

Issue date: 2011

Publication year: 2011

Pages: 154-158

Article number: 5876723

Language: English

ISBN-13: 9781424493241

Document type: Conference article (CA)

Conference name: 2011 5th IEEE/ICME International Conference on Complex Medical Engineering, CME 2011

Conference date: May 22, 2011 - May 25, 2011

Conference location: Harbin, China

Conference code: 85402

Sponsor: IEEE Systems, Man, and Cybernetics Society; Institute of Complex Medical Engineering; Harbin Engineering University; Kagawa University

Publisher: IEEE Computer Society, 445 Hoes Lane - P.O.Box 1331, Piscataway, NJ 08855-1331, United States

Abstract: The FDG-PET is an important imaging tool for early diagnosis and treatment of malignant tumor and functional disease. The main purpose of this work is to propose a method for simulation of dynamic FDG-PET images based on VHP datasets. First the tissue time-activity curves (TTAC) are simulated using compartment model with blood time-activity curve (BTAC), and then the noises of each voxel are estimated according to the activity countering and the scan duration. At last according to the obtained BTAC and TTACs, a set of corresponding values are assigned to the segmented VHP image together with the independent Gaussian noise respectively. Series dynamic FDG-PET images were simulated respectively for normal physiology and pathology. The results of this work may provide a novel simulation platform for the research of PET image processing. © 2011 IEEE.

Number of references: 17

Main heading: Medical imaging

Controlled terms: Biomedical engineering - Computer simulation - Diagnosis - Diseases - Engineering research - Gaussian noise (electronic) - Image processing - Tissue

Uncontrolled terms: Compartment model - Data sets - Early diagnosis - FDG - FDG-PET - Image-based - Imaging tools - Malignant tumors - Scan duration - simulation image - Simulation platform - Time-activity curves - VHP

Classification code: 461 Bioengineering and Biology

Bioengineering and Biology

- 713 Electronic Circuits

Electronic Circuits

- 716 Telecommunication; Radar, Radio and Television

Telecommunication; Radar, Radio and Television

- 723.5 Computer Applications

Computer Applications

- 741 Light, Optics and Optical Devices

Light, Optics and Optical Devices

- 901.3 Engineering Research

Engineering Research

DOI: 10.1109/ICCME.2011.5876723

201130

Database: Compendex

Compilation and indexing terms, Copyright 2016 Elsevier Inc.

Data Provider: Engineering Village

EI 通讯第2

3. Air leak in noninvasive positive pressure ventilation: A platform and experimental studies

Accession number: 20144900293626

Authors: Zhang, Qi (1); Qiao, Huiting (1); Li, Xin (1); Pei, Baoqing (1); Wang, Daifa (1); Li, Deyu (1)

Author affiliation: (1) School of Biological Science and Medical Engineering, Beihang University, Beijing, China

Corresponding author: Qiao, Huiting

Source title: ISEEE 2014 - Proceedings: 2014 International Conference on Information Science, Electronics and Electrical Engineering
Abbreviated source title: ISEEE - Proc.: Int. Conf. Inf. Sci., Electron. Electr. Eng.
Volume: 2
Part number: 2 of 3
Issue date: November 5, 2014
Publication year: 2014
Pages: 1363-1367
Article number: 6947904
Language: English
ISBN-13: 9781479931965
Document type: Conference article (CA)
Conference name: 2014 International Conference on Information Science, Electronics and Electrical Engineering, ISEEE 2014
Conference date: April 26, 2014 - April 28, 2014
Conference location: Sapporo City, Hokkaido, Japan
Conference code: 109001
Sponsor: Future University Hakodate; IEEE Sapporo Section; Xiamen University
Publisher: Institute of Electrical and Electronics Engineers Inc.
Abstract: Noninvasive positive pressure ventilation (NPPV) has been widely used in the clinical and domestic therapy. Air leak is the unavoidable problem during NPPV. Undesirable leak may cause side effects on ventilation. In this paper, an experiment platform was established to study air leak in ventilation. The platform includes three parts: A ventilator control system, a lung model and a detection module. The platform was validated effective in NPPV leak study. Based on the experiment platform, the impacts of leak were studied. The air leak varied with the size of leak holes, airflow rate and airway pressure. It is found that in volume control ventilation the airflow rate about 25L/min will lead to less leakage than other airflow rates. It is significant for NPPV to establish an experiment platform and to discover the relationships between leakage and set-up parameters.
Number of references: 15
Main heading: Experiments
Controlled terms: Leak detection
Uncontrolled terms: Air flow-rate - Air leaks - Airway pressures - Detection modules - Experiment platforms - Lung model - Positive pressure ventilation - Side effect
Classification code: 901.3 Engineering Research
Engineering Research
- 943 Mechanical and Miscellaneous Measuring Instruments
Mechanical and Miscellaneous Measuring Instruments
DOI: 10.1109/InfoSEEE.2014.6947904
20150107
Database: Compindex
Compilation and indexing terms, Copyright 2016 Elsevier Inc.
Data Provider: Engineering Village

EI 一作第2

4. Improvement of medical imaging course by modeling of positron emission tomography

Accession number: 20140917403509
Authors: Qiao, Huiting (1); Wang, Libin (1); Liu, Wenyong (1); Wang, Yu (1); Li, Shuyu (1); Pu, Fang (1); Li, Deyu (1)
Author affiliation: (1) School of Biological Science and Medical Engineering, Beihang University, Beijing 100191, China
Corresponding author: Li, D.(deyuli@buaa.edu.cn)
Source title: Lecture Notes in Electrical Engineering
Abbreviated source title: Lect. Notes Electr. Eng.
Volume: 269 LNEE
Monograph title: Frontier and Future Development of Information Technology in Medicine and Education, ITME 2013
Issue date: 2014
Publication year: 2014
Pages: 2301-2305
Language: English
ISSN: 18761100
E-ISSN: 18761119
ISBN-13: 9789400776173
Document type: Conference article (CA)
Conference name: 5th International Symposium on IT in Medicine and Education, ITME 2013
Conference date: July 19, 2013 - July 21, 2013
Conference location: Xining, China

Conference code: 102717

Publisher: Springer Verlag, Tiergartenstrasse 17, Heidelberg, D-69121, Germany

Abstract: With the development of nuclear medical imaging, the medical imaging course has been developed in Beihang University. As an important part of nuclear medical imaging, Positron Emission Tomography (PET) is introduced in the imaging course with the methods of modeling and simulation. Pharmacokinetics model, Monte Carlo N-Particle Transport Code (MCNP) and Visible Human Project (VHP) datasets have been used to simulate the principle of PET imaging, which have made students understand the course more easily. The method that integrates imaging and modeling is potential and effective in the interdisciplinary teaching. © Springer Science+Business Media Dordrecht 2014.

Number of references: 10

Main heading: Medical imaging

Controlled terms: Computer simulation - Education - Education computing - Imaging techniques - Information technology - Models - Positron emission tomography

Uncontrolled terms: Model and simulation - Monte carlo n particles - Nuclear medical imaging - PET imaging - Positron emission tomography (PET) - Simulation - Transport codes - Visible human project

Classification code: 461.1 Biomedical Engineering

Biomedical Engineering

- 723.5 Computer Applications

Computer Applications

- 741 Light, Optics and Optical Devices

Light, Optics and Optical Devices

- 746 Imaging Techniques

Imaging Techniques

- 901.2 Education

Education

- 902.1 Engineering Graphics

Engineering Graphics

DOI: 10.1007/978-94-007-7618-0_282

201412

Database: Compendex

Compilation and indexing terms, Copyright 2016 Elsevier Inc.

Data Provider: Engineering Village

5. The study of PET image segmentation using clustering algorithm

EI 一作第3

Accession number: 20131616209805

Authors: Qiao, Huiting (1); Mei, Mengqi (1); Zhang, Qi (1); Liu, Nian (1); Li, Xin (1); Huang, Qiaoyang (1); Li, Deyu (1)

Author affiliation: (1) Key Laboratory for Biomechanics and Mechanobiology of Ministry of Education, School of Biological Science and Medical Engineering, Beihang University, Beijing, 37 Xueyuan road, Beijing, China

Corresponding author: Li, D.(deyuli@buaa.edu.cn)

Source title: IFMBE Proceedings

Abbreviated source title: IFMBE Proc.

Volume: 39 IFMBE

Monograph title: World Congress on Medical Physics and Biomedical Engineering

Issue date: 2013

Publication year: 2013

Pages: 1836-1839

Language: English

ISSN: 16800737

ISBN-13: 9783642293047

Document type: Conference article (CA)

Conference name: World Congress on Medical Physics and Biomedical Engineering

Conference date: May 26, 2012 - May 31, 2012

Conference location: Beijing, China

Conference code: 96476

Publisher: Springer Verlag, Tiergartenstrasse 17, Heidelberg, D-69121, Germany

Abstract: The segmentation of PET image is significant to clinical diagnosis. Clustering algorithm has the potential to segment the short dynamic PET images. Two kinds of clustering algorithms, K-means algorithm and the improved algorithm based on ISODATA, were validated and compared, with the simulated PET data and clinical dynamic PET images. Using the short dynamic data in the reasonable time range, the two clustering algorithms have the possibility to separate the region of interest. K-means algorithm depends on initial centers, while the improved algorithm based on ISODATA has little relation with initial centers, but depends on some other clustering parameters such as the relative standard deviation in cluster. The result of segmentation depends on not only the initial parameters but also the time range of dynamic scan. The optical scan protocol and the assignment of the

clustering parameters should be studied in further. © 2013 Springer-Verlag.

Number of references: 13

Main heading: Clustering algorithms

Controlled terms: Biomedical engineering - Diagnosis - Image segmentation - Physics

Uncontrolled terms: Clinical diagnosis - Dynamic data - Dynamic PET - Initial parameter - k-Means algorithm - Region of interest - Relative standard deviations - simulation

Classification code: 933 Solid State Physics

Solid State Physics

- 932 High Energy Physics; Nuclear Physics; Plasma Physics

High Energy Physics; Nuclear Physics; Plasma Physics

- 931 Classical Physics; Quantum Theory; Relativity

Classical Physics; Quantum Theory; Relativity

- 741.1 Light/Optics

Light/Optics

- 721 Computer Circuits and Logic Elements

Computer Circuits and Logic Elements

- 461.6 Medicine and Pharmacology

Medicine and Pharmacology

- 461.1 Biomedical Engineering

Biomedical Engineering

DOI: 10.1007/978-3-642-29305-4_483
201318

Database: Compendex

Compilation and indexing terms, Copyright 2016 Elsevier Inc.

Data Provider: Engineering Village

2016年专业技术职务评聘论文发表及收录情况证明表

单位：北京航空航天大学 生物与医学工程学院

姓名	乔惠婷	工作证号	08853	现任职称	讲师	任职时间	2008.09	
任现职以来发表论文及收录情况：收录类别、作者贡献（第一、通讯等）仅计算1次；论文收录以图书馆检索证明为准，未检索到的来源刊论文仅计算1篇								
类别	合计	SCI	SSCI	CSSCI	EI	ISTP	中文核 心期刊	其他
一、符合职称申报条件 论文	11	6			5			
其中：1. 第一作者	8	5			3			
2. 学生第一本人第二作者								
3. 通讯作者	3	1			2			
二、其他	9	5			1		2	1

本人承诺以上所填属实，如与事实不符，本人愿承担一切责任。

本人签字：



日期：2016年5月16日

单位负责人签字（加盖公章）：



日期：2016年5月16日

图书馆意见：

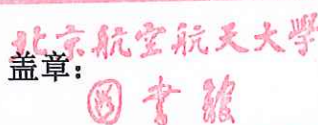
经检索，上表所列论文发表及收录情况属实。

经检索，上表中被 SCIE、EI 数据库收录的文章数量情况属实。

证明人：



盖章：



日期：2016年5月17日

检索专用章

注：1. 申请人认真如实填写相关信息后A4纸单面打印；

2. 对于学生第一本人第二作者的论文需填写《2016年专业技术职务评聘研究生指导情况证明表》由所在单位认定，主管副院长签字，学院盖章，研究生院审定，一并发去图书馆认定。

北京航空航天大学专业技术职务评审 任现职以来主要教学业绩水平证明表

姓 名 乔惠婷
 现任专业技术职务 讲师
 申请专业技术职务 副教授

单位 生物与医学工程学院
 任现职时间 2008.9
 填表日期 2016.5.17

一、教学总体情况

任现职以来,独立指导硕士研究生 5 届 6 人,其中毕业 4 人,在读 2 人;指导本科毕设 8 人,主讲本科生课 3 门,其中必修课 3 门;主讲研究生课 4 门、其中学位课 4 门。年均授课 80.125 学时。

二、本科教学工作量

	课程代码	课程名称	学年-学期	课程学时	本人授课学时	授课对象(本科生/留学生等)	授课次数(几轮次)	课程性质
教学工作量	E10B3320	生物医学信号处理	2008.9至今	48	24.7	本科生	6	必修
	F10C3240	生理系统建模与仿真	2009.3-2014.6	32	11	本科生	6	必修
	F10D3650	生物产业政策 and 法规	2013.1-2014.6	16	10	本科生	2	选修
	F10D3360	医疗器械规范与法规	2012.9-2013.12	16	2	本科生	2	必修
	G10C4430	专业综合实验	2011.9至今	10周	40	本科生	5	必修

注:课程性质为校级核心、专业基础核心、专业方向核心、必修、选修、公共选修等。

院(系)确认人签字: 乔惠婷
 教务处确认人签字: 周峰

教学成果材料奖	获奖时间	获奖项目名称		获奖等级	本人排名
教学研究	起止时间	教改立项项目名称(含编写教材、讲义)	项目来源	完成情况	本人作用
	2010.9-2011.9	“生物医学数字信号处理”课程体系改革与实践	校级	完成	负责人 <u>陈新</u>
其它	任务完成情况(含辅导员、军训、学生工作论文、指导青年教师及青年技术人员社会实践等)				本人作用
	第十一届青年教师课堂比赛暨青年教师教学基本功比赛一等奖				获奖者
	带队生产实习 3年				指导教师 <u>周峰</u>
	SRTP 2项(于思洋:用于漏气及RC补偿的呼吸机模型的建立,梅梦琪:基于动态多模成像提取代谢功能信息的方法研究)				指导教师 <u>周峰</u>
	指导本科毕设8人(王正文 36101125, 张葵 36101117, 崔吉慧 38101119, 于思洋 38101109, 李鑫 39102118, 刘念 10101033, 程子曼 11101026, 李一鸣 12101017)				指导教师 <u>周峰</u>
	2015.8-至今				代理班主任

院(系)确认人签字: 乔惠婷
 教务处确认人签字: 周峰

本人确认表内所填内容属实 签名: 乔惠婷

院(系)确认人签字(公章): 乔惠婷

教务处确认盖章: 周峰

日期: 2016.5.17

三、研究生教学工作量

教学工作量	课程名称	起止时间	课程学时	本人授课学时	授课对象 (研究生/ 留学生等)	授课次数 (几轮次)	课程类型
	生物医学信号处理	2009.9-2013.12	48	13.3	研究生	3	学位课
	生物系统建模和仿真	2012.3至今	48	11.5	研究生	4	学位课
	生理信号检测与处理实验	2013.3-2014.7	18	13.5	研究生	2	学位课
	生理系统建模与仿真实验	2012.3-2012.7	18	18	研究生	1	学位课
	医学图像处理及成像技术实验	2013.3-2013.7	18	18	研究生	1	学位课
	医疗器械创制与企业管理	2013.9至今	24	14	研究生	2	学位课
	生物医学成像技术	2013.3至今	32	2.7	研究生	3	学位课
	生物医学工程软件技术	2016.3至今	32	8	研究生	1	学位课
	生物医学传感器	2016.3至今	32	10	研究生	1	学位课

院(系)确认人签字:

研究生院确认人签字:

教 学 含 成 教 果 材 奖	获奖时间	获奖项目名称	获奖等级		本人排名
	2013	以交叉创新为导向的研究生多元化学术活动模式及其实践		校级二等	3
教 学 研 究	时间	项目名称	项目来源	完成情况	本人作用
	2011.10 -2012.10	生物医学工程学科跨专业研究生专业适应问题研究，	研究生教育与发展专项基金	完成	参与
	2011.10 -2012.10	生物医学工程交叉学科研究生课程教学方法研究，	研究生教育与发展专项基金	完成	参与
其 它	任务完成情况（含辅导员、学生工作论文、指导青年教师及青年技术人员社会实践等）				本人作用
	研究生张琪荣获北航工程硕士实习实践优秀成果。				指导教师
	指导硕士研究生 6 人（张琪 ZY1110121，王丽斌 SY1210120，古红玉 SY1310109，赵红俊 SY1410220，朱丹丹 GS1010111，刘聪 SY1510118）				指导教师

院(系)确认人签字:

研究生院确认人签字:

本人确认表内所填内容属实

院(系)确认人签字

研究生院确认人签字

签名:

(公章):

(公章):

日期:

证明

兹证明生物与医学工程学院乔惠婷老师（职工编号：08853），
于 2011 年获批北航“蓝天教学新星”称号。

特此证明。



荣誉证书

乔惠婷 同志

在 2012 年第十一届青年教师课堂教学比赛暨青年教师教学基本功比赛中获一等奖。特颁发此证，以资鼓励。

北京航空航天大学
二〇一二年十二月

荣誉证书

北京航空航天大学教学成果奖 获奖证书

获奖成果：以交叉创新为导向的研究生多元化学术活动模式及其实践

获奖者：韩慧瑜 樊瑜波 乔惠婷 刘岩 何静雯

获奖等级：二等奖

北京航空航天大学

2013年1月





硕士研究生国家奖学金 荣誉证书

编号: 2014 年第 00488 号

王丽斌 同学荣获 2014 年硕士研究生国家奖学金, 特颁此证。



中华人民共和国教育部

二〇一四年十二月三十一日

国家奖学金荣誉证书

荣誉证书

HONORARY CREDENTIAL

北京航空航天大学

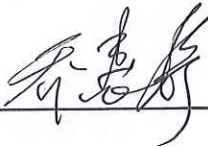



工程硕士实习实践优秀成果获得者

张 琪

北京航空航天大学

二〇一五年六月一日

2016年专业技术职务评聘专利与获奖情况认定表

单位	生物与医学工程学院	姓名	乔惠婷	工作证号	8853	任职时间	2008.9
1.获批专利情况							
任现职以来以第一享有人(含学生第一本人第二)名义共授权专利__项;任现职以来共获得已授权专利情况:							
类别	专利数	发明专利		实用新型		外观设计	
第一享有人	2	2		0		0	
总数量	2	2					
序号	专利名称	专利类型	授权日期	批准机构	专利号	仅限首次授权	
						权利单位	人数
1	一种无创通气接口检测系统	发明专利	2016/1/6	国家知识产权局	ZL201210438841.1	北京航空航天大学	5 1
2	一种基于压力波形估算容量控制通气漏气量的方法	发明专利	2016/4/27	国家知识产权局	ZL201410232734.2	北京航空航天大学	5 1
3							
4							
5							
6							
7							
8							
本人承诺以上所填属实。							
承诺人:				学院审核人(盖章):  赵崇青			
科研部门审核意见:							
经审核,上表所列奖项中,符合首次授权状态的归档专利共 2 项(序号: 1-2)。							
审核人:		 2016.5.25		盖章: 			

2.获奖情况

任现职以来获得国家级教学/科研成果奖__项；省部级教学/科研成果一等奖前五名、二等奖前三名或三等奖第一完成人共__项。请填写任现职以来获得教学、科研、管理奖励情况。

序号	奖励名称	颁奖部门	奖励级别	获奖时间	人数	本人排名
1	青年英才计划	北京市	省部级	2013	1	1
2	“蓝天新星”称号	北京航空航天大学	校级	2011	1	1
3	青年教师教学基本功比赛一等奖	北京航空航天大学	校级	2012	1	1
4	教学成果二等奖	北京航空航天大学	校级	2013	5	3
5	优秀党务工作者	北京航空航天大学	校级	2013	1	1
6						

本人承诺以上所填属实。

承诺人：



学院审核人（盖章）：



科研部门审核意见：

经审核，上表所列奖项中，情况属实的国家级科研成果奖__项（序号： ），省部级科研成果__项（序号： ）。

审核人：

盖章：

注：1.申请人认真如实填写相关信息后A4纸单面打印；

2.申请人签字确认后将此表及相关证明材料交至所在学院，由学院统一送至科研院审核；

3.申请人填写申报材料时以审核后的信息为准。

课题信息查询

经费负责人：乔惠婷

工作证号：08853

查询范围：2008-09-01到2016-05-25

总实到经费：161

单位：万元

编号	经费号	项目名称	项目来源	实到经费	设备费	外协费	课题性质	项目负责人
1	54-4885-01	基于流体伺服作动式外骨骼机器人的运动及生物力学模型研究	哈尔滨工程大学	40	0	0	技术开发	乔惠婷
2	52-7407-01	强机动目标追踪捕获的导航与控制算法设计及软件研制	上海航天控制技术研究所	19.1	0	0	技术开发	乔惠婷
3	30-4492-01	基于医学影像的脑血管构型及疾病风险分析	教育部	11.999945	0	0	非51合同	乔惠婷
4	30-3620-01	航空复杂环境下心血管-呼吸系统响应与防护的研究	教育部	15	0	0	非51合同	乔惠婷
5	30-2814	航空复杂环境下心血管-呼吸系统响应与防护的研究	教育部	10	0	0	非51合同	乔惠婷
6	37-5811	Calcineurin-NFAT信号通路在牵张力牵引神经突起生长中的功能和调控机制研究	国家基金委	26	0	0	非51合同	王梦航
7	30-2331	建立特种作业人员内照射剂量估计的虚拟刻度系统	教育部	2.499405	0	0	非51合同	乔惠婷
8	30-1880	基于物联网的手术室管理系统	工信部：重大项目领航基金	0.400615	0	0	非51合同	乔惠婷
9	37-5473	基于micro PET/CT对肺部肿瘤与炎症葡萄糖代谢动态特征的研究	国家自然科学基金	23	3	0	非51合同	乔惠婷
10	30-1312	基于 /对肺部肿瘤与炎症葡萄糖代谢动态特征的研究	工信部：“唯实”人才培育基金	2	0	0	非51合同	乔惠婷
11	30-0962	基于物联网的手术室管理系统	工信部：重大项目领航基金	6	0	0	非51合同	乔惠婷
12	30-0034	利用聚类分析从PET/CT短时动态成像中识别肿瘤组织的方法研究	工信部	5	0	0	非51合同	乔惠婷

科学技术研究院

查询日期：2016年05月24日

证明

兹证明生物与医学工程学院乔惠婷同志（职工编号：08853），
于 2013 年获批一项北京市青年英才项目，资助金额 15 万元。

特此证明。



证 明

兹证明乔惠婷于 2010、2012 年终考核被评为校优秀。

特此证明。

北京航空航天大学人事处

2016-05-27

人事处

证 明

兹证明乔惠婷于 2011、2013、2015 年终考核被评为院优秀。

特此证明。



证书

乔惠婷同志

被评为2011—2013年度校优秀党务工作者，
特此表彰。

中共北京航空航天大学委员会

二〇一三年七月



乔惠婷 同志

在北京航空航天大学60周年校庆中，积极奉献，特授予

积极奉献奖

北京航空航天大学
二〇一二年十二月

荣誉证书

乔惠婷同志

在 2010 年第三届青年教师教学业务培训提高班
学员代表交流环节，表现突出，获最佳 PPT 制作奖。

北京航空航天大学
二〇一〇年十二月



荣誉证书

乔惠婷 同志，

在 2010-2011 学年度努力工作、表现优秀，被评为学院优秀工作者，特发此证，以资鼓励。

北京航空航天大学

生物与医学工程学院

二〇一一年七月

留学回国人员证明

(2015) 组 教(文) 证字 3455 号

兹证明 乔惠婷 (男 ☐、女 ☒)，护照号码 E09709270) 系我国
在 美 国 德雷塞尔大学 学校 (单位)

的高级研究学者 ☐、访问学者 ☒、博士后 ☐、博士研究生 ☐、硕士研究生 ☐、
本科生 ☐、大专生 ☐、其他留学人员 ☐

在我驻外使 (领) 馆报到日期 2014 年 07 月 17 日

注册入学日期 2014 年 07 月 17 日

毕 (结) 业日期 2015 年 07 月 27 日

拟回国日期 2015 年 07 月 27 日

毕 (结) 业证书名称 _____ 号码 _____

备注 (留学经历描述) _____

留学回国人员签字:

经办人签字:

负责人签字:

教育 (文化) 处 (组) 公章

2015 年 06 月 12 日

第一联: 交留学回国人员

教育部国际合作与交流司 2012 年制表

注意事项

- 1、本证明只为学成回国工作的留学人员开具。
- 2、本证明由我驻外使 (领) 馆教育 (文化) 处 (组) 在留学人员回国时填写, 不得涂改。
- 3、本证明经使 (领) 馆教育 (文化) 处 (组) 经办人、负责人签字并在第一、第二联加盖公章方为有效。
- 4、第一联由留学人员保存, 其他单位可查验原件, 收存复印件, 不得收取原件。

教育部出国留学人员培训部
结业证书

学员乔惠婷，女，1980年12月20日出生，于2013年3月至2013年6月参加北京语言大学出国留学人员培训部英语高级班培训。经统一考试，成绩合格，准予结业。



证书编号: 1306297

CERTIFICATE
FOR GOVERNMENT-SPONSORED SCHOLARS GOING TO STUDY ABROAD

It is hereby certified that Ms. QIAO HUITING, born on Dec. 20, 1980, took the Advanced English Training Program at the Pre-departure Training Department, BLCU, affiliated with the Ministry of Education, from March 2013 to June 2013, and has passed the required tests with satisfactory scores.

Signature:

Dean of the Department for Pre-departure Training
Beijing Language and Culture University
Issued in June 2013

常州高新区人才工作领导小组办公室文件

常开人才办〔2012〕1号



关于聘请裘进浩等 110 名同志为常州高新区 “教授博士柔性进企业活动”专家的通知

各有关单位：

根据《关于开展 2012 年江苏省“教授博士柔性进企业活动”的通知》（苏人才办〔2012〕6 号）文件精神，经研究，决定聘请裘进浩等 110 名同志为常州高新区“教授博士柔性进企业活动”专家。名单如下：

北京航空航天大学：乔惠婷、蒲放、刘文勇、王豫

大连理工大学：林国强、吴爱民、王存山、郝胜智

徐军、秦福文、马春雨、张学宇

曲文超、尹基哲